Supplementary Information

Global cost drivers and regional trade-offs for low-carbon fuels: a prospective techno-economic assessment

Zipeng Liu*[1,2], Tom Terlouw[1,2], Patrick Frey[1,3], Christian Bauer*[1], Russell McKenna[1,2]

[1] Laboratory for Energy Systems Analysis, Centers for Nuclear Engineering and Sciences and Energy and Environmental Sciences, Paul Scherrer Institute, PSI, 5232, Villigen, Switzerland. E-mail: zipeng.liu@psi.ch, christian.bauer@psi.ch.

[2] Chair of Energy Systems Analysis, Institute of Energy and Process Engineering, ETH Zurich, Zurich 8092, Switzerland

[3] Department of Chemistry, University of Zürich

Contents

Supplementary Note 1: Technology specification

Hydrogen production pathways

Water Electrolysis: PEM, AE, SOEC

Water electrolysis utilizes electricity to separate water into H_2 and oxygen, as represented in equation (1)[1].

$$2H_2O \leftrightarrow 2H_2 + O_2 \tag{1}$$

Three major electrolysis technologies are considered viable for large-scale hydrogen production: **alkaline electrolysis (AE)**, **proton exchange membrane (PEM)** electrolysis, and **solid oxide electrolysis cells (SOEC)**. AE is the most mature technology, operating in an aqueous potassium hydroxide electrolyte at 70–90°C, offering low-cost, high durability, but lower current densities and slower dynamic response. PEM electrolysis utilizes a solid polymer electrolyte membrane, enabling higher current densities and flexible operation at 50–100°C, but requiring expensive catalysts and membrane materials. SOEC operates at 600–900°C, achieving higher efficiencies by utilizing both heat and electricity, but faces challenges in material degradation and commercialization. While AE and PEM are commercially available, SOEC remains in early development, with ongoing research focused on improving system durability and cost-effectiveness.

Nuclear based hydrogen: HTSE, CuCl

High-temperature steam electrolysis (HTSE) utilizes solid oxide electrolyzer cells (SOECs) in conjunction with nuclear power plants (NPPs) to enhance overall efficiency by integrating both thermal and electrical energy. In this process, steam supplied to the hydrogen electrode (cathode) serves to heat the electrochemical stack, where it dissociates into hydrogen and oxygen ions at operating temperatures of 750–950°C and pressures of up to 2 MPa. In this study, we consider an HTSE system coupled with a high-temperature gas-cooled reactor and a light-water reactor as the reference process[2,3] .

Beyond direct electrolysis, the **Cu-Cl thermochemical cycle (CuCl)** is among the most promising nuclear-integrated hydrogen production pathways[4,5]. In this study, we adopt the four-step Cu-Cl cycle[6] , which consists of hydrolysis, thermolysis, electrolysis, and drying/separation. Initially, cupric chloride ($CuCl_2$) reacts with superheated steam in a hydrolysis reactor, forming dicopper oxychloride (Cu_2OCl_2), hydrochloric acid (HCl), and unreacted steam. The Cu_2OCl_2 then undergoes thermal decomposition (thermolysis), producing oxygen gas and cuprous chloride (CuCl). The HCl-steam mixture is condensed and separated via pressure-swing distillation. CuCl is subsequently quenched and solidified, after which it, along with the recovered HCl, is directed to the anolyte make-up vessel (AMV) before entering the electrolyzer. During electrolysis, hydrogen is generated at the cathode, while $CuCl_2$, CuCl, HCl, and water are formed at the anode. These products are separated, with water and HCl passing through condensers and separation units. The remaining $CuCl_2$ is concentrated and dried, and CuCl is recycled back to the AMV, ensuring process continuity and efficiency.

Natural gas based hydrogen: SMR+CCS, ATR+CCS, CLR, M-PYR

Steam methane reforming with carbon capture and storgage (SMR+CCS) is the most widely used method for current fossil hydrogen production, leveraging a catalytic reaction between methane (CH_4) and steam (H_2O) at high temperatures (700–1000°C) in the presence of a nickel-based catalyst. The primary reaction follows: The overall reaction of both the processes is represented by equation (2).

$$CH_4 + 2H_2O \leftrightarrow CO_2 + 4H_2 \tag{2}$$

SMR is an endothermic process, requiring external heat input to sustain the reaction. It typically operates at pressures between 15–30 bar, and the generated synthesis gas (syngas) undergoes further purification through pressure swing adsorption (PSA) to separate pure hydrogen.

Autothermal reforming with carbon capture and storgage (ATR+CCS) integrates partial oxidation and steam reforming in a single-step process, achieving a thermally self-sustaining reaction without requiring external heat. Methane reacts with oxygen and steam at temperatures of 900–1100°C, facilitated by a nickel-based catalyst:

$$CH_4 + \frac{1}{2}O_2 \leftrightarrow CO + 2H_2 \tag{3}$$

$$CO + 2H_2O \leftrightarrow CO_2 + H_2 \tag{4}$$

ATR typically operates at pressures up to 30 bar and achieves higher hydrogen yields than SMR. The exothermic oxidation step provides the necessary heat for the endothermic steam reforming, eliminating the need for an external heat source and improving overall process efficiency. The product gas, primarily composed of H_2, CO, and CO_2, undergoes further purification through water-gas shift (WGS) and PSA units. ATR is particularly advantageous for large-scale hydrogen production and can be more compatible with carbon capture and storage (CCS) systems due to its concentrated CO_2 stream.

Chemical loop reforming (CLR) involves the controlled oxidation of methane with a sub-stoichiometric amount of oxygen at moderate temperatures (800–900°C) over a metal-based catalyst, typically nickel or rhodium[7], the reactions are the same with ATR.

Unlike SMR, which requires external heat, partial oxidation generates the necessary thermal energy internally, making the process faster and more compact. The synthesis gas (syngas) produced contains CO and H_2, which can be further processed in a water-gas shift reactor to enhance hydrogen yield.

CLR is particularly well-suited for decentralized and small-scale hydrogen production due to its rapid reaction kinetics and lower operating pressures compared to ATR. However, compared to ATR and SMR, the hydrogen yield per unit of methane is lower, and additional purification steps are required to remove residual CO_2 and CO from the final hydrogen stream. Compared with steam reforming technologies, the advantages of CLR are that the heat is provided by the oxidation with higher heat transfer coefficient, and no external combustion is needed[8] .

Methane pyrolysis (M_PYR), also known as methane cracking or methane decomposition, is a thermochemical process that decomposes methane into hydrogen and solid carbon directly at high temperatures catalytically in non-oxidative environments, as in equation (5)

$$CH_4 \leftrightarrow C + 2H_2 \tag{5}$$

This endothermic reaction requires high temperatures, typically ranging from 800°C to 1200°C, depending on the specific process conditions and reactor design. Various reactor configurations are employed, including plasma, thermal, and catalytic reactors, each offering distinct advantages in terms of efficiency and product quality[9] . A notable advantage of methane pyrolysis is its potential for low-emission hydrogen production. By generating solid carbon as a byproduct, the process inherently avoids the direct emission of CO_2.

Biomass based hydrogen: Biomass gasification with CCS

Biomass thermal gasification with carbon capture and storgage (TG-CCS) is a thermochemical process that converts biomass into a hydrogen-rich syngas through partial oxidation or steam reforming at high temperatures, typically 800–1000°C. The general reaction is represented as:

$$Biomass + H_2O \leftrightarrow H_2 + CO + CO_2 + CH_4 + Tar + Char \quad (6)$$

The produced syngas undergoes further water-gas shift (WGS) reactions to increase hydrogen yield, followed by gas cleaning and CO_2 separation. The integration of carbon capture and storage (CCS) enables the sequestration of CO_2 emissions, potentially resulting in negative carbon emissions when combined with sustainably sourced biomass. In this study, we consider a reference process design for hydrogen production via biomass gasification with CCS, as described in[10]. The process includes syngas cooling, gas cleanup, WGS, CO_2 capture, and hydrogen purification, with the captured CO_2 transported and stored in geological formations. Biomass gasification with CCS presents a promising pathway for low-carbon or negative-emission hydrogen production, depending on feedstock sustainability and capture efficiency[11].

Hydrocarbons production pathways

Hydrocarbon-based low-carbon fuels can be synthesized through various thermochemical and electrochemical pathways, utilizing renewable energy, captured CO_2, and biomass as feedstocks. This study considers solar-driven reforming, solar thermochemical conversion, Power-to-Liquid (PtL), and Biomass-to-Liquid (BTL) Fischer-Tropsch (FT) synthesis.

Fischer-Tropsch (FT) is a catalytic reaction involving the reaction between the reactants in syngas (CO and H_2) on the catalyst surface. It converts the syngas into a spectrum of liquid hydrocarbon products, such as liquid transportation fuels, alcohols, aldehydes, olefins, paraffins, etc. The main products of FTS are alkanes (Equation (7)), alkenes (Equation (8)), and alcohols (Equation (9)), but the product strongly depends on the catalyst's nature and reaction parameters.

$$nCO + (2n+1)H_2 \rightarrow C_nH_{2n+1} + nH_2O, n = 1,2,\ldots,\infty \quad (7)$$

$$nCO + 2nH_2 \rightarrow C_nH_{2n} + nH_2O, n = 2,3,\ldots,\infty \quad (8)$$

$$nCO + 2nH_2 \rightarrow C_nH_{2n+2}O + (n-1)H_2O, n = 1,2,\ldots,\infty \quad (9)$$

Solar FT fuel: SR-FT, ST-FT

Solar reforming FT (SR-FT) synthesis combines methane reforming with concentrated solar power (CSP) to produce syngas (H_2 + CO), which is further converted into synthetic fuels via FT synthesis. Solar reforming utilizes high-temperature solar heat (800–1200°C) in place of conventional fossil-based heating for steam reforming (CH_4 + H_2O) or dry reforming (CH_4 + CO_2), reducing CO_2 emissions while maintaining high hydrogen yields. The produced syngas is processed through FT synthesis, yielding various products such as synthetic aviation fuel (SAF), diesel, and gasoline[12].

This pathway reduces fossil fuel dependency while leveraging renewable thermal energy, making it an intermediate solution between fossil-based reforming and fully renewable FT synthesis. CCS is required to capture and store this CO_2, preventing emissions and ensuring low-carbon fuel production[13]. In this analysis, biomethane from anaerobic digestion is used for input methane source.

Solar thermochemical FT (ST-FT) synthesis offers a fully renewable pathway by directly converting CO_2 and H_2O into syngas using high-temperature solar-driven redox cycles. This process operates at 1000–1900 Kelvin. For the concentration of solar energy, either a field of heliostats focusing on a tower, or an array of dishes can be used. The resulting synthesis gas, a mixture of mainly H_2 and CO, is then converted into liquid fuels with the Fischer–Tropsch process. The resulting jet fuel is a drop-in fuel permitted for blends with conventional jet fuel with shares of up to 50%[12].Since ST-FT does not rely on fossil feedstocks, it inherently eliminates CO_2 emissions from hydrocarbon conversion.

Power to Liquid fuel: RWGS-FT, RWGS-MeOH

Reverse Water-Gas Shift (RWGS) +FT pathway utilizes electrolysis-derived hydrogen and captured CO_2 to synthesize hydrocarbon fuels. CO_2 reacts with H_2 via RWGS at 800–1100°C, producing syngas. The syngas undergoes FT synthesis, forming liquid hydrocarbons such as SAF and diesel. This process provides high flexibility in integrating renewable electricity and CO_2 capture, offering a scalable alternative to fossil-derived FT fuels[14].

RWGS-MeOH pathway can produce synthetic jet fuel through methanol synthesis followed by Methanol-to-Jet (MtJ) conversion[15]. CO_2-derived syngas is first converted into methanol (CH_3OH) via catalytic methanol synthesis. Methanol is then processed into kerosene (jet fuel) via dehydration and oligomerization reactions[14]. This pathway is optimized for aviation fuel applications, providing direct compatibility with existing infrastructure while being fully renewable when powered by green hydrogen and CO_2 capture.

BtL: BG-FT

Biomass thermal gasification FT (TG-FT) technology is considered as a good approach to obtaining environmentally friendly transportation fuel and reducing the high dependency on fossil fuels. BTL technology is a multistep process that involves the gasification of carbonaceous material (biomass) into synthesis gas, followed by conversion of the biomass-derived synthesis gas into synthetic fuel and chemicals.

With only a few BG-FT plants having been built to date at the pilot and demonstration scale, one significant challenge in scaling up the BTL-FT process is the economic aspect, which is a major motivation for developing novel processes that can use existing unit operations in a more effective process design. We considered the biomass gasification and FT process described in[16]. The input materials are woody biomass, and the target fuel is kerosene (SAF). Material and energy balance data are obtained from process modelling[16].

Biodiesel/Biokerosene production pathways

Hydrotreated vegetable oil and hydroprocessed esters and fatty acids (HVO/HEFA) is a mature and commercially deployed technology for producing advanced biofuels, including renewable diesel and sustainable aviation fuel (SAF/kerosene). The process involves catalytic hydrotreating of triglyceride-rich feedstocks (e.g., vegetable oils, animal fats, used cooking oil) with hydrogen (H_2), converting them into paraffinic hydrocarbons suitable for direct use as diesel or jet fuel. The generalized reaction is:

$$C_{57}H_{110}O_6 + H_2 \leftrightarrow 3\, C_{28}H_{38} + C_3H_8O_3 \tag{10}$$

Hydroprocessing removes oxygen and saturates the hydrocarbon chains, resulting in high-quality, drop-in fuels with properties similar to fossil diesel and jet fuel. HVO/HEFA fuels are fully compatible with existing diesel engines and aviation fuel infrastructure, with no blending limits. The process typically operates at 30–80 bar and 300–400°C, using catalysts such as Ni-Mo or Co-Mo. In our study, PEM hydrogen is used for hydroprossing.

Hydrothermal Liquefaction (HTL) is an emerging, less mature technology primarily considered for kerosene (jet fuel) production. In HTL, wet biomass (such as microalgae, sewage sludge, or lignocellulosic residues) is converted into bio-crude oil through reaction with water at subcritical conditions (typically 250–374°C and 100–350 bar). The bio-crude is then further upgraded via hydrotreatment to produce drop-in aviation fuels. Due to its current low technology readiness and limited commercial deployment, HTL is considered only for kerosene production in this analysis.

Biomass pyrolysis (B_PYR) is a thermochemical conversion process where lignocellulosic biomass is rapidly heated to 400–600°C in the absence of oxygen, yielding bio-oil (pyrolysis oil), syngas, and biochar. Fast pyrolysis maximizes bio-oil yield, while slow pyrolysis produces more biochar. The crude bio-oil requires further catalytic upgrading, such as hydrotreatment and hydrocracking, to reduce oxygen content and convert it into hydrocarbon fuels suitable for blending with jet fuel. In this study, only kerosene production from pyrolysis oil is considered due to the relatively high cost of upgrading for diesel. The upgrading process utilizes hydrogen is sourced from PEM electrolysis for hydrotreatment in this analysis.

Methane production: PTM, AD

The Power to Methane (PTM) production of methane from hydrogen and carbon dioxide is the reverse process of SMR. The catalytic methanation process was first described by Paul Sabatier in 1902 and has historically been employed to remove CO and CO_2 from hydrogen-rich gas streams, particularly in the fertilizer industry. More recently, research has expanded into biological methanation, wherein microorganisms metabolize hydrogen and CO_2 to produce methane. However, as biological methanation remains at the pilot and demonstration scale and is primarily suitable for small-scale applications, it is not considered in this study. Catalytic methanation occurs at temperatures of approximately 300–400 °C using a nickel-based catalyst. The reaction follows the general stoichiometry[17]:

$$CO_2 + 4H_2 \leftrightarrow CH_4 + 2H_2O \tag{11}$$

Anaerobic digestion (AD) is a biochemical process in which microorganisms break down organic biomass in an oxygen-free environment, producing biogas, primarily composed of methane (CH_4) and carbon dioxide (CO_2). This process occurs in four main stages: hydrolysis, acidogenesis, acetogenesis, and methanogenesis, where complex organic matter is progressively decomposed into simpler molecules, ultimately yielding CH_4-rich biogas. The general reaction for anaerobic digestion can be expressed as:

$$C_6H_{12}O_6 \leftrightarrow 3CH_4 + 3CO_2 \tag{12}$$

Raw biogas can be upgraded to biomethane by removing CO_2, H_2S, and water vapor, resulting in pipeline-quality renewable natural gas (RNG) or compressed/liquefied biomethane for transportation fuel use.

Ammonia production: HB

Industrial ammonia production is predominantly based on the Haber-Bosch (HB) process, in which nitrogen and hydrogen react catalytically over an iron-based catalyst to form ammonia[18]. This process is thermodynamically characterized by a decrease in entropy, favouring low temperatures and high pressures. However, due to the slow kinetics of the reaction, elevated temperatures of approximately 500 °C and pressures of 200 bar are required to achieve a viable reaction rate. the production of 1 kg of NH_3 requires approximately 0.18 kg of H_2 and 0.84 kg of N_2, resulting in a lower heating value (LHV) efficiency of 87%[18]. Additionally, the process demands around 0.5 $kWh_{el}/kgNH_3$, primarily for the compression of the input gas streams. The produced ammonia is subsequently liquefied at -33 °C, utilizing cooling from the evaporation of the nitrogen feed. In our analysis, only electrolyzed hydrogen is considered for ammonia production, and ammonia conversion is considered as a transport option for all the hydrogen.

$$N_2 + 3H_2 \rightarrow 2NH_3 \tag{13}$$

Carbon sources:

In this study, two representative carbon sources are considered for techno-economic assessment: Direct Air Capture (DAC) and biogenic CO_2. DAC is a process that removes CO_2 directly from ambient air (0.04 vol% concentration) using either solvent-based systems (e.g., alkaline solutions) or solid sorbent systems (e.g., amine-functionalized materials). In both approaches, CO_2 is bound to the capture medium and subsequently released as a concentrated stream through regeneration with heat or pressure. We adopt the standard DAC process and learning rate described in[19] as the benchmark option in our analysis.

The levelized cost of carbon (LCOC) for biogenic CO_2 captured from anaerobic digestion was estimated as a fraction of the DAC LCOC. Given the higher CO_2 concentration in biogas (typically 40–50 vol%) compared to ambient air, the capture cost for biogenic CO_2 is substantially lower. Based on recent techno-economic studies, we assumed a representative ratio of 25% of the DAC LCOC for biogenic CO_2 from anaerobic digestion, consistent with literature values[16,20].

Supplementary Note 2: Techno economic assessment

Country specific grid LCOE calculation

Grid integration cost thresholds

The integration cost penalty in grid LCOE calculations (see Equation 7, main text) is triggered when the combined share of solar PV and onshore wind exceeds a scenario- and country-specific threshold reflecting national grid flexibility and VRE integration capability.

- **Custom base thresholds** were set for selected countries (see Table S1) based on documented VRE integration experience, grid studies, and expert assessment. All other countries use a default threshold of 0.45.
- **Scenario multipliers:** Thresholds are scaled by 1.3 for 2030 and 1.6 for 2050, and by 1.1 (2°C) or 1.2 (1.5°C) climate scenarios. The maximum threshold is 0.80.
- **Integration penalty:** When the combined VRE share exceeds the threshold, an incremental penalty of 0.001–0.01 EUR/kWh is applied depending on the exceedance (see Table S2).

Grid Carbon Intensity Calculation

Grid carbon intensities are calculated as the weighted sum of the emission factors for each technology, using the grid mix in each country, scenario, and year. Technology emission factors are summarized in Table S3. Country-scenario-year carbon intensities were benchmarked against international “green hydrogen” thresholds (CertifHy, ≤4.4 kg CO_2-eq/kg H_2), corresponding to a grid electricity threshold of 0.038–0.050 kg CO_2-eq/kWh, depending on electrolyzer efficiency in different scenarios.

Table S1. Grid integration cost thresholds by country and scenario

Country (ISO)	Base Threshold (2024)	2030 Multiplier	2050 Multiplier	2°C Scenario Multiplier	1.5°C Scenario Multiplier	Max Applied Threshold	Notes
DNK (Denmark)	0.70	1.3	1.6	1.1	1.2	0.80	Custom: advanced VRE integration
DEU (Germany)	0.65	1.3	1.6	1.1	1.2	0.80	Custom: advanced VRE integration
NLD (Netherlands)	0.60	1.3	1.6	1.1	1.2	0.80	Custom: advanced VRE integration
GBR (United Kingdom)	0.60	1.3	1.6	1.1	1.2	0.80	Custom: offshore wind/high integration
FRA (France)	0.55	1.3	1.6	1.1	1.2	0.80	Custom: strong grid/nuclear base
AUS (Australia)	0.55	1.3	1.6	1.1	1.2	0.80	Custom: improving grid, high solar/wind
USA (United States)	0.55	1.3	1.6	1.1	1.2	0.80	Custom: large, diverse grid
CAN (Canada)	0.55	1.3	1.6	1.1	1.2	0.80	Custom: hydro base, strong grid
ESP (Spain)	0.50	1.3	1.6	1.1	1.2	0.80	Custom: strong VRE penetration
ITA (Italy)	0.50	1.3	1.6	1.1	1.2	0.80	Custom: moderate grid capability
CHN (China)	0.45	1.3	1.6	1.1	1.2	0.80	Custom: large system, grid challenges
BRA (Brazil)	0.45	1.3	1.6	1.1	1.2	0.80	Custom: hydro-dominated
IND (India)	0.40	1.3	1.6	1.1	1.2	0.80	Custom: grid challenges, rapid expansion
RUS (Russia)	0.40	1.3	1.6	1.1	1.2	0.80	Custom: aging grid
KOR (South Korea)	0.40	1.3	1.6	1.1	1.2	0.80	Custom: advanced, limited flexibility

JPN (Japan)	0.35	1.3	1.6	1.1	1.2	0.80	Custom: island grid, limited interconnection
IDN (Indonesia)	0.30	1.3	1.6	1.1	1.2	0.80	Custom: archipelago, fragmented grid
PHL (Philippines)	0.30	1.3	1.6	1.1	1.2	0.80	Custom: archipelago, grid challenges
MYS (Malaysia)	0.25	1.3	1.6	1.1	1.2	0.80	Custom: moderate infrastructure
SGP (Singapore)	0.20	1.3	1.6	1.1	1.2	0.80	Custom: small, limited flexibility
Default (all others)	0.45	1.3	1.6	1.1	1.2	0.80	Applied to all other countries

Custom grid integration thresholds are shown for major economies and key case studies; a default base threshold of 0.45 applies to all other countries. The final applied threshold is the base threshold times relevant multipliers, capped at 0.80.

Table S2. Integration cost penalty applied when VRE share exceeds the country- and scenario-specific threshold

Excess Share Above Threshold	Integration Cost Penalty (EUR/kWh)
≤ 0.15	0.001
≤ 0.30	0.003
≤ 0.45	0.006
> 0.45	0.010

Table S3. Emission factors by power generation technology as used in this study

Technology	Emission Factor (kg CO_2-eq/kWh)	Source
Coal (hard)	0.820	IPCC AR6[21], NREL[22]
Oil/Diesel	0.778	
Natural Gas (CCGT)	0.490	
Nuclear	0.012	
Hydro (large)	0.024	
Solar PV (utility)	0.041	
Wind (onshore)	0.011	
Biomass	0.230	
Geothermal	0.038	
Other renewables	0.050	

Dynamic WACC parameterization

Country-level adjustment: To account for regional financial risk, country-specific WACC components include[23]:

$$WACC_y = \frac{E}{V} K_{e,y} + \frac{D}{V} K_{d,y} = \frac{E}{V}\left(r_f + ERP + CRP_y + T_{p,0}\right) + \frac{D}{V}\left(r_f + CDS_y + L_{m,0}\right) \qquad (14)$$

where:

- r_f= 5%: Risk-free rate
- ERP = 5%: Mature-market equity risk premium[24,25]
- CRP_y and CDS_y are country-specific risk premium and credit default swap spread data sourced from Damodaran[23]

- The baseline technology premium $T_{p,0}$ = 3.25% and ender margin $L_{m,0}$ = 2%[24], respectively, represent typical values for early-commercial, yet not fully de-risked, energy technologies.
- Debt share is consistently set at D/V = 75%[24], reflecting typical mature energy industry financing structures to ensure comparability across scenarios.

The country adjustment factor is normalized as:

$$f_{wacc,y}(y) = \frac{WACC_y}{WACC_{base}}. \tag{15}$$

Technology-specific adjustment: Technology-specific risk is adjusted based on maturity (TRL) and global scale. The learning-related decline in financial risk is modeled as:

$$\alpha_x = \frac{T_{p,0} - 1\%}{TRL_{target} - TRL_{x,0}}, \qquad \beta_x = \frac{L_{m,0} - 0.5\%}{TRL_{target} - TRL_{x,0}} \tag{16}$$

where coefficients α_x and $\beta_x$represent a linear interpolation of risk premiums from current TRL ($TRL_{x,0}$) to mature TRL 9 (TRL_{target}). As technologies mature and their cumulative deployment increases, financial risk premiums decline according to the following[26,27]:

$$T_p(x,t) = \left[T_{p,0} - \alpha_x\left(TRL_{x,t} - TRL_{x,0}\right)\right] \cdot S_{x,t}^{-\lambda_e} \tag{17}$$

$$L_m(x,t) = \left[L_{m,0} - \beta_x\left(TRL_{x,t} - TRL_{x,0}\right)\right] \cdot S_{x,t}^{-\lambda_d} \tag{18}$$

$$\frac{D}{V}(x,t) = (D/V)_0 + \gamma\left(TRL_{x,t} - TRL_{x,0}\right) + \delta \ln\left(S_{x,t}\right) \tag{19}$$

where:

- γ = 0.05, and δ = 0.08: Debt share growth coefficients
- $\lambda_e = 0.25 \cdot LR_{x,t}$, and $\lambda_d = 0.125 \cdot LR_{x,t}$: Bankability learning effects
- $S_{x,t}$ is the global installed capacity index, $S_{x,t} = \frac{I_{x,t}}{I_{x,0}}$.

Updated costs of equity and debt are:

$$K_e(x,t) = r_f + ERP + CRP_0 + T_p(x,t) \tag{19}$$

$$K_d(x,t) = r_f + CDS_0 + L_m(x,t). \tag{20}$$

The updated WACC is then:

$$WACC^*(x,t) = \left[1 - \frac{D}{V}(x,t)\right] \cdot K_e(x,t) + \left[\frac{D}{V}(x,t)\right] \cdot K_d(x,t) \tag{21}$$

$$f_{wacc,x}(x,t) = \frac{WACC^*(x,t)}{WACC_{base}}. \tag{22}$$

Using Equations (12), (14), and (22), a fully dynamic WACC can be computed for each country, technology, and time step. This formulation captures the co-evolution of financial risk, technological maturity, and deployment scale, enabling robust and scenario-consistent cost assessments.

Monte Carlo analysis

Table S4. Monte carlo parameter distributions and ranges[28–30]

Parameter	Distribution	Baseline Value	Uncertainty Range / σ	Rationale / Reference
CAPEX	PERT	TEA input data	min: 0.7–0.8×, mode: 1.0×, max: 1.3–1.5×	Reflects skewed, bounded uncertainty; wider for 2050.
O&M	Lognormal	TEA input data	σ = 0.15 (2024), 0.18 (2030), 0.22 (2050)	Multiplicative uncertainty, literature precedent.
Plant Lifetime	Triangular	TEA input data	min: 0.7–0.8×, mode: 1.0×, max: 1.1–1.2×	Bounded, wider for 2050.
Efficiency	Trunc. Normal	TEA input data	σ = 6–10% of baseline, bounds: 50–110%	Avoids unphysical values.
Capacity Factor	Beta	8000/8760 (TEA input)	α, β chosen for mean, wider for 2050	Reflects operational variability.
Tech WACC factor	Triangular	TEA input data	±12% (2024), up to ±18% (2050)	Literature, expert judgment.
Country WACC fact.	Triangular	TEA input data	±18% (2024), up to ±27% (2050)	Literature, expert judgment.
Electricity price	Lognormal	LCOE (TEA input)	σ = 0.22 (2024), 0.28 (2030), 0.35 (2050)	Market volatility.
Biomass price	Normal	TEA input data	σ = 20% (2024), up to 30% (2050)	Market, supply chain uncertainty.
Water price	Normal	TEA input data	σ = 10% (2024), up to 15% (2050)	Low volatility.
Natural gas price	Lognormal	TEA input data	σ = 0.30 (2024), up to 0.45 (2050)	High market volatility.
CO_2 price (DAC)	Triangular	Model output	min: 0.5–0.7×, mode: 1.0×, max: 1.5–2.0×	Reflects technology learning.
H_2 price (PEM)	Lognormal	Model output	σ = 0.25 (2024), up to 0.4 (2050)	Market, technology learning.

Supplementary Note 3: Transport cost assessment

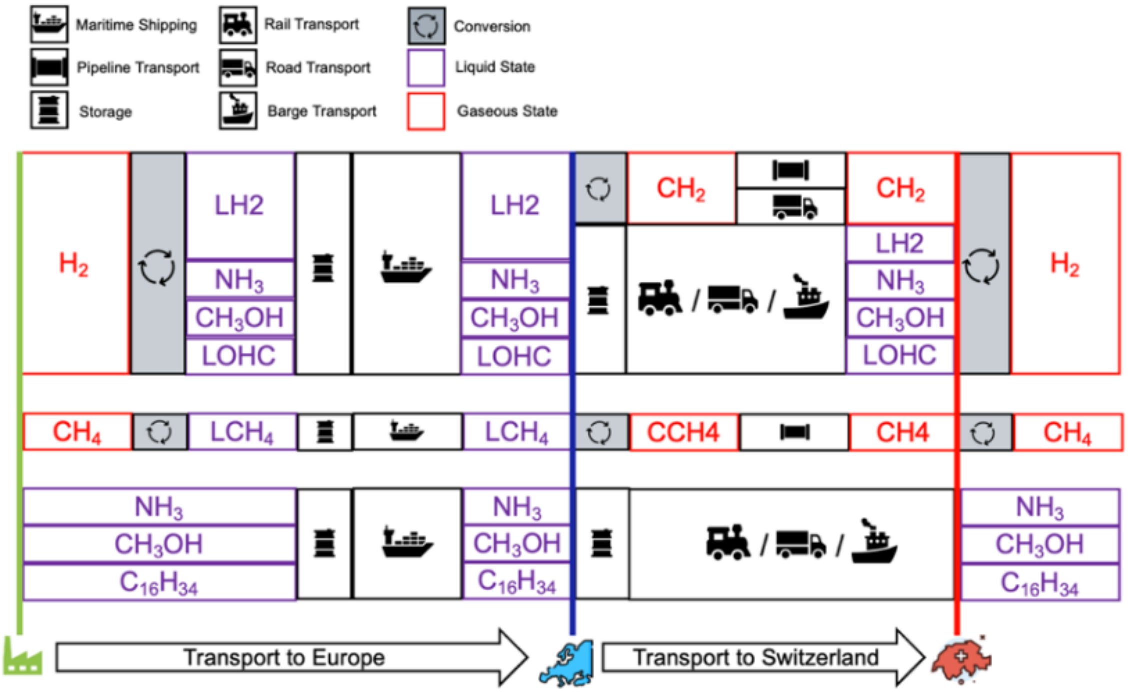

Fig S1. Hydrogen transport flowchart

Table S5. Overview of transport cost assumptions for selected fuels and transport modes[31–33]

	H_2 (as LH_2)	H_2 (as NH_3)	H_2 (as CH_3OH)	H_2 (as LOHC)	NH_3	CH_4	CH_3OH	$C_{16}H_{34}$
Conversion [EUR/t]	2024: 2500 2050: 1500	2024: 750 2050: 550	2024: 1200 2050: 650	2024: 350 2050: 200	n.a.	0.108	n.a.	n.a.
Ship Transport [EUR/t/km]	2024: 0.1 2050: 0.075	see NH_3	see CH_3OH	0.005	0.006	0.005	0.005	0.005
Truck Transport [EUR/t/km]	0.6	see NH_3	see CH_3OH	0.13	0.17	n.a.	0.13	0.13
Rail Transport [EUR/t/km]	2024: 0.5 2050: 0.3	see NH_3	see CH_3OH	0.016	0.021	n.a.	0.016	0.016
Barge Transport [EUR/t/km]	2024: 0.56 2050: 0.42	see NH_3	see CH_3OH	0.028	0.036	n.a.	0.028	0.028
New hydrogen Pipeline Transport [EUR/t/km]	0.2	see NH_3	see CH_3OH	n.a.	n.a.	0.033	n.a.	n.a.
Storage [EUR/t/d]	2024: 82 2050: 27	see NH_3	see CH_3OH	0.1	0.5	4.5	0.1	0.1
Reconversion [EUR/t]	180	2024: 1500 2050: 750	2024: 1300 2050: 750	2024: 2150 2050: 1000	n.a.	18	n.a.	n.a.

Supplementary input data

Table S6. Techno economic data used for the LCOX calculation. capex [EUR/kW]: capital expenditure. om [%]: operational expenditure (percentage of capex per year). lt [hours]: lifetime of production equipment. eff [%]: energy efficiency (LHV). Data references are the same as Table 1.

technology	sub	Base_2024	Base_2030	2 degree_2030	1.5 degree_2030	Base_2050	2 degree_2050	1.5 degree_2050
PEM	capex	1200	928	789	671	755	558	517
	om	5%	5%	5%	5%	5%	5%	5%
	lt	60000	71429	74286	78571	100000	110000	125000
	eff	58%	61%	62%	63%	70%	73%	75%
AE	capex	800	691	630	574	614	517	495
	om	3%	3%	3%	3%	3%	3%	3%
	lt	75000	82143	85000	89286	100000	110000	125000
	eff	67%	68%	69%	70%	70%	74%	78%
SOEC	capex	2500	2281	1853	1341	2118	1447	1014
	om	5%	5%	5%	5%	5%	5%	5%
	lt	20000	37143	38571	40000	80000	85000	90000
	eff	88%	88%	89%	89%	88%	90%	90%
HTSE	capex	2500	2307	1986	1390	1710	995	554
	om	5%	5%	5%	5%	5%	5%	5%
	lt	20000	37143	38571	40000	80000	85000	90000
	eff	88%	88%	89%	89%	88%	90%	90%
CuCl	capex	500	446	397	354	442	371	300
	om	5%	5%	5%	5%	5%	5%	5%
	lt	87600	87600	87600	87600	87600	87600	87600
	eff	43%	53%	53%	53%	63%	63%	63%
SMR+CCS	capex	1674	1592	1377	1173	1524	1204	930
	om	5%	5%	5%	5%	5%	5%	5%
	lt	219000	219000	219000	219000	219000	219000	219000
	eff	70%	70%	74%	74%	70%	85%	85%
ATR+CCS	capex	1307	1254	1087	911	1195	942	739
	om	5%	5%	5%	5%	5%	5%	5%
	lt	219000	219000	219000	219000	219000	219000	219000
	eff	70%	70%	71%	71%	70%	75%	75%
CLR	capex	1200	1159	975	778	1082	802	612
	om	5%	5%	5%	5%	5%	5%	5%
	lt	219000	219000	219000	219000	219000	219000	219000
	eff	75%	75%	75%	75%	75%	75%	75%
M_PYR	capex	1500	1384	1112	863	1099	674	418
	om	5%	5%	5%	5%	5%	5%	5%
	lt	219000	219000	219000	219000	219000	219000	219000
	eff	60%	60%	63%	66%	60%	70%	80%
TG+CCS	capex	800	747	553	402	682	460	283
	om	6%	6%	6%	6%	6%	6%	6%
	lt	262800	262800	262800	262800	262800	262800	262800
	eff	60%	60%	60%	60%	60%	60%	60%
SR-FT	capex	1030	887	650	465	704	410	219
	om	5%	5%	5%	5%	5%	5%	5%
	lt	219000	219000	219000	219000	219000	219000	219000
	eff	64%	64%	64%	64%	64%	64%	64%
ST-FT	capex	1800	1661	1334	1035	1319	842	452
	om	4%	4%	4%	4%	4%	4%	4%
	lt	219000	219000	219000	219000	219000	219000	219000
	eff	45%	45%	45%	45%	45%	45%	45%
TG-FT	capex	1787	1538	1128	807	1371	896	571
	om	5%	5%	5%	5%	5%	5%	5%
	lt	219000	219000	219000	219000	219000	219000	219000
	eff	50%	50%	50%	50%	50%	50%	50%
RWGS-FT	capex	1212	1043	805	566	930	619	408
	om	3%	3%	3%	3%	3%	3%	3%
	lt	219000	219000	219000	219000	219000	219000	219000
	eff	65%	65%	68%	68%	65%	74%	74%
RWGS-MeOH	capex	799	712	569	414	635	438	299
	om	3%	3%	3%	3%	3%	3%	3%
	lt	219000	219000	219000	219000	219000	219000	219000
	eff	78%	78%	78%	78%	78%	78%	78%
HTL	capex	2100	1896	1374	936	1791	1143	694
	om	5%	5%	5%	5%	5%	5%	5%

	lt	219000	219000	219000	219000	219000	219000	219000
	eff	45%	45%	45%	45%	50%	50%	50%
HVO	capex	2000	1906	1670	1410	1823	1510	1292
	om	5%	5%	5%	5%	5%	5%	5%
	lt	219000	219000	219000	219000	219000	219000	219000
	eff	80%	80%	80%	80%	80%	80%	80%
B_PYR	capex	1200	1112	946	776	1063	856	712
	om	5%	5%	5%	5%	5%	5%	5%
	lt	219000	219000	219000	219000	219000	219000	219000
	eff	40%	40%	40%	40%	45%	45%	45%
PTM	capex	320	309	268	211	299	206	152
	om	10%	10%	10%	10%	10%	10%	10%
	lt	219000	219000	219000	219000	219000	219000	219000
	eff	85%	85%	85%	85%	85%	85%	85%
AD	capex	1200	1159	1014	845	1063	891	747
	om	5%	5%	5%	5%	5%	5%	5%
	lt	219000	219000	219000	219000	219000	219000	219000
	eff	58%	58%	58%	58%	58%	58%	58%
HB	capex	515	512	509	505	510	505	499
	om	3%	3%	3%	3%	3%	3%	3%
	lt	219000	219000	219000	219000	219000	219000	219000
	eff	70%	70%	70%	70%	70%	70%	70%
DAC	capex	1384	1099	796	447	980	653	339
	om	12%	12%	12%	12%	12%	12%	12%
	lt	219000	219000	219000	219000	219000	219000	219000
	eff	50%	58%	58%	58%	78%	78%	78%

Table S7. Technology learning rate, TRL, and accumulated capacity data used for calculation and references.

Scenarios	**2 degree**							**1.5 degree**							**BAU**							**Refs**
Variables	Learning rate	TRL			Scale (Mt H_2 equivalent)			Learning rate	TRL			Scale (Mt H_2 equivalent)			Learning rate	TRL			Scale (Mt H_2 equivalent)			
Tech.		2024	2030	2050	2024	2030	2050		2024	2030	2050	2024	2030	2050		2024	2030	2050	2024	2030	2050	
PEM	14%	8	9	9	0.2	16	189	14%	8	9	9	0.2	51	327	14%	0.2	9	9	0.1	5	22	34–37
AE	8%	8	9	9	0.5	16	189	8%	8	9	9	0.5	51	327	8%	0.5	9	9	0.1	5	22	
SOEC	10%	7	8	9	0.1	16	189	15%	7	9	9	0.1	51	327	5%	0.1	8	9	0.1	5	22	
HTSE	10%	6	8	9	0.1	16	189	15%	6	9	9	0.1	51	327	5%	5	8	9	0.1	5	22	
CuCl	10%	5	7	9	0.1	1	1.5	15%	5	9	9	0.1	1	3	5%	6	8	9	0.1	1	1	
SMR+CCS	8%	8	9	9	1	8	56	13%	8	9	9	1	18	89	3%	8	9	9	1	2	8	7,32,34,38
ATR+CCS	8%	8	9	9	1	8	56	13%	8	9	9	1	18	89	3%	8	9	9	1	2	8	
CLR	10%	6	8	9	1	8	56	15%	6	9	9	1	18	89	5%	6	8	9	1	2	8	
PYR	10%	5	8	9	1	8	56	15%	5	9	9	1	18	89	5%	5	8	9	1	2	8	
TG+CCS	8%	8	9	9	0.1	0.5	1	13%	8	9	9	0.1	1	2	3%	8	9	9	0.1	0.1	1	10
SR_FT	10%	6	8	9	1	6	83	15%	6	9	9	1	16	142	5%	6	8	9	1	2	4	14,16,34,39–41
ST_FT	10%	5	7	9	1	6	83	15%	5	9	9	1	16	142	5%	5	7	9	1	2	4	
TG_FT	10%	7	8	9	0.1	0.1	1	15%	7	9	9	0.1	1	2	5%	6	8	9	0.1	0.1	2	
RWGS_FT	10%	7	8	9	1	6	83	15%	7	9	9	1	16	142	5%	6	8	9	1	2	4	
RWGS_MeOH	10%	7	8	9	1	6	83	15%	7	9	9	1	16	142	5%	6	8	9	1	2	4	
FAME	8%	8	9	9	0.23	1.4	3.83	13%	8	9	9	0.23	2.37	4.23	3%	8	9	9	0.23	0.6	1.47	42–44
HVO	10%	7	8	9	0.23	1.4	3.83	15%	7	9	9	0.23	2.37	4.23	5%	6	8	9	0.23	0.6	1.47	
PYR	10%	5	8	9	0.23	1.4	3.83	15%	5	9	9	0.23	2.37	4.23	5%	4	7	9	0.23	0.6	1.47	
PTM	10%	7	8	9	1	6	83	15%	7	9	9	1	16	142	5%	7	8	9	1	2	4	45,46
AD	10%	7	8	9	12.5	25	142.5	15%	7	9	9	12.5	67.5	245	5%	7	8	9	12.5	130	295	
HB	8%	9	9	9	1	6	83	13%	9	9	9	1	16	142	3%	9	9	9	1	2	4	18
DAC	8%	5	8	9	0.5	10	1000	13%	5	8	9	0.5	10	1000	5%	5	8	9	0.5	10	1000	19,47

Table S8. Input energy and material balance data for each technology's 1 kWh target fuel production. Data references are the same as Table 1.

tech	Target fuel	Pure water [kg/kWh]	Biomass [kg/kWh]	Industry water [kg/kWh]	CO_2 [kg/kWh]	CH_4 [kg/kWh]	H_2 [kg/kWh]	Elec [kWh/kWh]	Heat [kWh/kWh]
PEM	Hydrogen	0.405	0.000	0.000	0.000	0.000	0.000	1.000	0.000
AE	Hydrogen	0.405	0.000	0.000	0.000	0.000	0.000	1.000	0.000
SOEC	Hydrogen	0.405	0.000	0.012	0.000	0.000	0.000	0.800	0.200
HTSE	Hydrogen	0.405	0.000	0.000	0.000	0.000	0.000	0.800	0.200
CuCl	Hydrogen	0.405	0.000	0.000	0.000	0.000	0.000	0.290	0.710
SMR+CCS	Hydrogen	0.000	0.000	0.201	0.000	0.072	0.000	0.133	0.000
ATR+CCS	Hydrogen	0.000	0.000	0.201	0.000	0.090	0.000	0.107	0.000
CLR	Hydrogen	0.000	0.000	0.000	0.000	0.108	0.000	0.092	0.000
M_PYR	Hydrogen	0.000	0.000	0.000	0.000	0.106	0.000	0.168	0.000
TG+CCS	Hydrogen	0.000	0.392	0.000	0.000	0.000	0.000	0.000	0.000
SR_FT	Kerosene	0.108	0.000	0.000	0.000	0.0658	0.000	0.080	0.236
ST_FT	Kerosene	0.060	0.000	0.000	0.122	0.000	0.000	0.150	1.000
TG_FT	Kerosene	0.000	0.310	0.106	0.000	0.000	0.002	0.000	0.000
RWGS_FT	Kerosene	0.000	0.000	0.000	0.254	0.000	0.025	0.020	0.000
RWGS_MeOH	MeOH-Kerosene	0.000	0.000	0.000	0.251	0.000	0.030	0.025	0.000
FAME	Diesel	0.001	0.224	0.000	0.000	0.000	0.008	0.000	0.000
HVO	Diesel	0.000	0.097	0.000	0.000	0.000	0.002	0.000	0.000
B_PYR	Diesel	0.000	0.212	0.000	0.000	0.000	0.018	0.056	0.000
PTM	Methane	0.000	0.000	0.000	0.200	0.000	0.038	0.010	0.000
AD	Methane	0.000	0.480	0.000	0.000	0.000	0.000	0.06	0.100
HB	Ammonia	0.000	0.000	0.000	0.000	0.000	0.035	0.096	0.000

Table S9. Fuel property data used in the calculation[34].

Fuel	Boiling point (°C)	Energy density (kWh/L)	Lower heating value (LHV, kWh/kg)	Higher heating value (HHV, kWh/kg)	Lower heating value (LHV, MJ/kg)
Ammonia	-33.34	3.53	5.22	6.25	18.79
Methanol	64.70	4.67	5.60	6.40	20.16
Kerosene	150-300	10.70	11.90	12.70	42.84
Diesel	163-357	10.70	11.90	12.70	42.84
Methane	-161.60	0.01	12.70	14.75	45.72
Liquid hydrogen	−252.9	2.50	33.30	39.40	119.88

Table S10. WACC technology and scenario specific factor $\boldsymbol{f_{x,t}^{tech}(x,t)}$ data used in the calculation in each scenario and year.

tech	Base_2024	Base_2030	2 degree_2030	1.5 degree_2030	Base_2050	2 degree_2050	1.5 degree_2050
AD	1.4408	1.2366	1.0376	1.0264	1.019	1.0103	1.0093
AE	1.3737	1.0776	1.0525	1.0274	1.0456	0.999	0.9871
ATR+CCS	1.3533	1.071	1.0516	1.0424	1.0355	1.0128	1.0082
B_PYR	1.6682	1.4797	1.3173	1.0392	1.0495	1.0283	1.0265
CLR	1.5586	1.3787	1.1891	1.0257	1.0408	1	0.9918
CuCl	1.6758	1.4659	1.3263	1.0581	1.054	1.0428	1.034
DAC	1.7431	1.4659	1.2665	0.9677	1.0065	0.9514	0.9208
HB	0.9843	0.9795	0.9778	0.9751	0.9764	0.9756	0.9728
HTL	1.4516	1.1636	1.121	1.1009	1.1218	1.0714	1.0523
HTSE	1.6875	1.5154	1.3507	1.1484	1.0712	1.037	1.0205
HVO	1.5472	1.3261	1.119	1.1086	1.1177	1.098	1.0968
M_PYR	1.7431	1.5914	1.4317	1.1285	1.0736	1.0338	1.0228
PEM	1.3565	1.0633	1.0387	1.0142	1.032	0.9863	0.9746
PTM	1.5078	1.2972	1.0886	1.0696	1.0962	1.0332	1.0245

RWGS-FT	1.5696	1.2972	1.0886	1.0696	1.0614	1.0332	1.0245
RWGS-MeOH	1.5696	1.3138	1.1031	1.0838	1.0764	1.0481	1.0389
SMR+CCS	1.3294	1.0434	1.0278	1.0229	1.0113	0.9915	0.9847
SOEC	1.6289	1.4143	1.2278	1.0522	1.0691	1.0233	1.013
SR-FT	1.6875	1.5154	1.3507	1.1671	1.1215	1.0863	1.0634
ST-FT	1.7431	1.5914	1.4507	1.1588	1.1252	1.0938	1.0581
TG+CCS	1.4516	1.1371	1.0863	1.0717	1.071	1.0366	1.0143
TG-FT	1.6319	1.3525	1.126	1.112	1.1111	1.0778	1.065

Supplementary figures and results

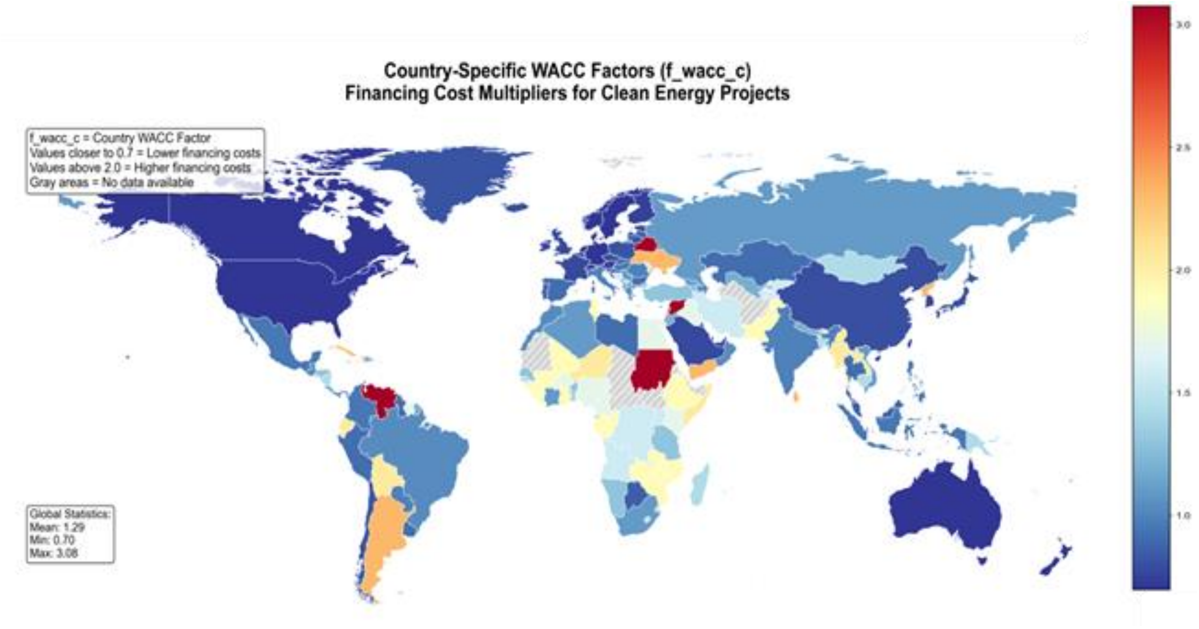

Fig. S2 global map of country specific WACC factor input (f_wacc_c)

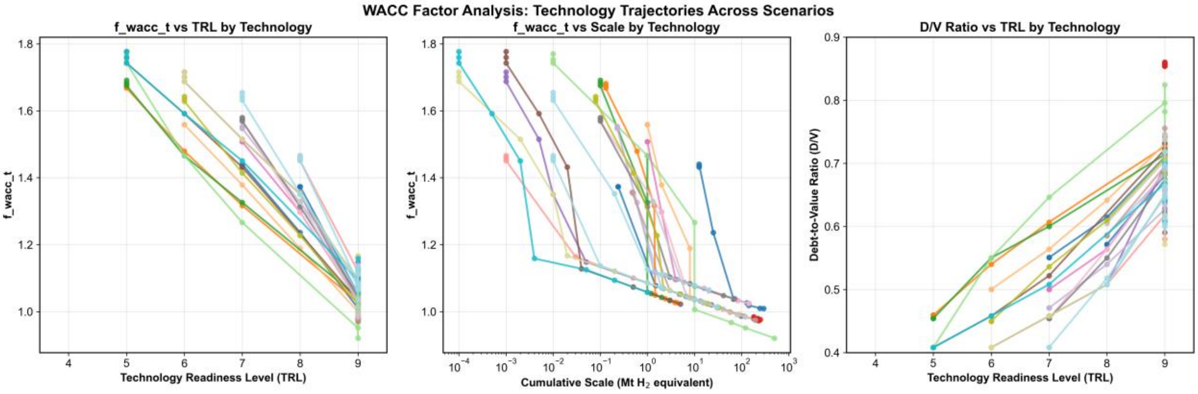

Fig. S3 Technology specific WACC factor input (f_wacc_t), at different TRL, cumulative scale, and the D/V ratio at differet TRL.

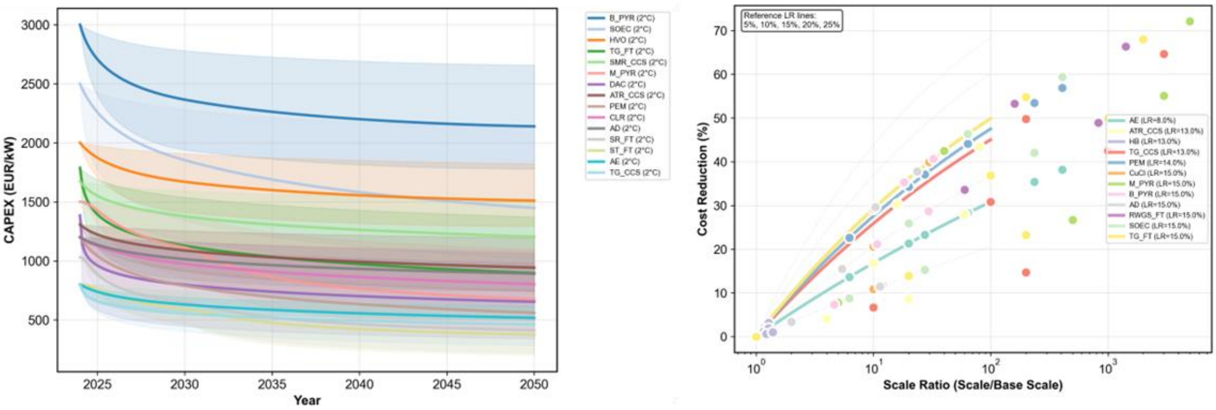

Fig. S4 CAPEX learning curve input and the cost redudctuions versus scale ratio

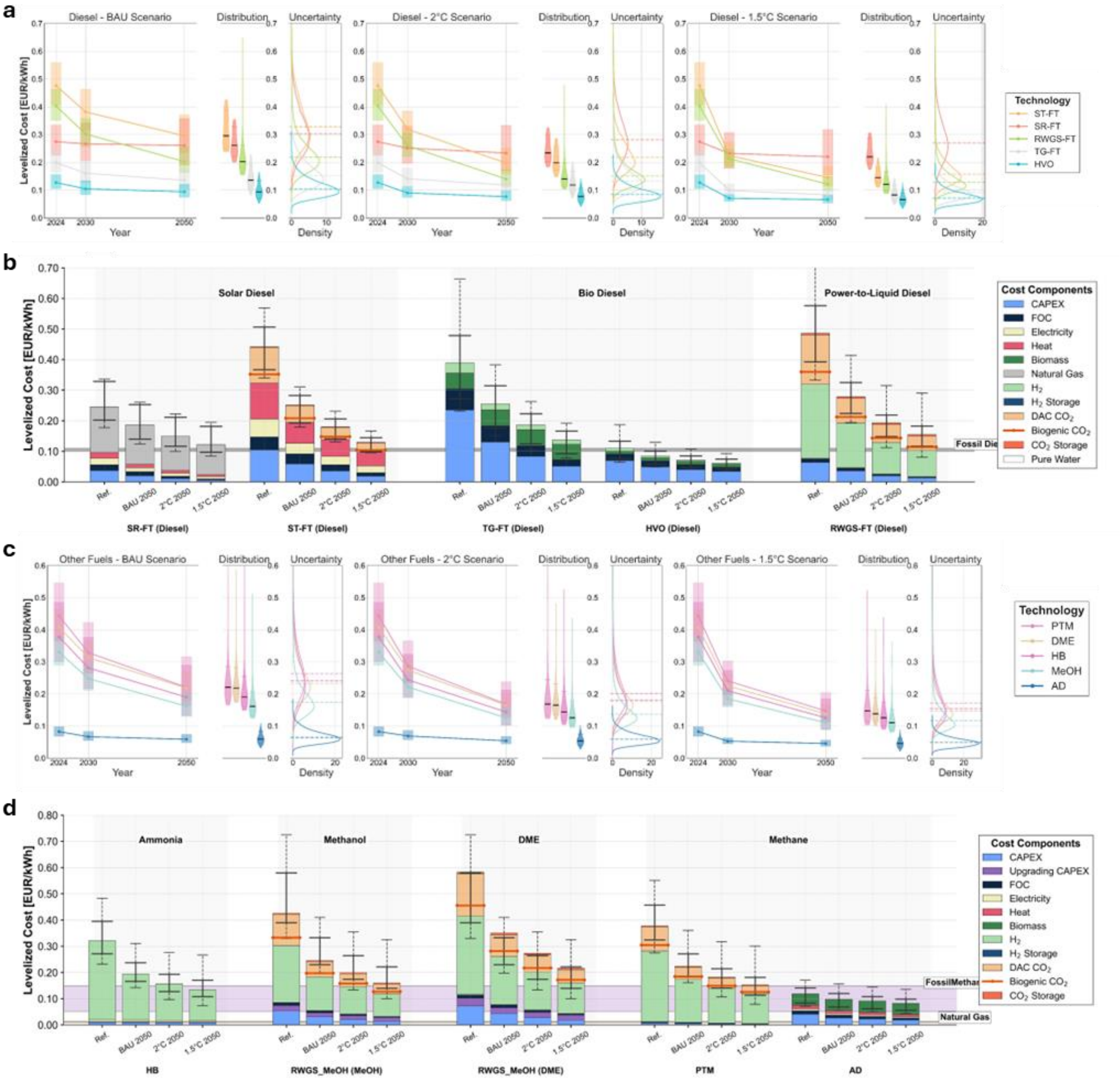

Fig. S5 Global cost trajectories and cost component breakdowns for diesel and other fuel production technologies across climate scenarios. (a, c) Time series of median levelized costs for diesel and other fuel pathways from 2024 to 2050 under BAU, 2 °C, and 1.5 °C scenarios. Left panels show cost trajectories with uncertainty bands representing Monte Carlo parameter uncertainty (10th–90th percentile). Middle panels display 2050 cross-country cost distributions as violin plots, with median and percentile markers. Right panels show Monte Carlo parameter uncertainty distributions for 2050 with density curves and median indicators. (b, d) Stacked-bar breakdowns of cost components for diesel and other fuel pathways in 2024 and 2050 scenarios. Diesel pathways include solar diesel (ST-FT, SN-FT), bio diesel (TG-FT, HVO), and power-to-liquid diesel (RWGS-FT). Other fuels include ammonia (HB), methanol (RWGS_MeOH), dimethyl ether (RWGS_MeOH_DME), and synthetic methane (PTM, AD). Bars show the sum of country-wise median component costs. Error bars represent cross-country variation (10th–90th percentile) in total costs. Cost components include CAPEX, O&M, electricity, heat, biomass, fossil inputs, H_2 feedstock & storage, CO_2 feedstock & storage, and other inputs. Shaded reference bands indicate fossil diesel (0.10–0.12 EUR/kWh), fossil methanol (0.05–0.155 EUR/kWh), and natural gas (0.015–0.025 EUR/kWh) costs for comparison[39,43,48].

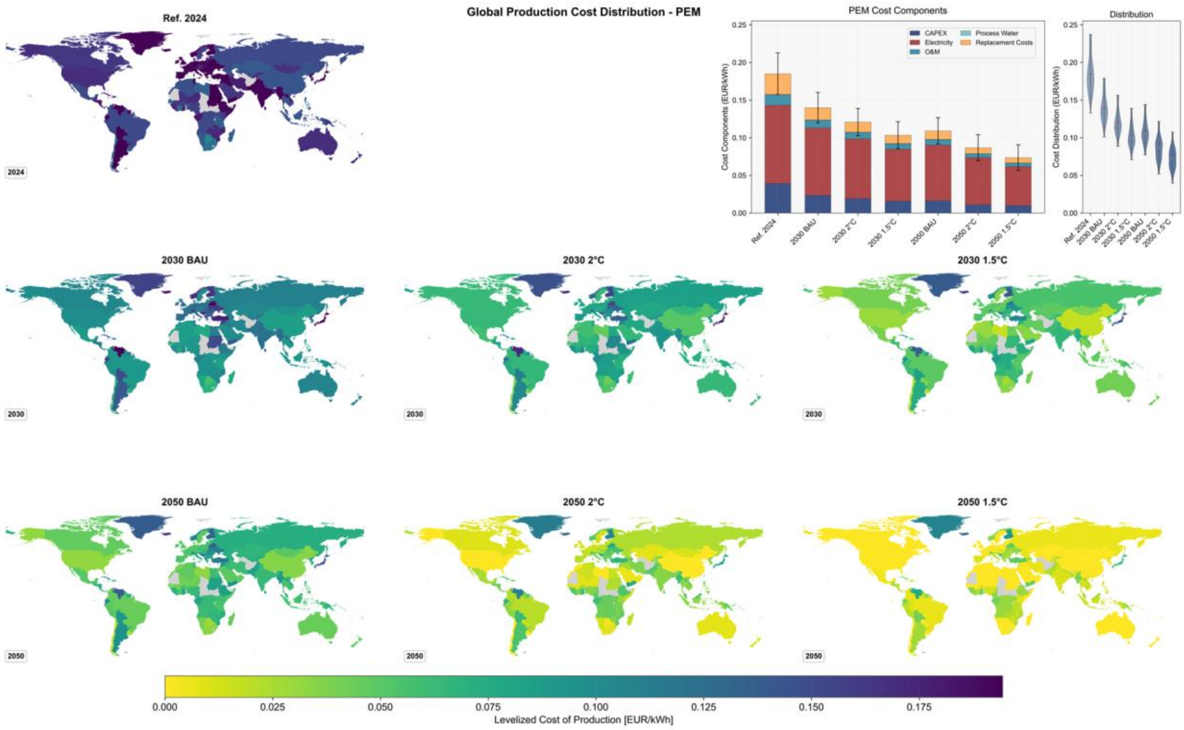

Fig. S6 Global production cost distribution for proton exchange membrane (PEM) under grid-connected conditions. The seven world maps show the levelized cost of hydrogen (LCOH) in EUR/kWh for the reference year 2024 and for three scenarios (BAU, 2 °C, and 1.5 °C) in 2030 and 2050. The color scale ranges from lower costs (green/yellow) to higher costs (purple). The bar chart on the top right shows the breakdown of LCOH into major cost components (e.g., electricity, capital expenditure) for each scenario-year combination, with error bars indicating standard deviations across countries. The violin plot to the right illustrates the global distribution of LCOH values, showing spread within ±2 SDs.

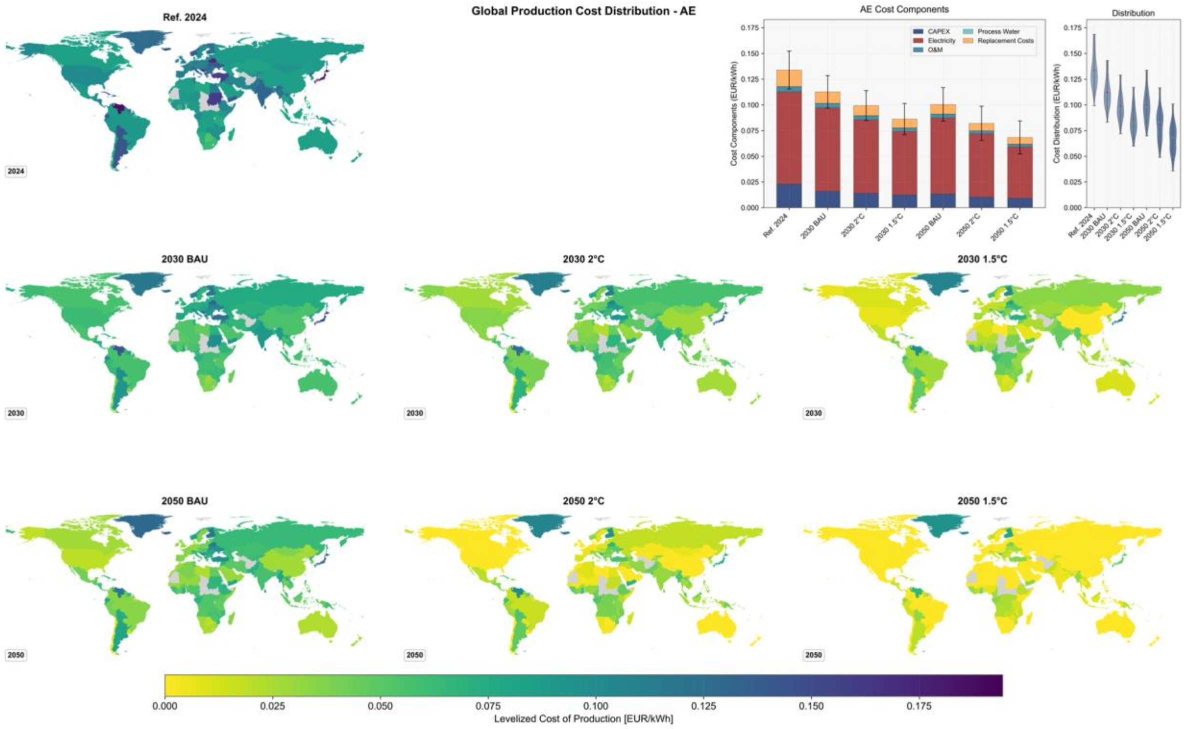

Fig. S7 Global production cost distribution for alkaline electrolysis (AE) under grid-connected conditions. The seven world maps show the levelized cost of hydrogen (LCOH) in EUR/kWh for the reference year 2024 and for three scenarios (BAU, 2 °C, and 1.5 °C) in 2030 and 2050. The color scale ranges from lower costs (green/yellow) to higher costs (purple). The bar chart on the top right shows the breakdown of LCOH into major cost components (e.g., electricity, capital expenditure) for each scenario-year combination, with error bars indicating standard deviations (SDs) across countries. The violin plot to the right illustrates the global distribution of LCOH values, showing spread within ±2 SDs.

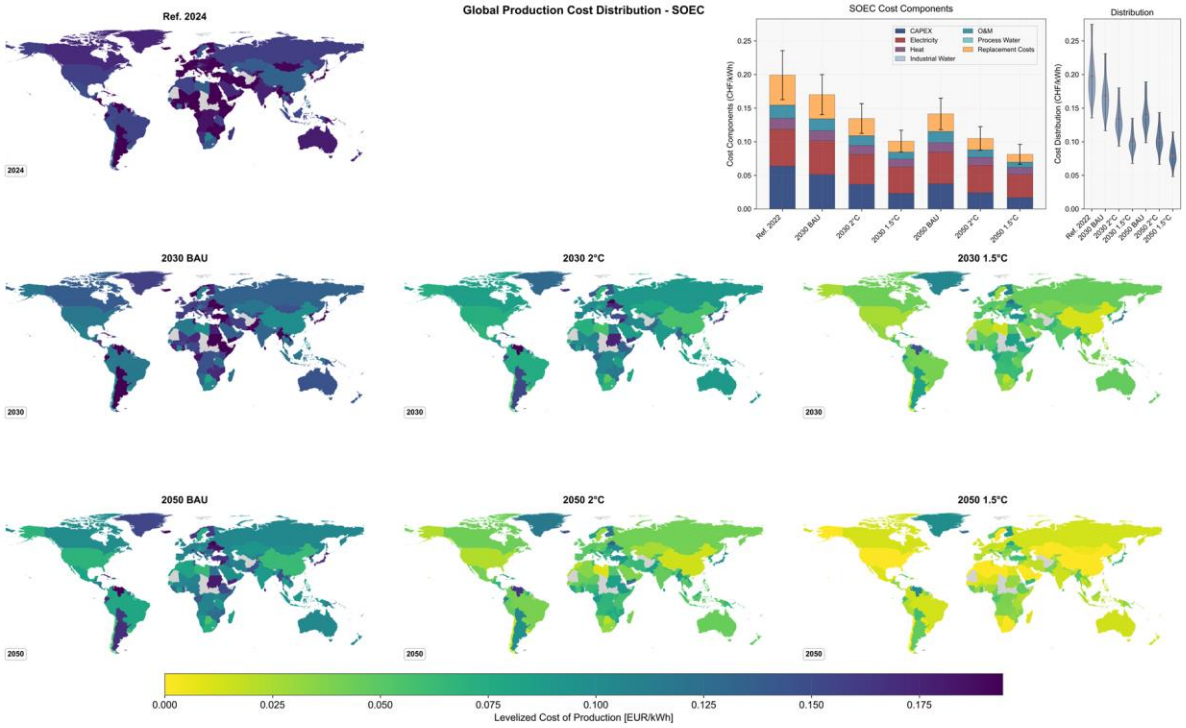

Fig. S8 Global production cost distribution for solid oxide electrolysis cells (SOEC) under grid-connected conditions. The seven world maps show the levelized cost of hydrogen (LCOH) in EUR/kWh for the reference year 2024 and for three scenarios (BAU, 2 °C, and 1.5 °C) in 2030 and 2050. The color scale ranges from lower costs (green/yellow) to higher costs (purple). The bar chart on the top right shows the breakdown of LCOH into major cost components (e.g., electricity, capital expenditure) for each scenario-year combination, with error bars indicating standard deviations across countries. The violin plot to the right illustrates the global distribution of LCOH values, showing spread within ±2 SDs.

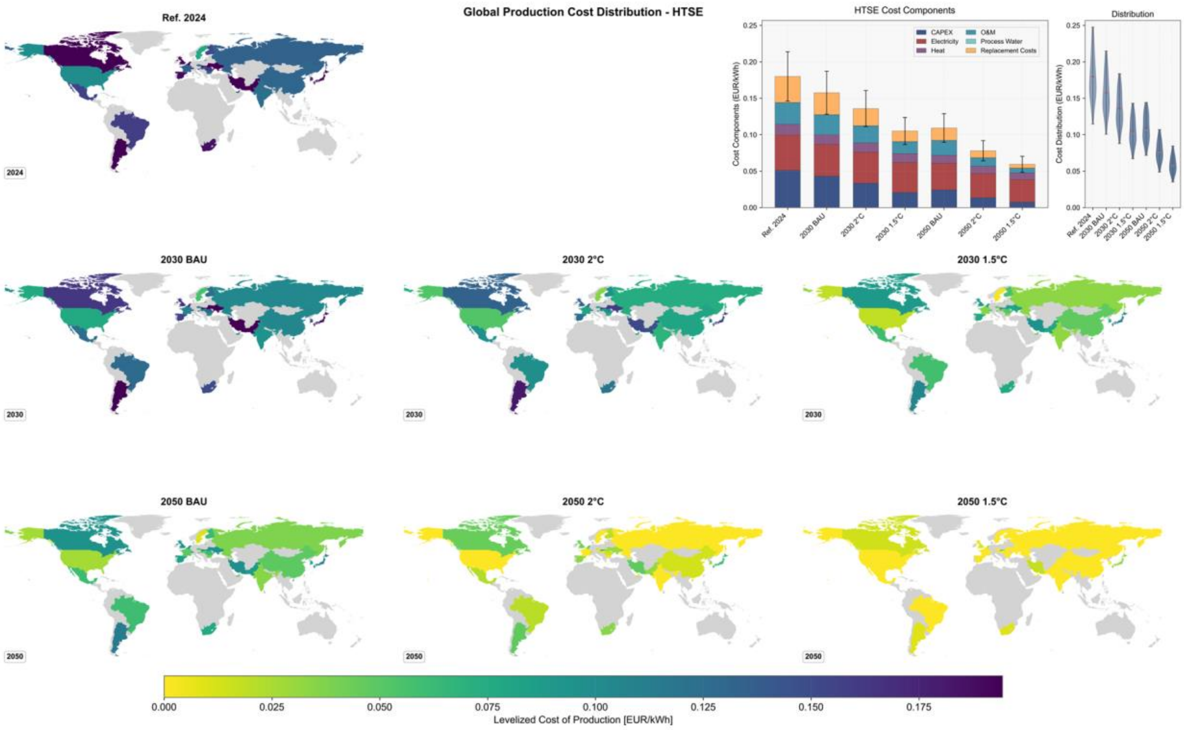

Fig. S9 Global production cost distribution for high-temperature steam electrolysis (HTSE) under nuclear-based hydrogen production. The seven world maps depict the levelized cost of hydrogen (LCOH) in the reference year 2024 and under three scenarios (BAU, 2 °C, 1.5 °C) for 2030 and 2050, using a color scale from lower costs (green/yellow) to higher costs (purple). The bar chart on the top right shows the breakdown of cost components in each scenario-year combination, with error bars indicating standard deviations across different countries. The violin plot to the right illustrates the global distribution of these LCOH values, showing spread within ±2 SDs.

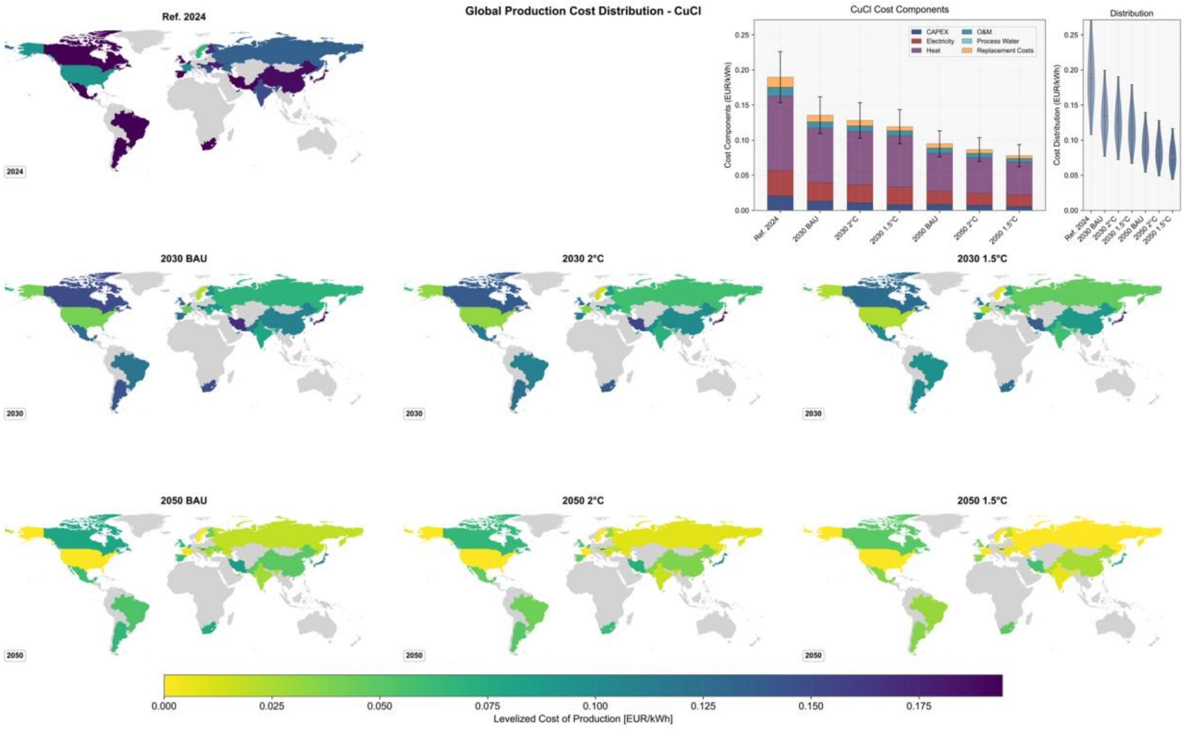

Fig. S10 Global production cost distribution for the CuCl thermochemical cycle (CuCl) under nuclear-based hydrogen production. The seven world maps depict the levelized cost of hydrogen (LCOH) in the reference year 2024 and under three scenarios (BAU, 2 °C, 1.5 °C) for 2030 and 2050, using a color scale from lower costs (green/yellow) to higher costs (purple). The bar chart on the top right shows the breakdown of cost components for AE in each scenario-year combination, with error bars indicating standard deviations across different countries. The violin plot to the right illustrates the global distribution of these LCOH values, showing spread within ±2 SDs.

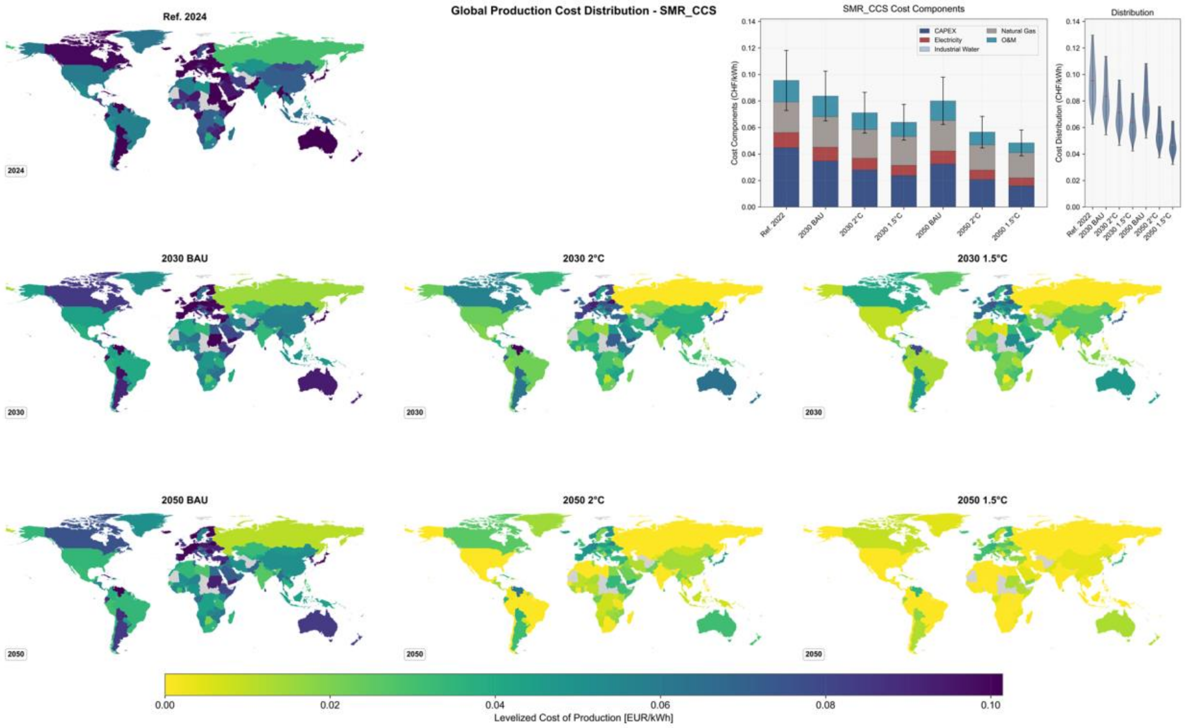

Fig. S11 Global production cost distribution for steam methane reforming with CCS (SMR+CCS) under various scenarios. Maps for 2024 and three scenarios (BAU, 2 °C, 1.5 °C) in 2030 and 2050 use a color scale from lower (green/yellow) to higher (purple) costs. The bar chart highlights capital, operating, and feedstock costs, with error bars showing standard deviations across countries. The violin plot on the right displays the global distribution of costs, showing spread within ±2 SDs.

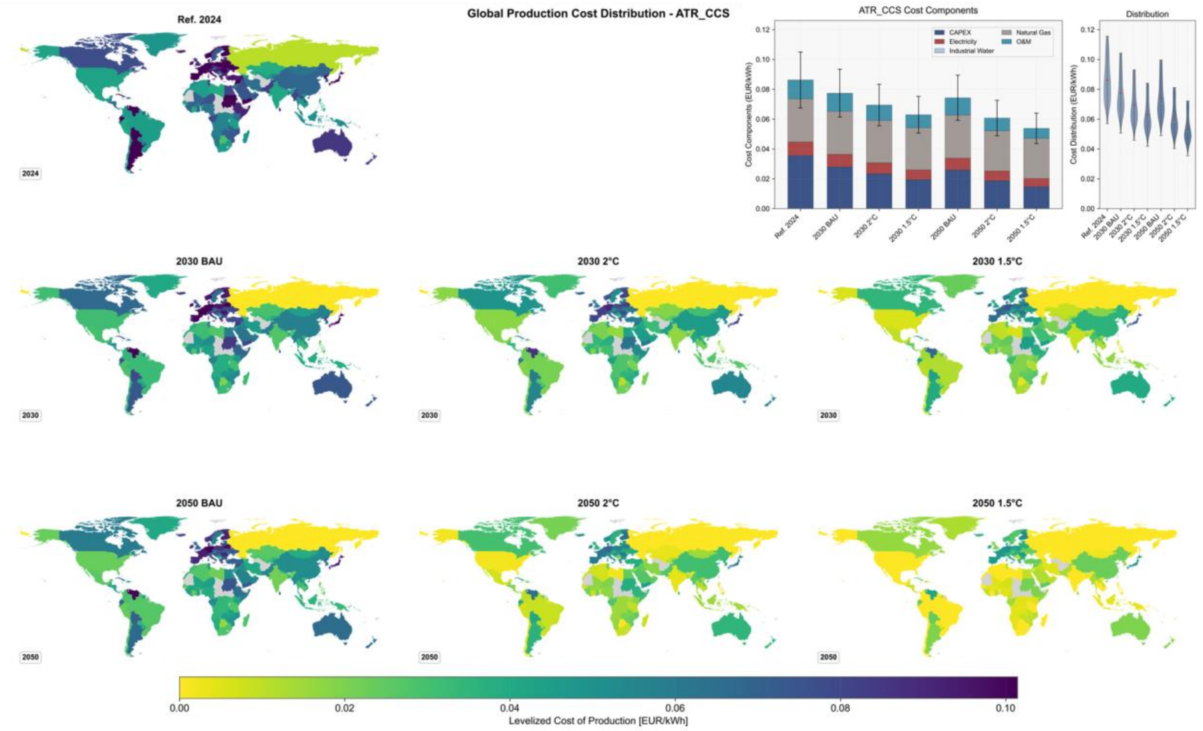

Fig. S12 Global production cost distribution for autothermal reforming with CCS (ATR+CCS) under various scenarios. The top-left map corresponds to 2024, followed by BAU, 2 °C, and 1.5 °C scenarios in 2030 and 2050. Colors shift from green (lower LCOH) to purple (higher LCOH). The bar chart reveals the relative contributions of major cost elements, while the error bars reflect cross-country variability. The violin plot shows the range and median trends of costs, showing spread within ±2 SDs.

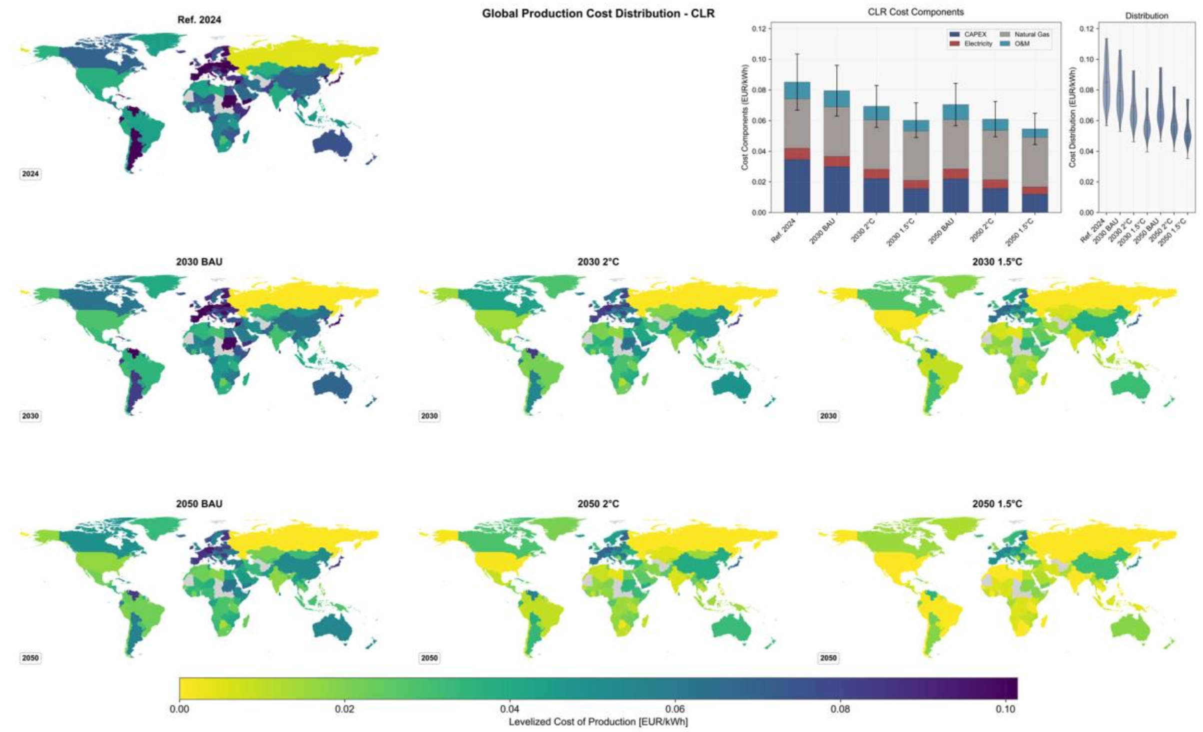

Fig. S13 Global production cost distribution for chemical looping reforming (CLR) under various scenarios. Each map displays the LCOH for 2024, BAU, 2 °C, and 1.5 °C scenarios in 2030 and 2050, transitioning from lower costs (green/yellow) to higher costs (purple). The bar chart details major cost components, with error bars illustrating cross-country variation. The violin plot highlights the distribution of costs, showing spread within ±2 SDs.

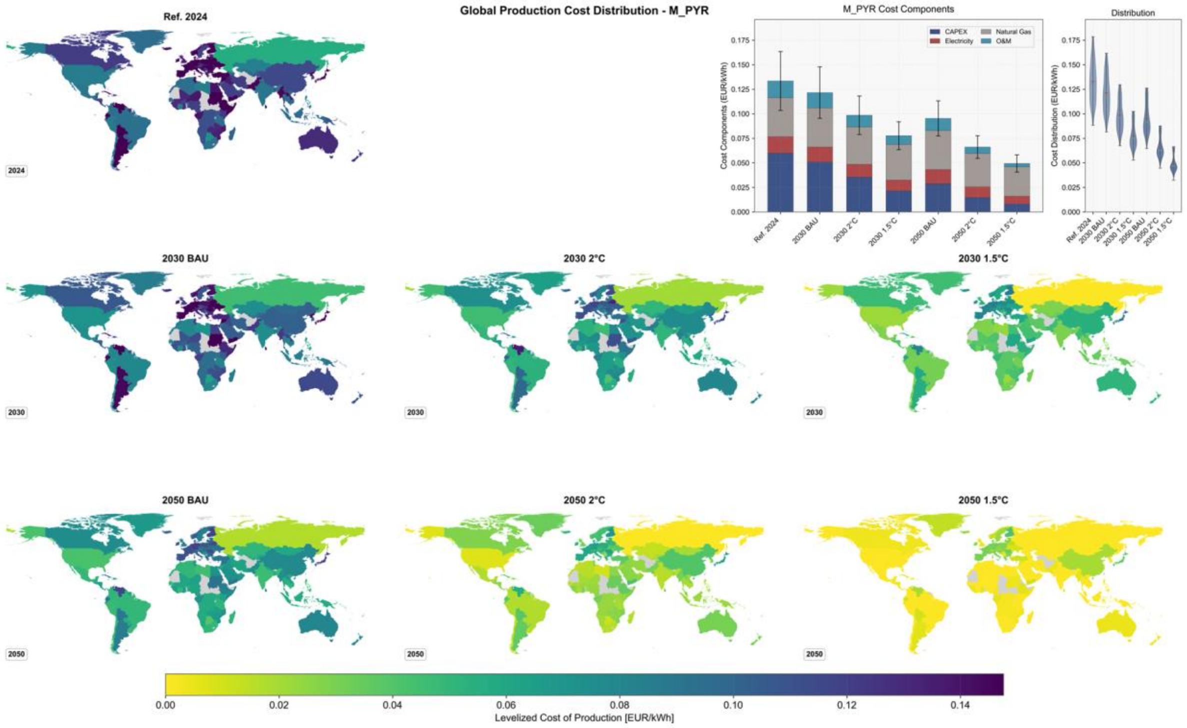

Fig. S14 Global production cost distribution for methane pyrolysis (M_PYR) under various scenarios. The series of maps spans 2024 through the BAU, 2 °C, and 1.5 °C scenarios in 2030 and 2050, using a color gradient to represent LCOH. The bar chart details major cost components, with error bars illustrating cross-country variation. The violin plot indicates the overall spread of costs, showing spread within ±2 SDs.

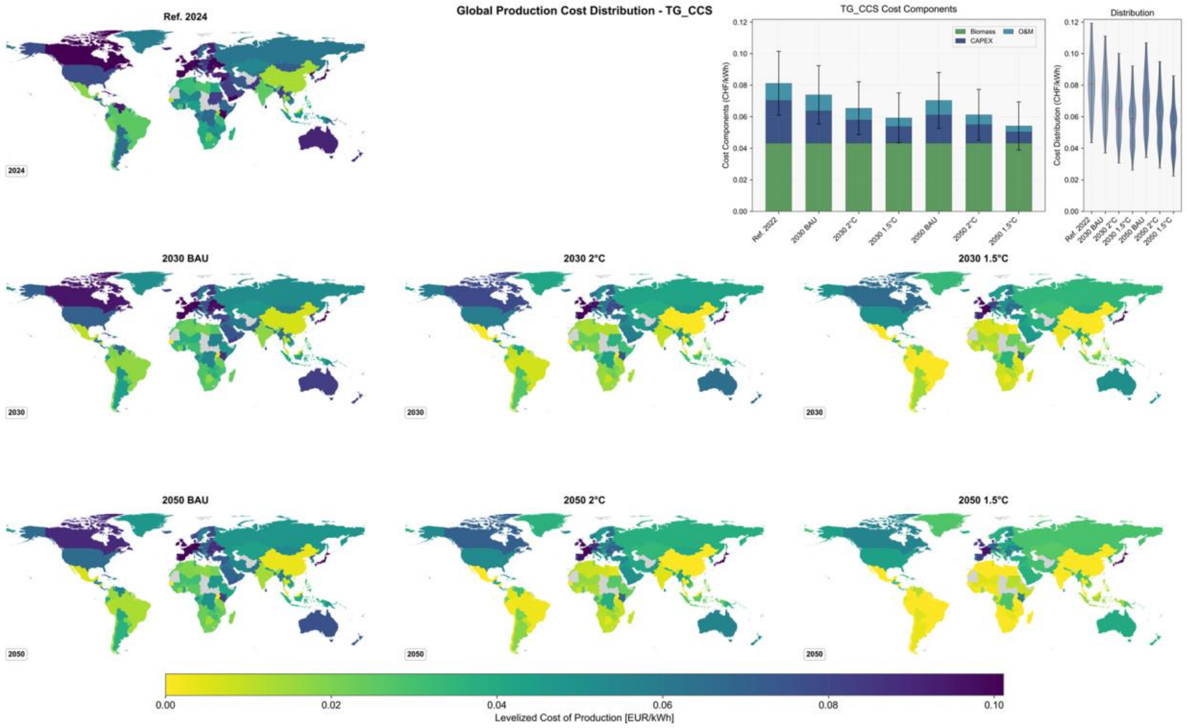

Fig. S15 Global production cost distribution for biomass gasification with CCS for hydrogen production (TG+CCS) across various scenarios. The series of maps spans 2024 through BAU, 2 °C, and 1.5 °C scenarios in 2030 and 2050, using a color gradient from higher (purple) to lower (yellow/green) LCOF. The bar chart details major cost components, with error bars illustrating cross-country variation. The violin plot on the right illustrates the global spread of LCOF values, showing spread within ±2 SDs.

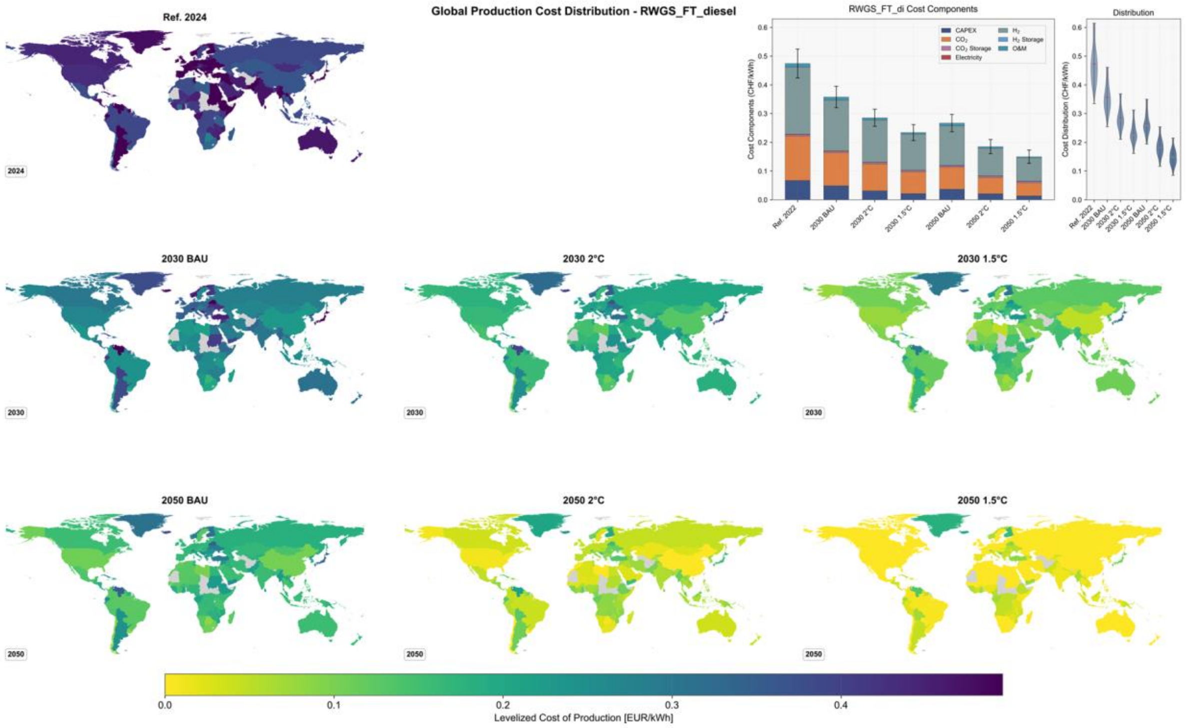

Fig. S16 Global production cost distribution for RWGS-FT-diesel under various scenarios and timeframes. The top-left map represents the reference year 2024, followed by three scenarios (BAU, 2 °C, 1.5 °C) in 2030 and again in 2050, with a color scale transitioning from lower (yellow/green) to higher (purple) levelized costs. The bar chart to the right shows cost component breakdowns (e.g., electricity, hydrogen input, capital expenditures), while error bars reflect standard deviations among countries. The violin plot illustrates the global cost distribution, showing spread within ±2 SDs.

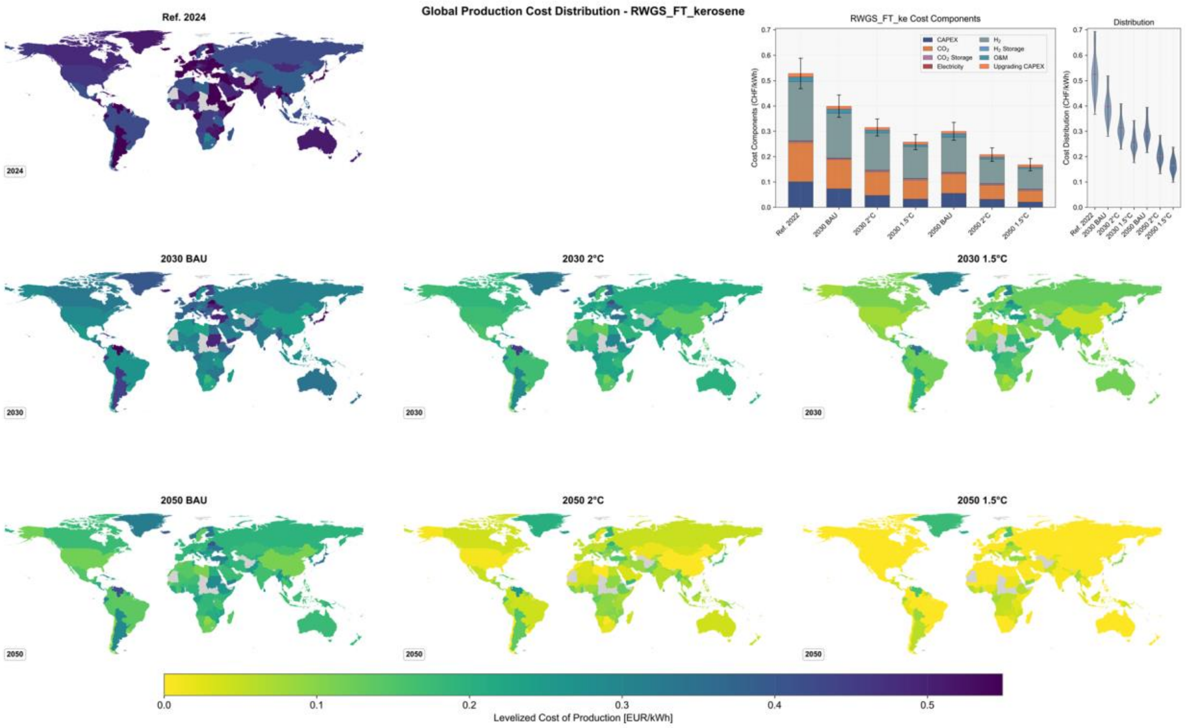

Fig. S17 Global production cost distribution for RWGS-FT-kerosene under various scenarios and timeframes. The top-left map represents the reference year 2024, followed by three scenarios (BAU, 2 °C, 1.5 °C) in 2030 and again in 2050, with a color scale transitioning from lower (yellow/green) to higher (purple) levelized costs. The bar chart to the right shows cost component breakdowns (e.g., electricity, hydrogen input, capital expenditures), while error bars reflect standard deviations among countries. The violin plot illustrates the global cost distribution, showing spread within ±2 SDs.

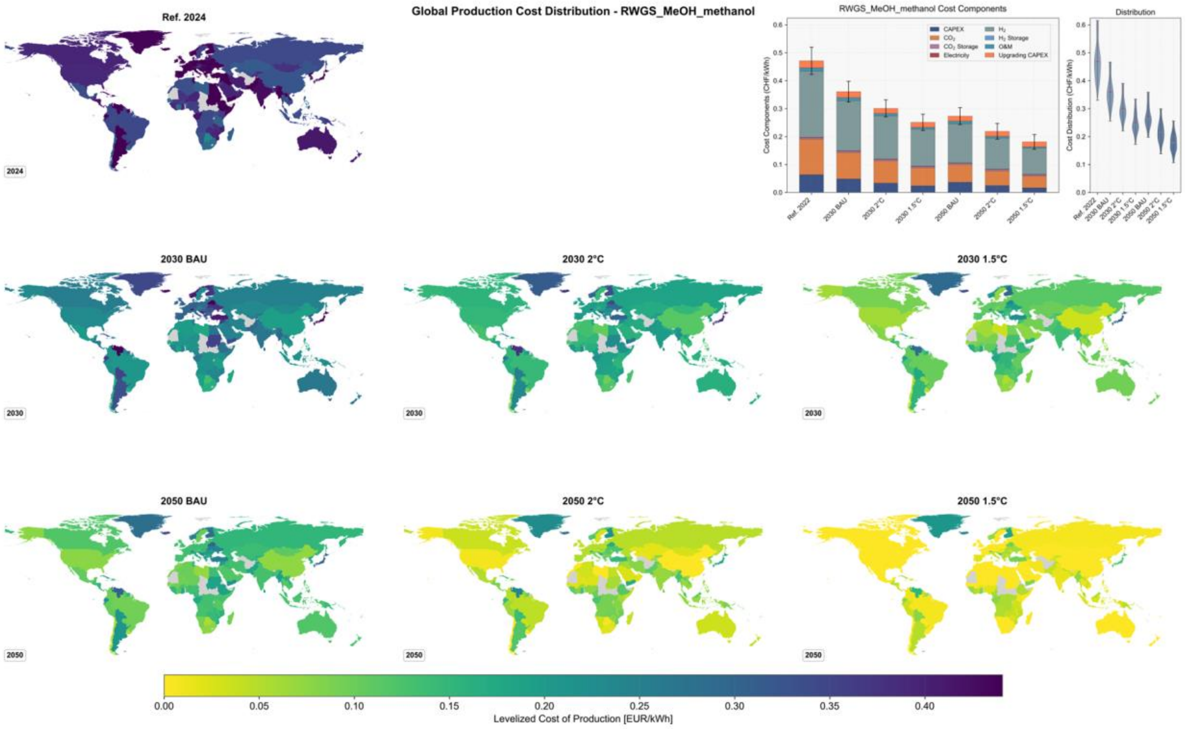

Fig. S18 Global production cost distribution for RWGS-MeOH-methanol under various scenarios and timeframes. The top-left map represents the reference year 2024, followed by three scenarios (BAU, 2 °C, 1.5 °C) in 2030 and again in 2050, with a color scale transitioning from lower (yellow/green) to higher (purple) levelized costs. The bar chart to the right shows cost component breakdowns (e.g., electricity, hydrogen input, capital expenditures), while error bars reflect standard deviations among countries. The violin plot illustrates the global cost distribution, showing spread within ±2 SDs.

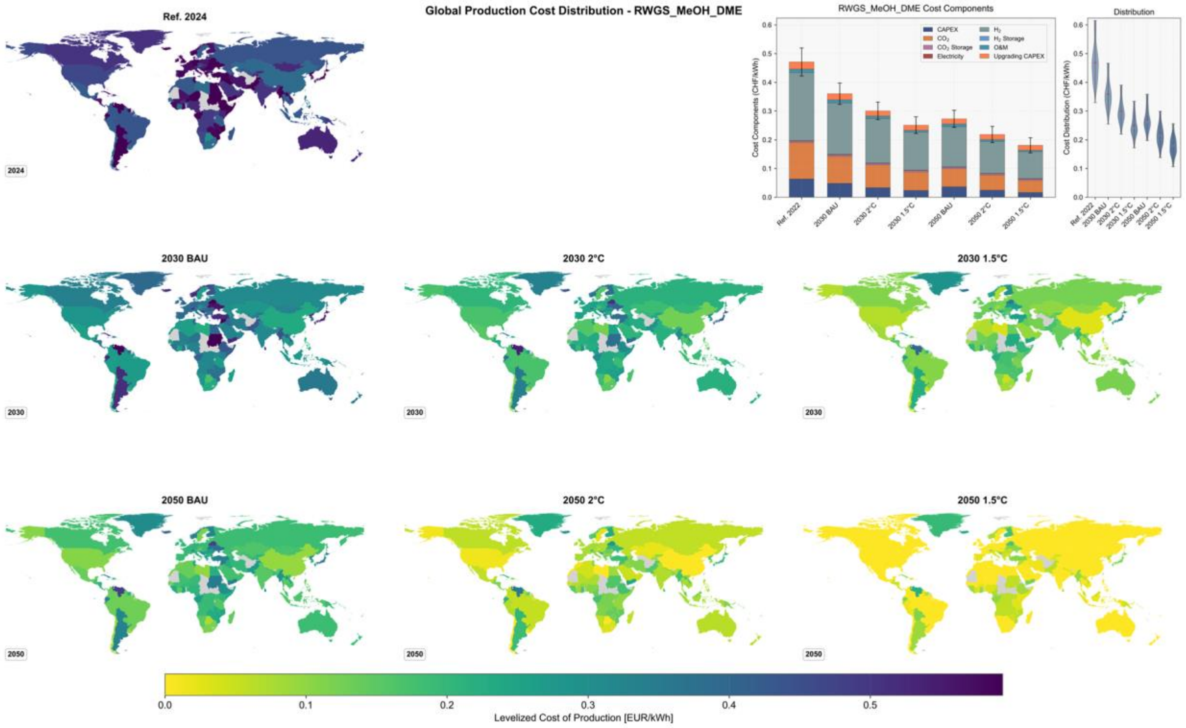

Fig. S19 Global production cost distribution for RWGS-MeOH-DME under various scenarios and timeframes. The top-left map represents the reference year 2024, followed by three scenarios (BAU, 2 °C, 1.5 °C) in 2030 and again in 2050, with a color scale transitioning from lower (yellow/green) to higher (purple) levelized costs. The bar chart to the right shows cost component breakdowns (e.g., electricity, hydrogen input, capital expenditures), while error bars reflect standard deviations among countries. The violin plot illustrates the global cost distribution, showing spread within ±2 SDs.

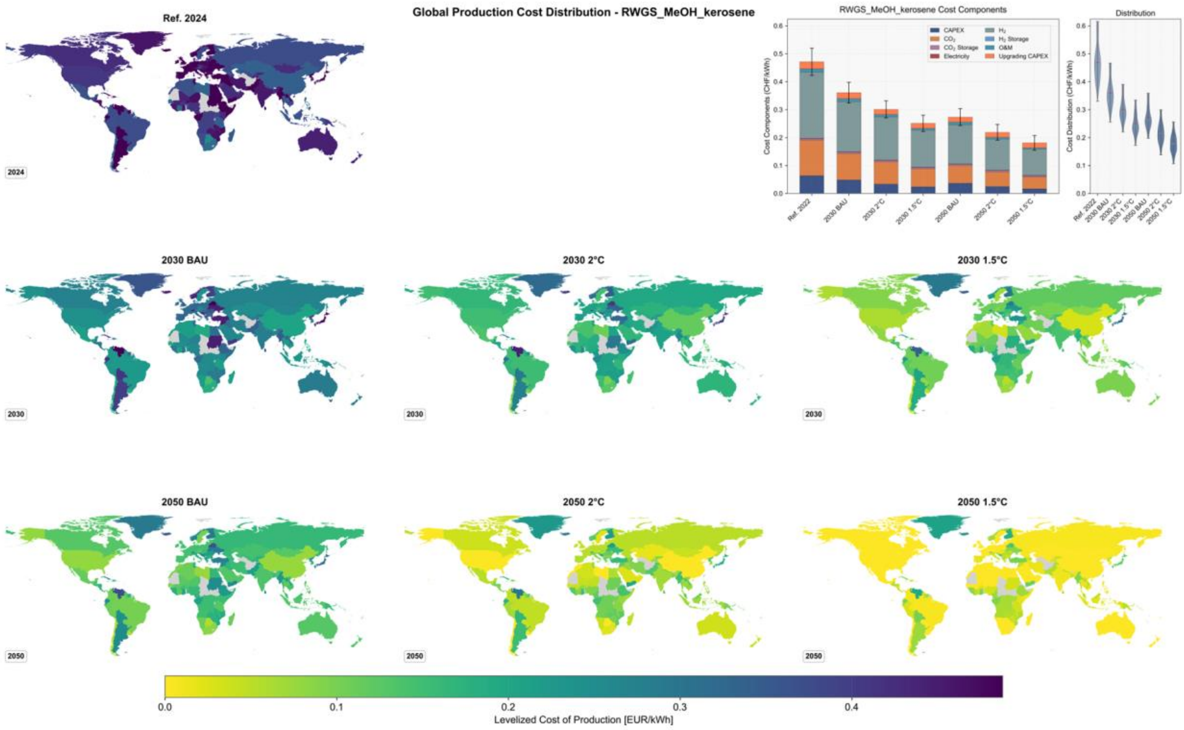

Fig. S20 Global production cost distribution for RWGS-MeOH-kerosene under various scenarios and timeframes. The top-left map represents the reference year 2024, followed by three scenarios (BAU, 2 °C, 1.5 °C) in 2030 and again in 2050, with a color scale transitioning from lower (yellow/green) to higher (purple) levelized costs. The bar chart to the right shows cost component breakdowns (e.g., electricity, hydrogen input, capital expenditures), while error bars reflect standard deviations among countries. The violin plot illustrates the global cost distribution, showing spread within ±2 SDs.

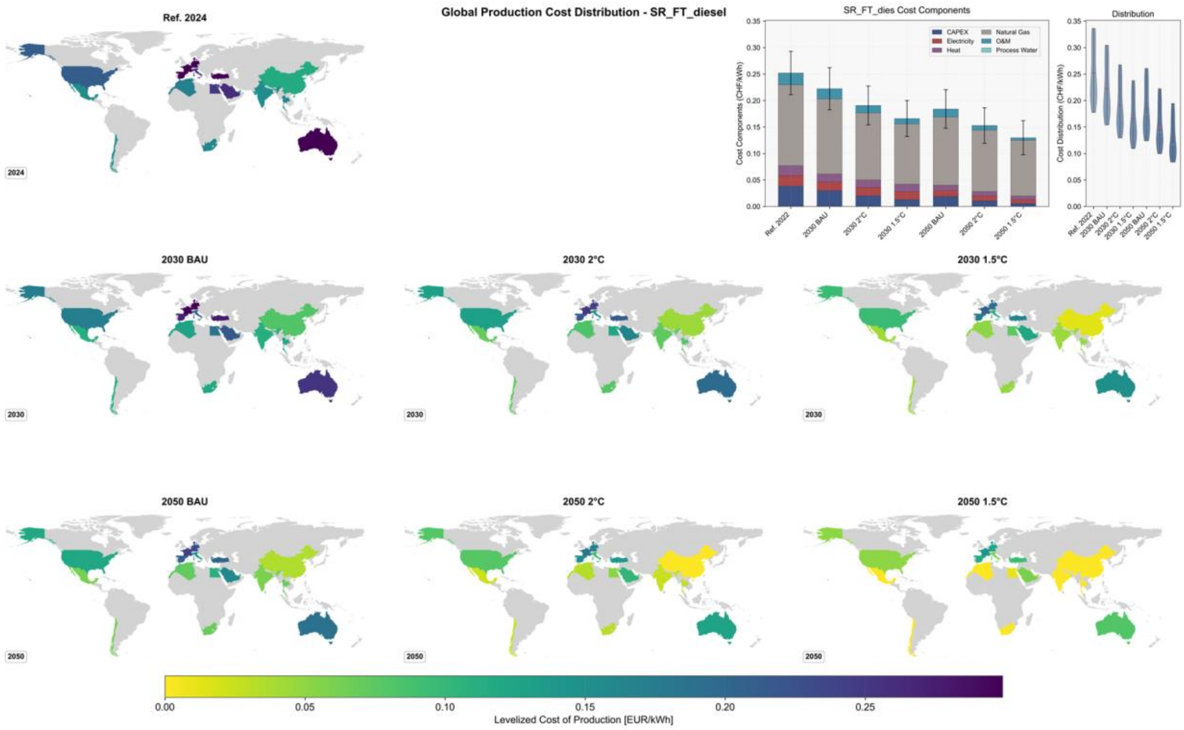

Fig. S21 Global production cost distribution for solar reforming Fischer–Tropsch (SR-FT) diesel under various scenarios and timeframes. The top-left map shows 2024 costs, followed by three scenarios (BAU, 2 °C, 1.5 °C) in 2030 and 2050, using a color scale from lower costs (yellow/green) to higher costs (purple). The bar chart details major cost components, with error bars illustrating cross-country variation. The violin plot on the right illustrates the global spread of LCOF values, showing spread within ±2 SDs.

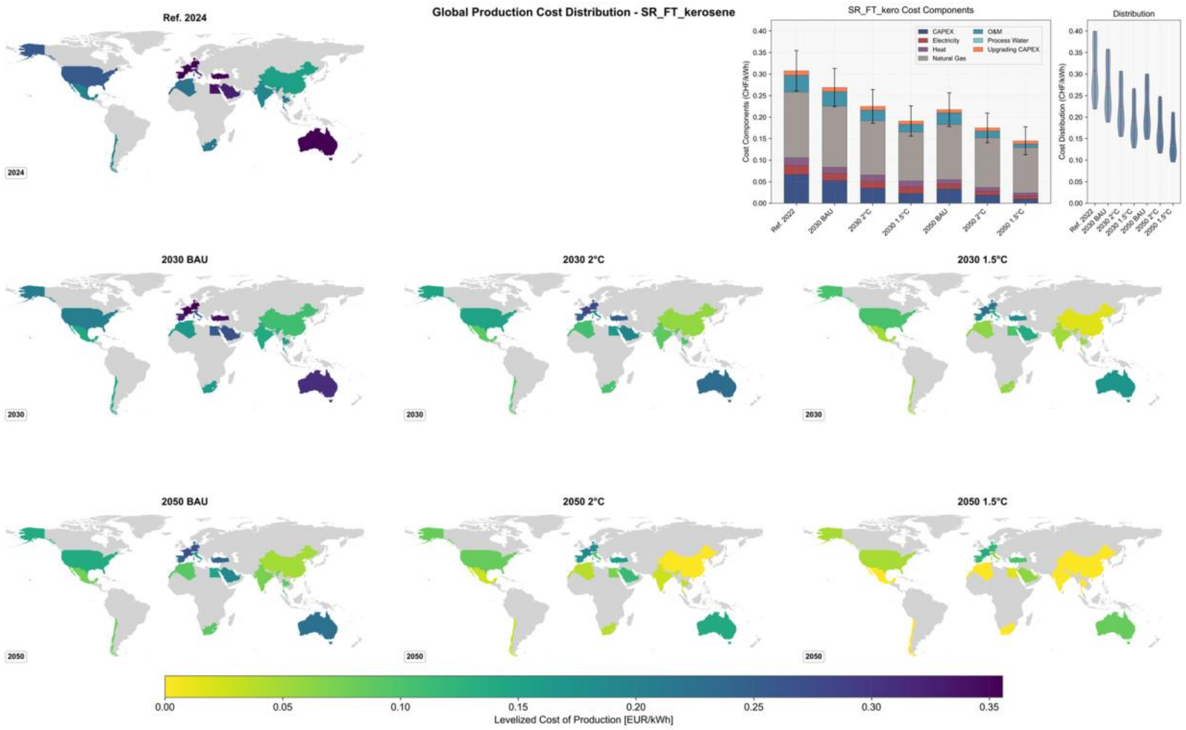

Fig. S22 Global production cost distribution for solar reforming Fischer–Tropsch (SR-FT) kerosene under various scenarios and timeframes. The top-left map shows 2024 costs, followed by three scenarios (BAU, 2 °C, 1.5 °C) in 2030 and 2050, using a color scale from lower costs (yellow/green) to higher costs (purple). The bar chart details major cost components, with error bars illustrating cross-country variation. The violin plot on the right illustrates the global spread of LCOF values, showing spread within ±2 SDs.

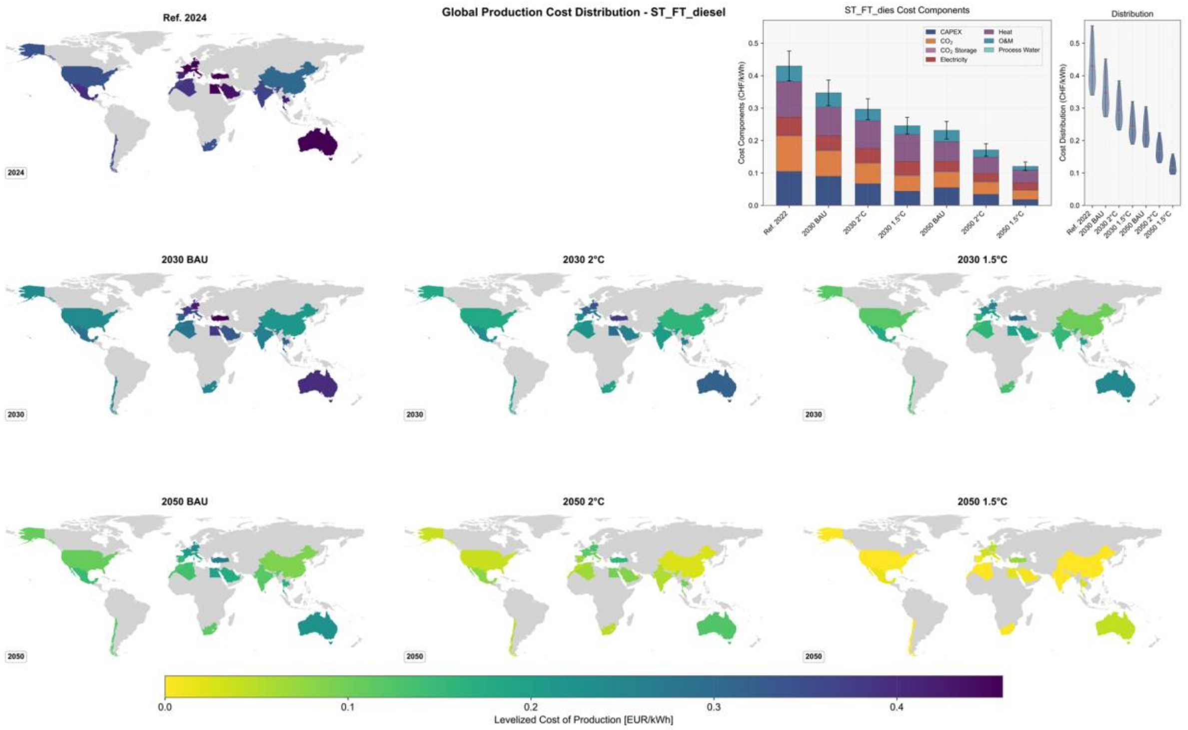

Fig. S23 Global production cost distribution for solar thermochemical Fischer–Tropsch (ST-FT) diesel under various scenarios and timeframes. The series of maps spans 2024 through BAU, 2 °C, and 1.5 °C scenarios in 2030 and 2050, using a color gradient from higher (purple) to lower (yellow/green) LCOF. The bar chart details major cost components, with error bars illustrating cross-country variation. The violin plot on the right illustrates the global spread of LCOF values, showing spread within ±2 SDs.

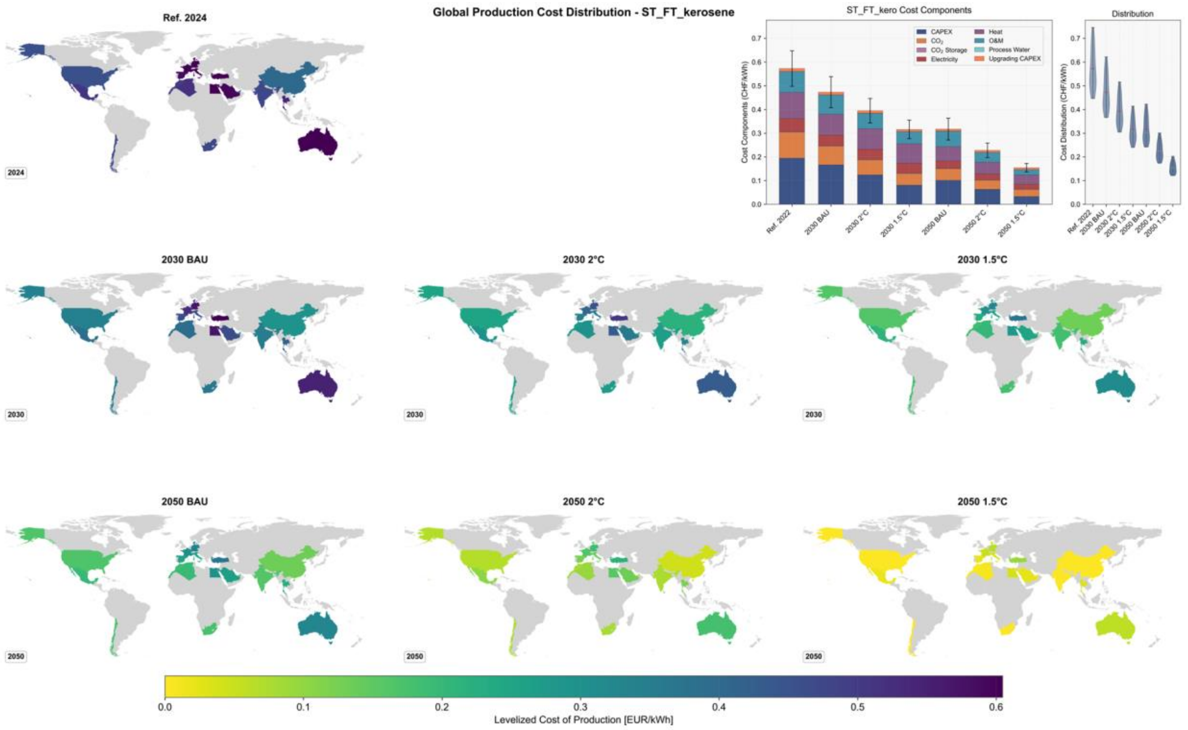

Fig. S24 Global production cost distribution for solar thermochemical Fischer–Tropsch (ST-FT) kerosene under various scenarios and timeframes. The series of maps spans 2024 through BAU, 2 °C, and 1.5 °C scenarios in 2030 and 2050, using a color gradient from higher (purple) to lower (yellow/green) LCOF. The bar chart details major cost components, with error bars illustrating cross-country variation. The violin plot on the right illustrates the global spread of LCOF values, showing spread within ±2 SDs.

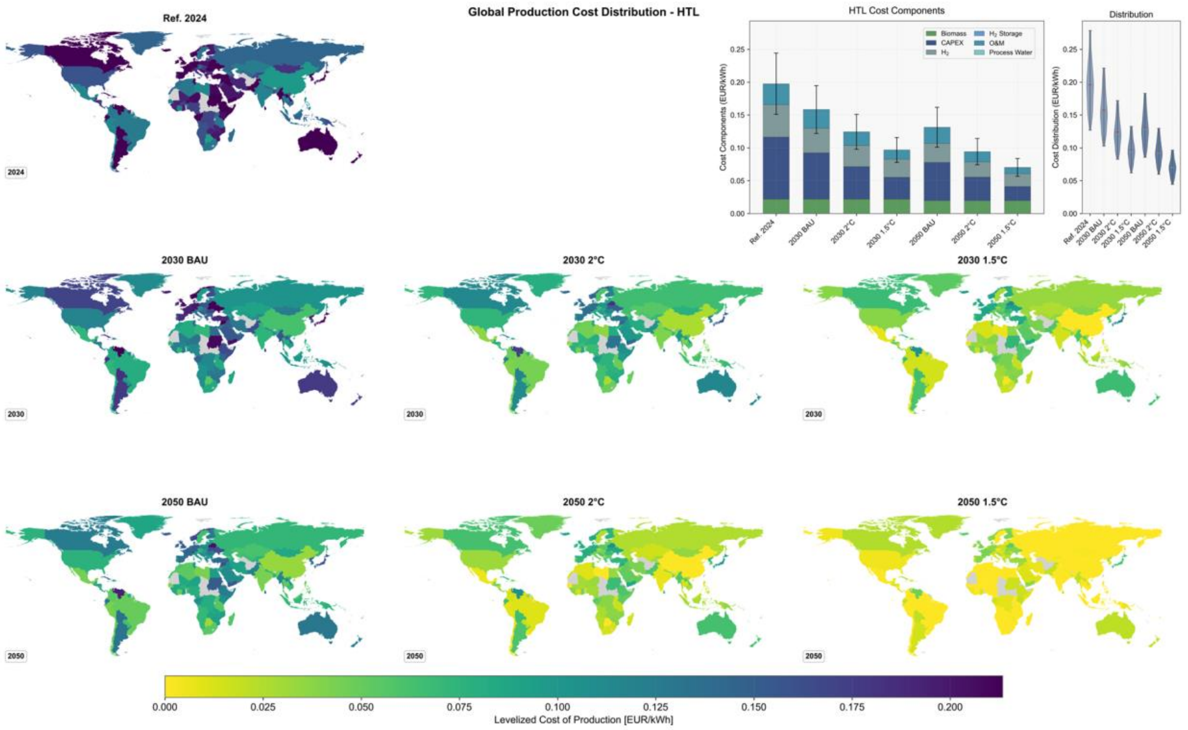

Fig. S25 Global production cost distribution for HTL kerosene under various scenarios and timeframes. The series of maps spans 2024 through BAU, 2 °C, and 1.5 °C scenarios in 2030 and 2050, using a color gradient from higher (purple) to lower (yellow/green) LCOF. The bar chart details major cost components, with error bars illustrating cross-country variation. The violin plot on the right illustrates the global spread of LCOF values, showing spread within ±2 SDs.

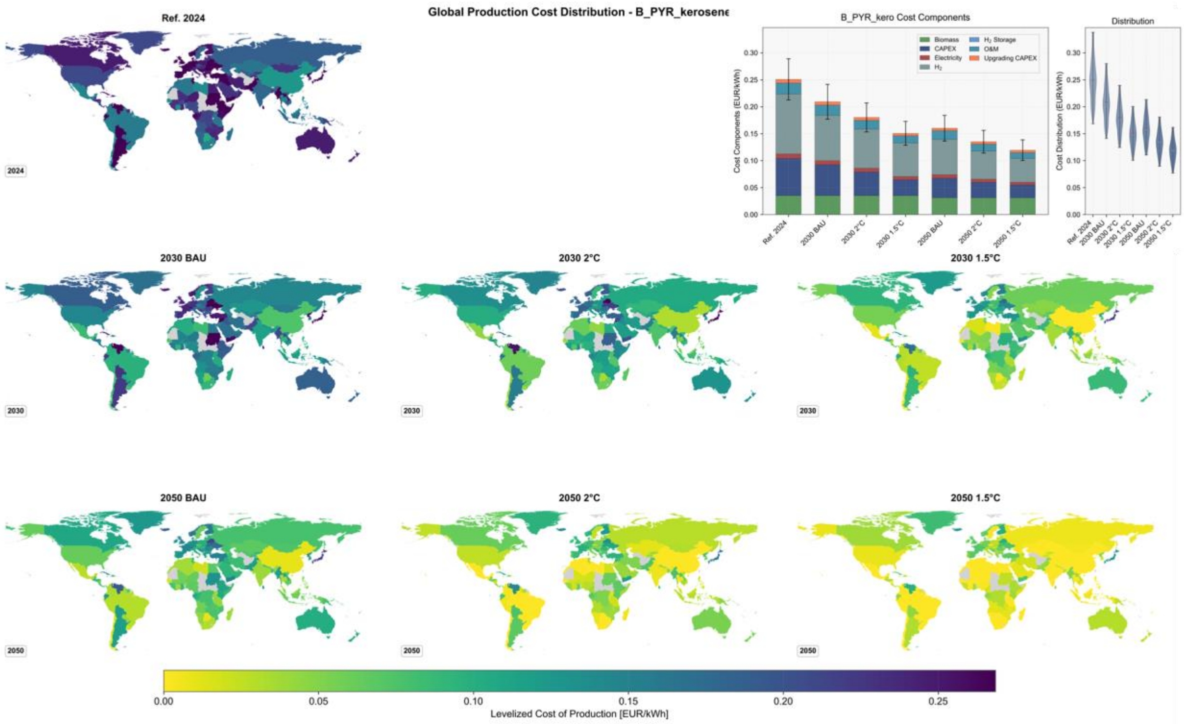

Fig. S26 Global production cost distribution for biomass pyrolysis kerosene (B_PYR) under various scenarios and timeframes. The series of maps spans 2024 through BAU, 2 °C, and 1.5 °C scenarios in 2030 and 2050, using a color gradient from higher (purple) to lower (yellow/green) LCOF. The bar chart details major cost components, with error bars illustrating cross-country variation. The violin plot on the right illustrates the global spread of LCOF values, showing spread within ±2 SDs.

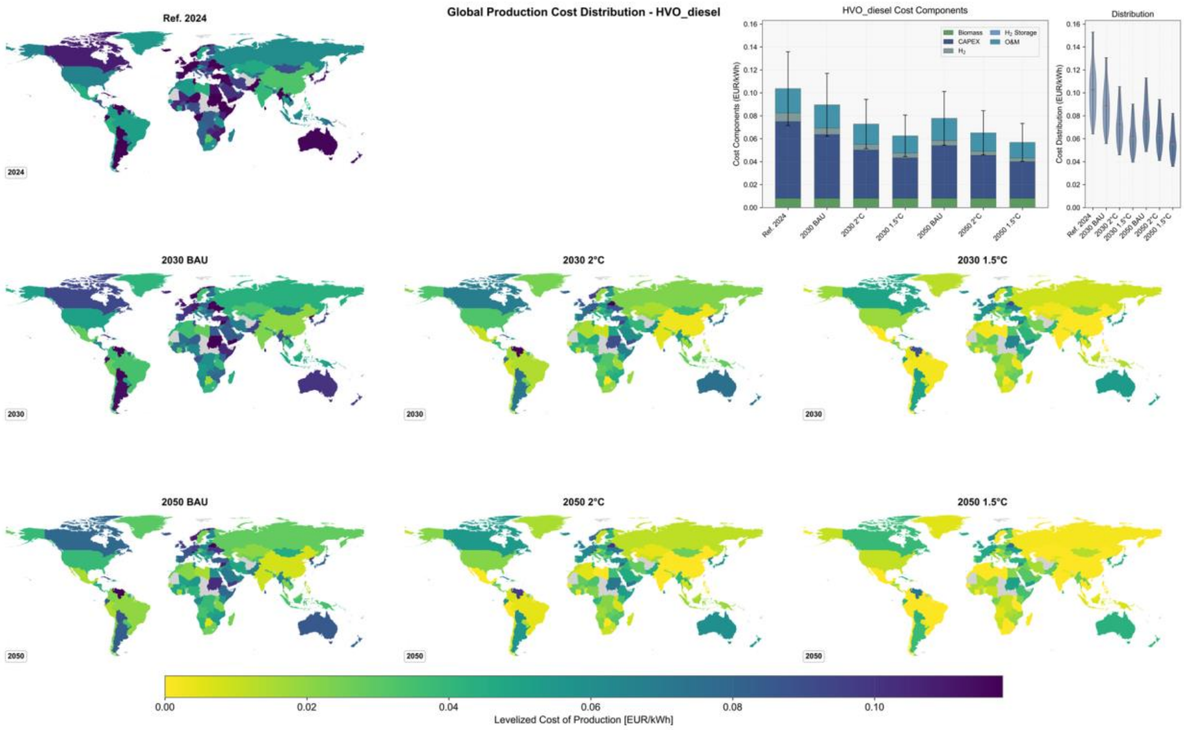

Fig. S27 Global production cost distribution for HVO diesel under various scenarios and timeframes. The series of maps spans 2024 through BAU, 2 °C, and 1.5 °C scenarios in 2030 and 2050, using a color gradient from higher (purple) to lower (yellow/green) LCOF.

The bar chart details major cost components, with error bars illustrating cross-country variation. The violin plot on the right illustrates the global spread of LCOF values, showing spread within ±2 SDs.

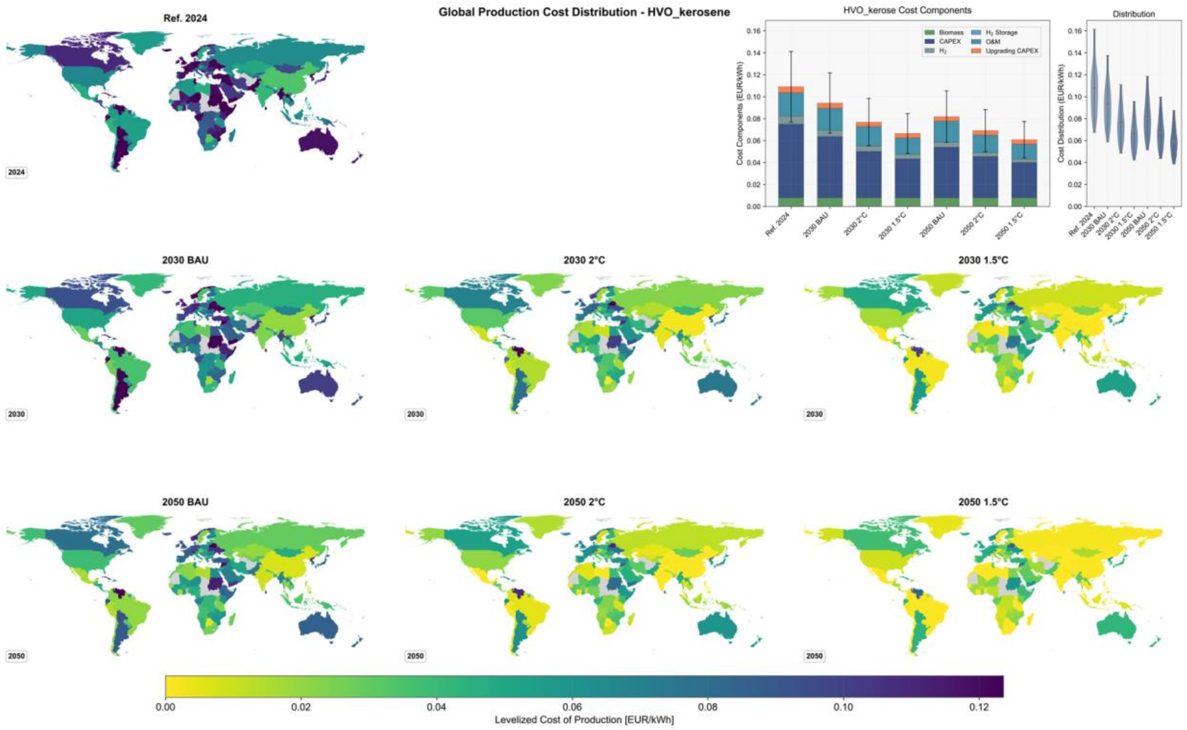

Fig. S28 Global production cost distribution for HVO kerosene under various scenarios and timeframes. The series of maps spans 2024 through BAU, 2 °C, and 1.5 °C scenarios in 2030 and 2050, using a color gradient from higher (purple) to lower (yellow/green) LCOF. The bar chart details major cost components, with error bars illustrating cross-country variation. The violin plot on the right illustrates the global spread of LCOF values, showing spread within ±2 SDs.

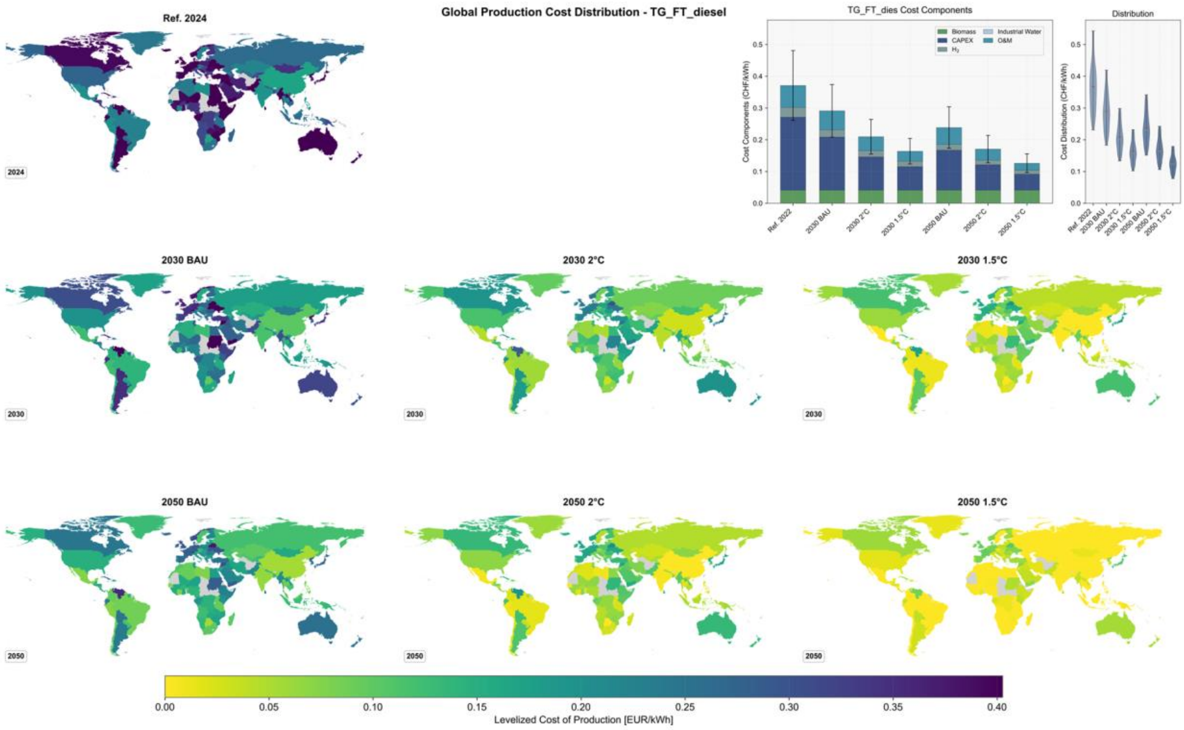

Fig. S29 Global production cost distribution for TG-FT diesel under various scenarios and timeframes. The series of maps spans 2024 through BAU, 2 °C, and 1.5 °C scenarios in 2030 and 2050, using a color gradient from higher (purple) to lower (yellow/green) LCOF. The bar chart details major cost components, with error bars illustrating cross-country variation. The violin plot on the right illustrates the global spread of LCOF values, showing spread within ±2 SDs.

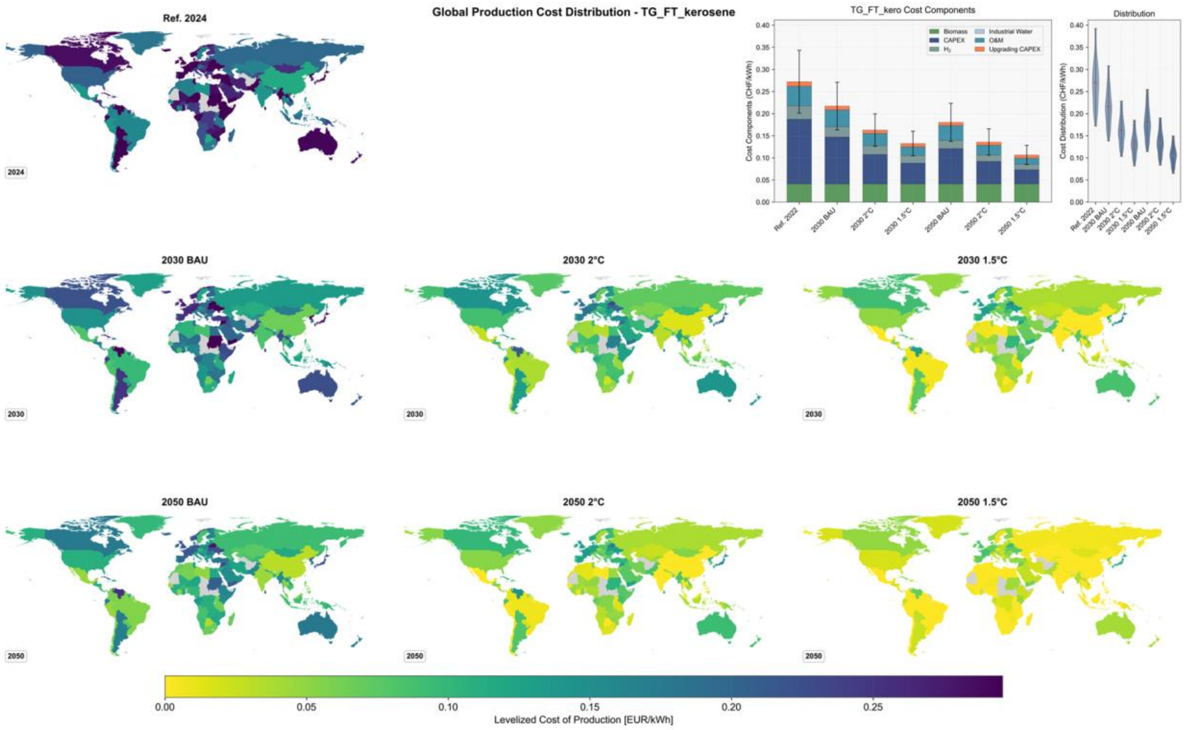

Fig. S30 Global production cost distribution for TG-FT kerosene under various scenarios and timeframes. The series of maps spans 2024 through BAU, 2 °C, and 1.5 °C scenarios in 2030 and 2050, using a color gradient from higher (purple) to lower (yellow/green) LCOF.

The bar chart details major cost components, with error bars illustrating cross-country variation. The violin plot on the right illustrates the global spread of LCOF values, showing spread within ±2 SDs.

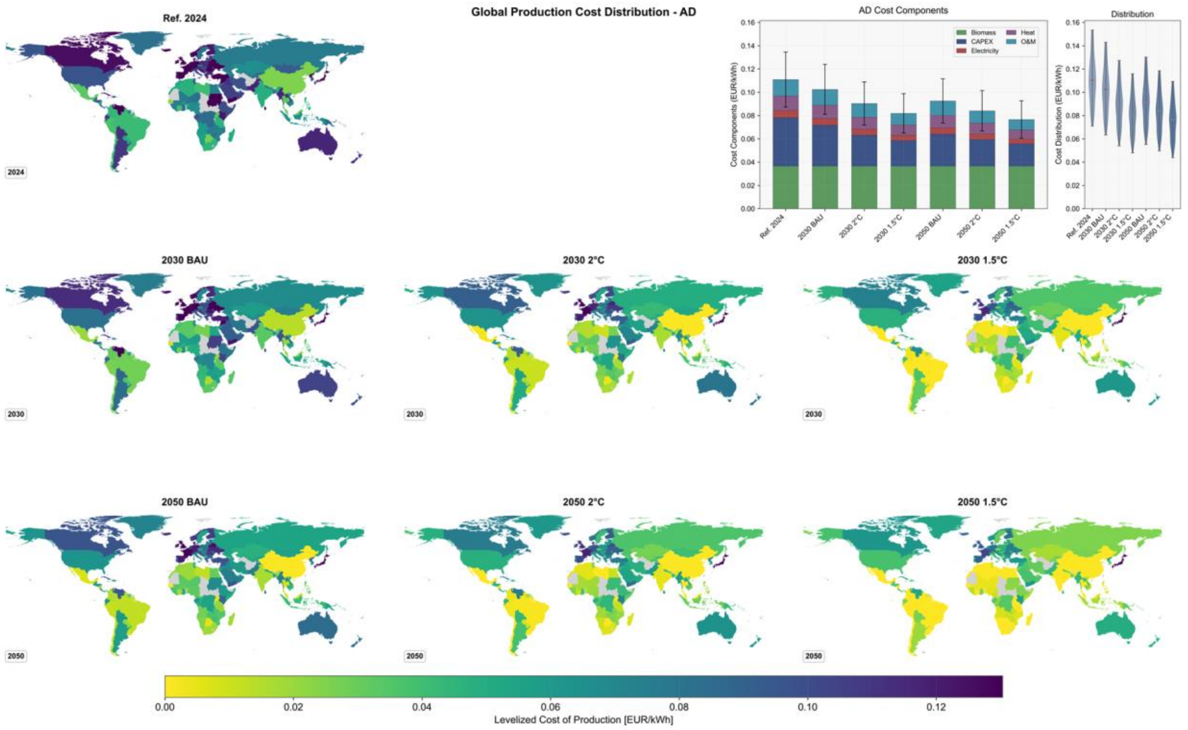

Fig. S31 Global production cost distribution for AD methane under various scenarios and timeframes. The series of maps spans 2024 through BAU, 2 °C, and 1.5 °C scenarios in 2030 and 2050, using a color gradient from higher (purple) to lower (yellow/green) LCOF. The bar chart details major cost components, with error bars illustrating cross-country variation. The violin plot on the right illustrates the global spread of LCOF values, showing spread within ±2 SDs.

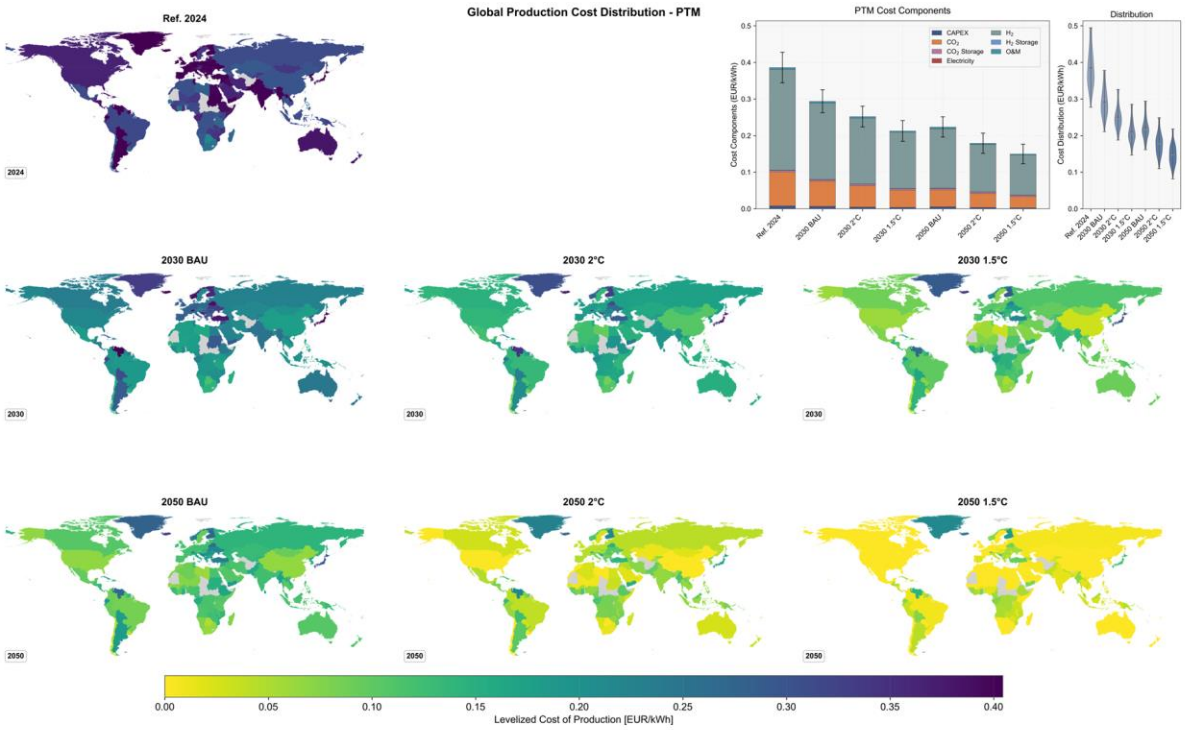

Fig. S32 Global production cost distribution for PTM methane under various scenarios and timeframes. The series of maps spans 2024 through BAU, 2 °C, and 1.5 °C scenarios in 2030 and 2050, using a color gradient from higher (purple) to lower (yellow/green) LCOF. The bar chart details major cost components, with error bars illustrating cross-country variation. The violin plot on the right illustrates the global spread of LCOF values, showing spread within ±2 SDs.

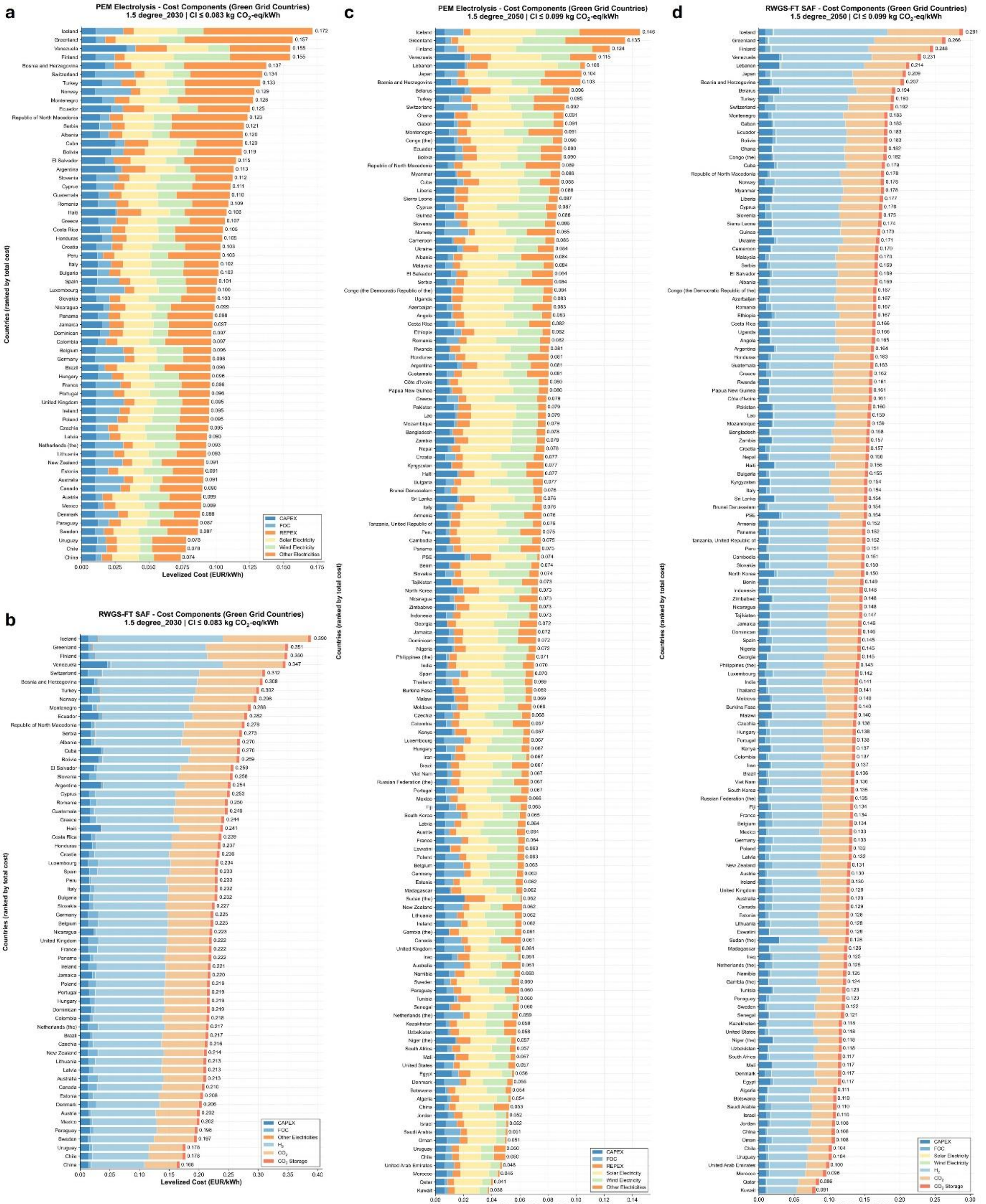

Fig. S33 Global costs and cost-component breakdowns for green hydrogen (PEM electrolysis) and synthetic kerosene (PEM-DAC-RWGS-FT) in green-grid-eligible countries under the 1.5 °C scenario. (a) Levelized cost of hydrogen (LCOH) and cost-component breakdown for PEM electrolysis in 2030; (b) Levelized cost of synthetic kerosene (LCOF) via the PEM-DAC-RWGS-FT pathway in 2030; (c) LCOH and cost breakdown for PEM electrolysis in 2050; (d) LCOF for PEM-DAC-RWGS-FT kerosene in 2050.

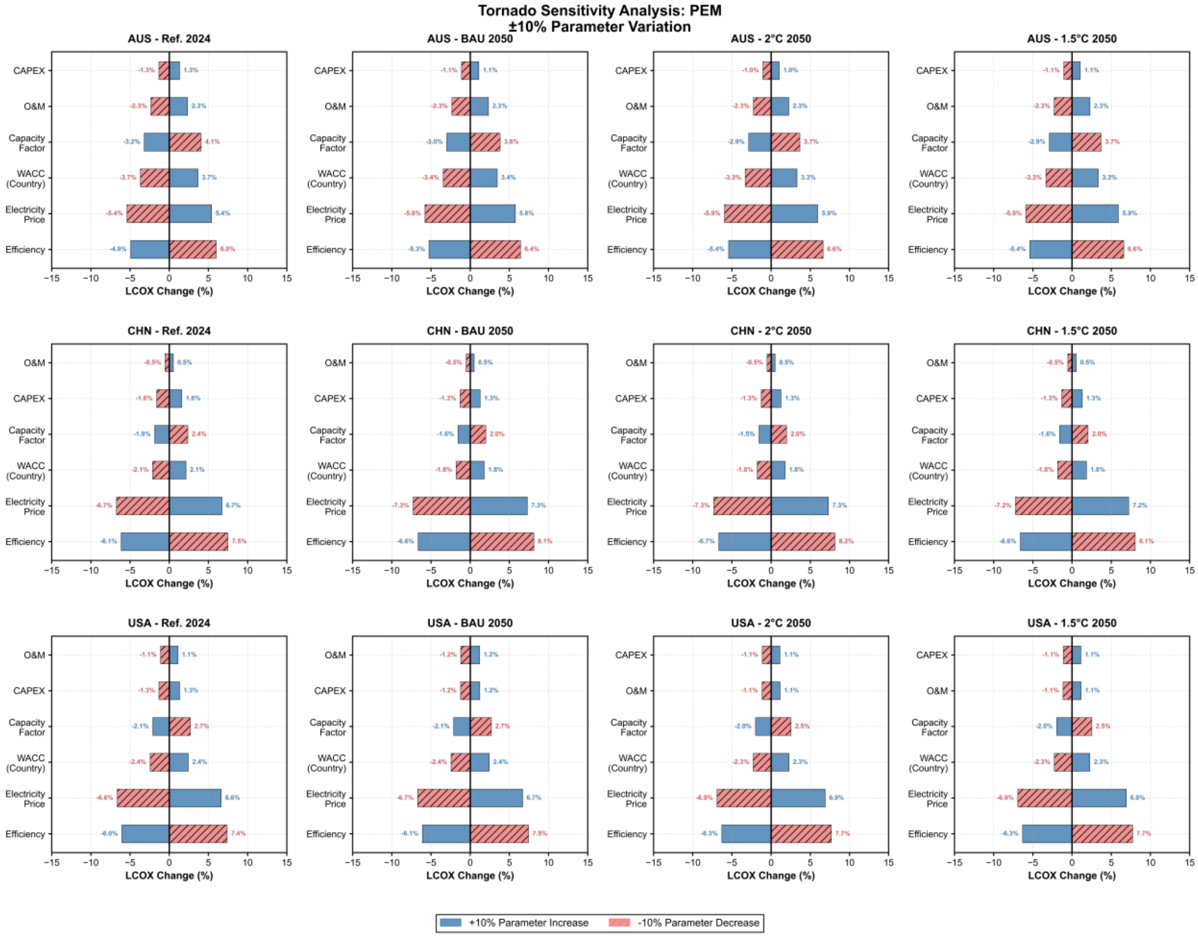

Fig. S34 Tornado sensitivity analysis of levelized hydrogen cost for PEM electrolysis across Australia, China, and USA under different scenarios (Ref. 2024, BAU 2050, 2°C 2050, and 1.5°C 2050). Each parameter was varied by ±20% from its baseline value. Blue bars represent the impact of +20% parameter increase; red hatched bars represent the impact of -20% parameter decrease.

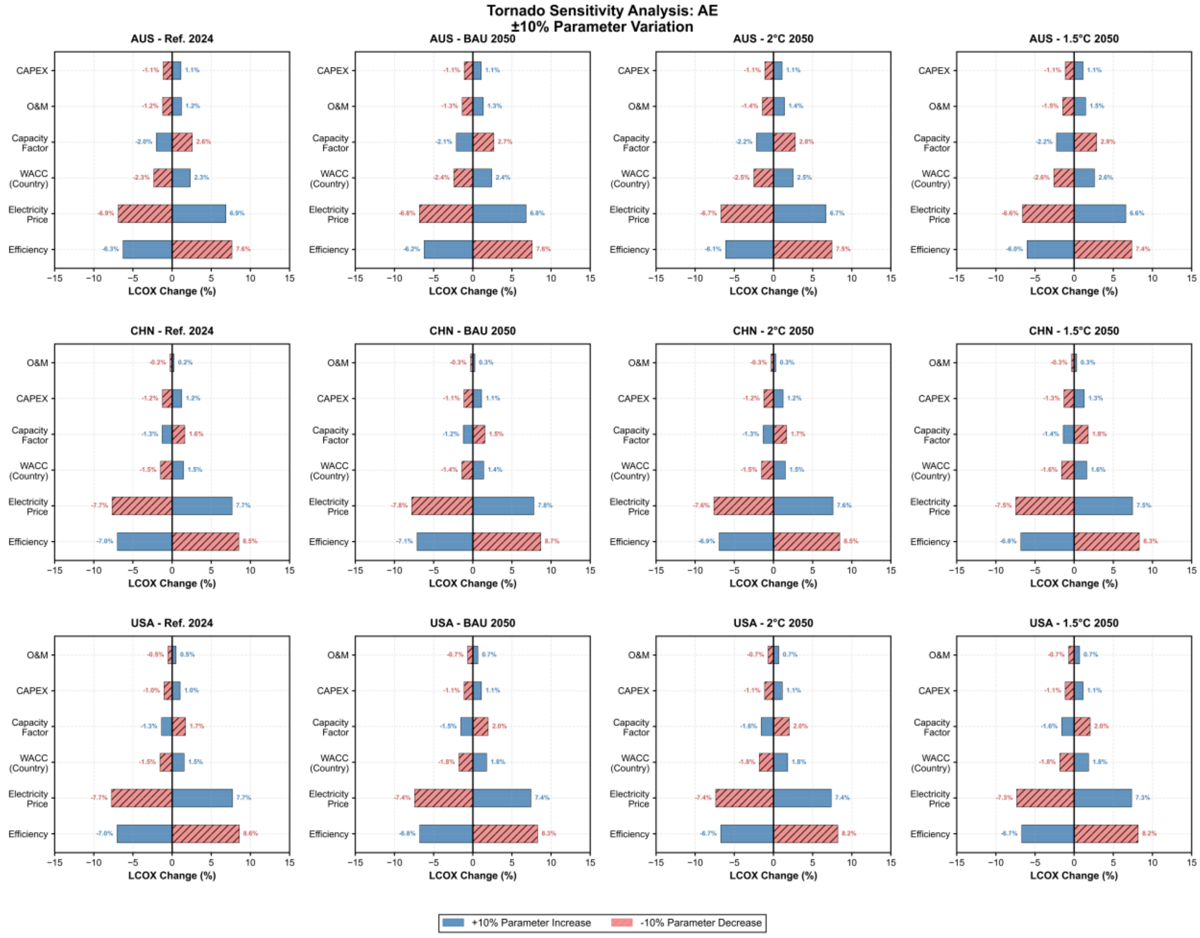

Fig. S35 Tornado sensitivity analysis of levelized hydrogen cost for alkaline electrolysis (AE) across Australia, China, and USA under different scenarios (Ref. 2024, BAU 2050, 2°C 2050, and 1.5°C 2050). Each parameter was varied by ±20% from its baseline value. Blue bars represent the impact of +20% parameter increase; red hatched bars represent the impact of -20% parameter decrease.

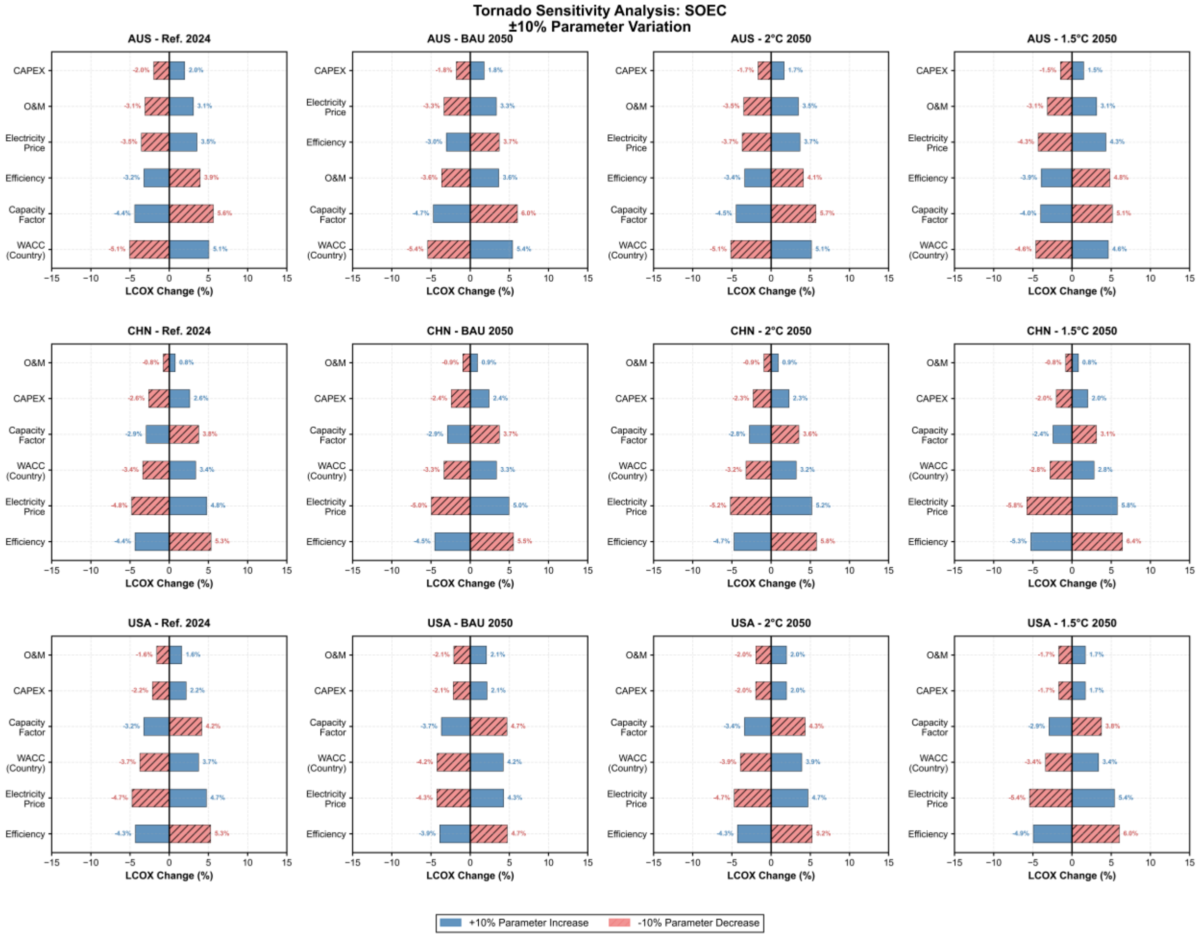

Fig. S36 Tornado sensitivity analysis of levelized hydrogen cost for solid oxide electrolysis cells (SOEC) across Australia, China, and USA under different scenarios (Ref. 2024, BAU 2050, 2°C 2050, and 1.5°C 2050). Each parameter was varied by ±20% from its baseline value. Blue bars represent the impact of +20% parameter increase; red hatched bars represent the impact of -20% parameter decrease.

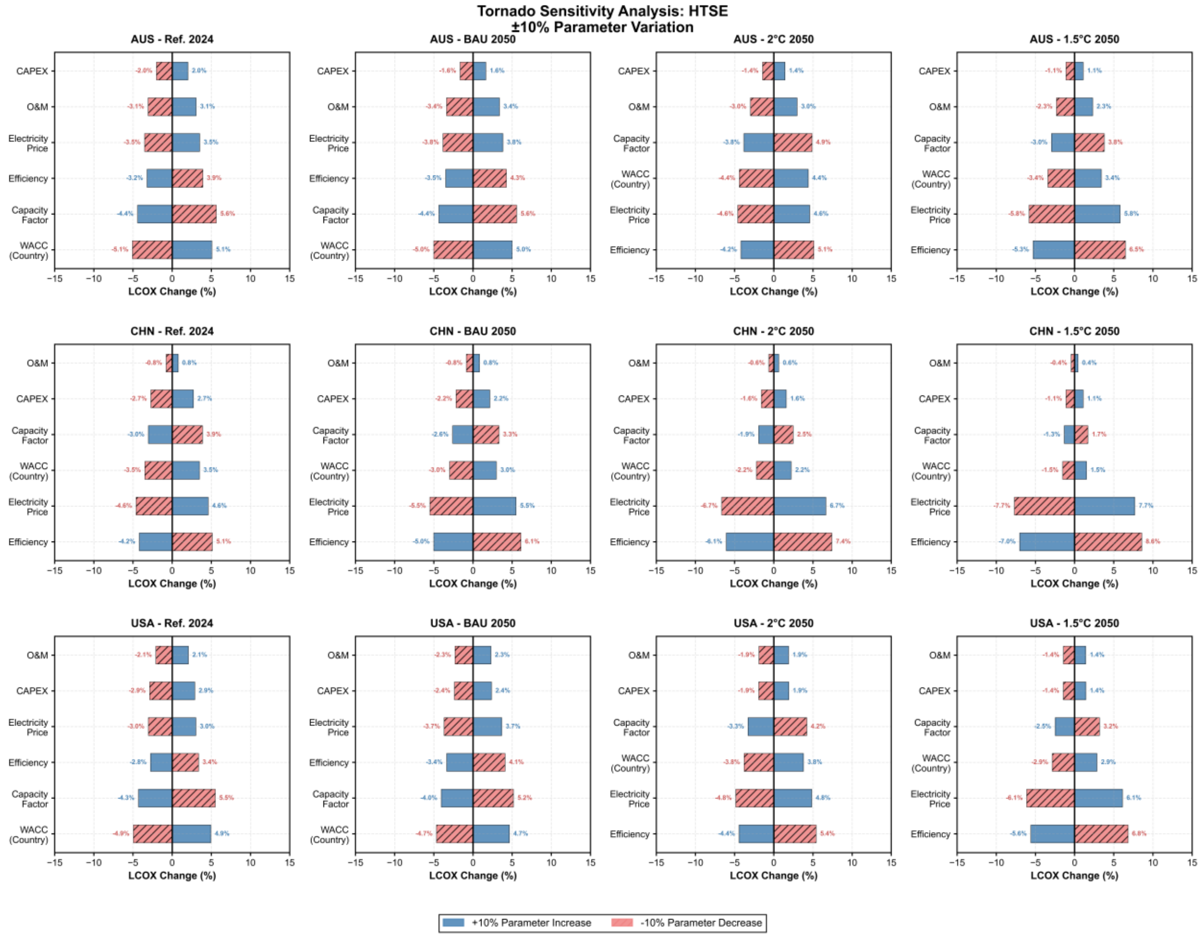

Fig. S37 Tornado sensitivity analysis of levelized hydrogen cost for high-temperature steam electrolysis (HTSE) across Australia, China, and USA under different scenarios (Ref. 2024, BAU 2050, 2°C 2050, and 1.5°C 2050). Each parameter was varied by ±20% from its baseline value. Blue bars represent the impact of +20% parameter increase; red hatched bars represent the impact of -20% parameter decrease.

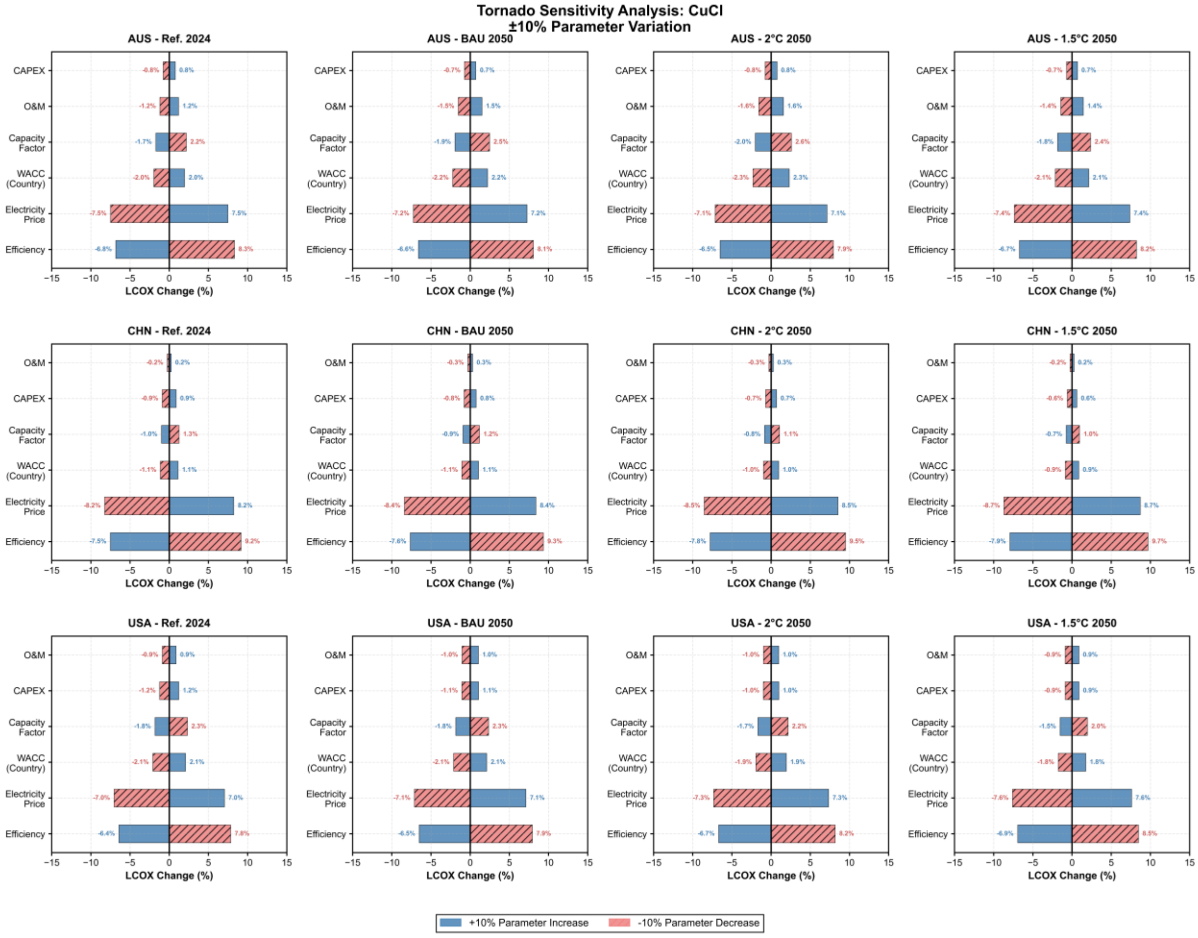

Fig. S38 Tornado sensitivity analysis of levelized hydrogen cost for CuCl thermochemical cycle (CuCl) across Australia, China, and USA under different scenarios (Ref. 2024, BAU 2050, 2°C 2050, and 1.5°C 2050). Each parameter was varied by ±20% from its baseline value. Blue bars represent the impact of +20% parameter increase; red hatched bars represent the impact of -20% parameter decrease.

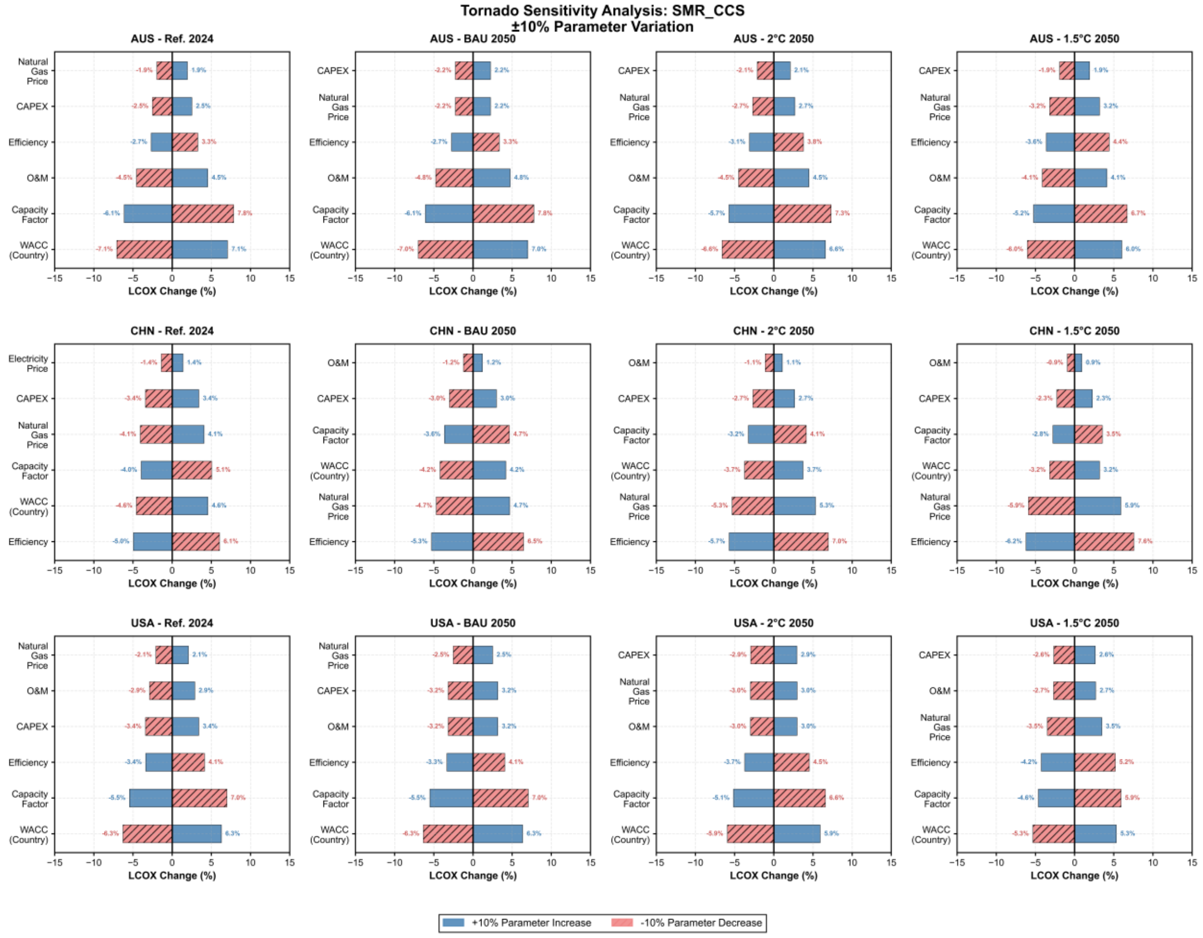

Fig. S39 Tornado sensitivity analysis of levelized hydrogen cost for steam methane reforming with CCS (SMR+CCS) across Australia, China, and USA under different scenarios (Ref. 2024, BAU 2050, 2°C 2050, and 1.5°C 2050). Each parameter was varied by ±20% from its baseline value. Blue bars represent the impact of +20% parameter increase; red hatched bars represent the impact of -20% parameter decrease.

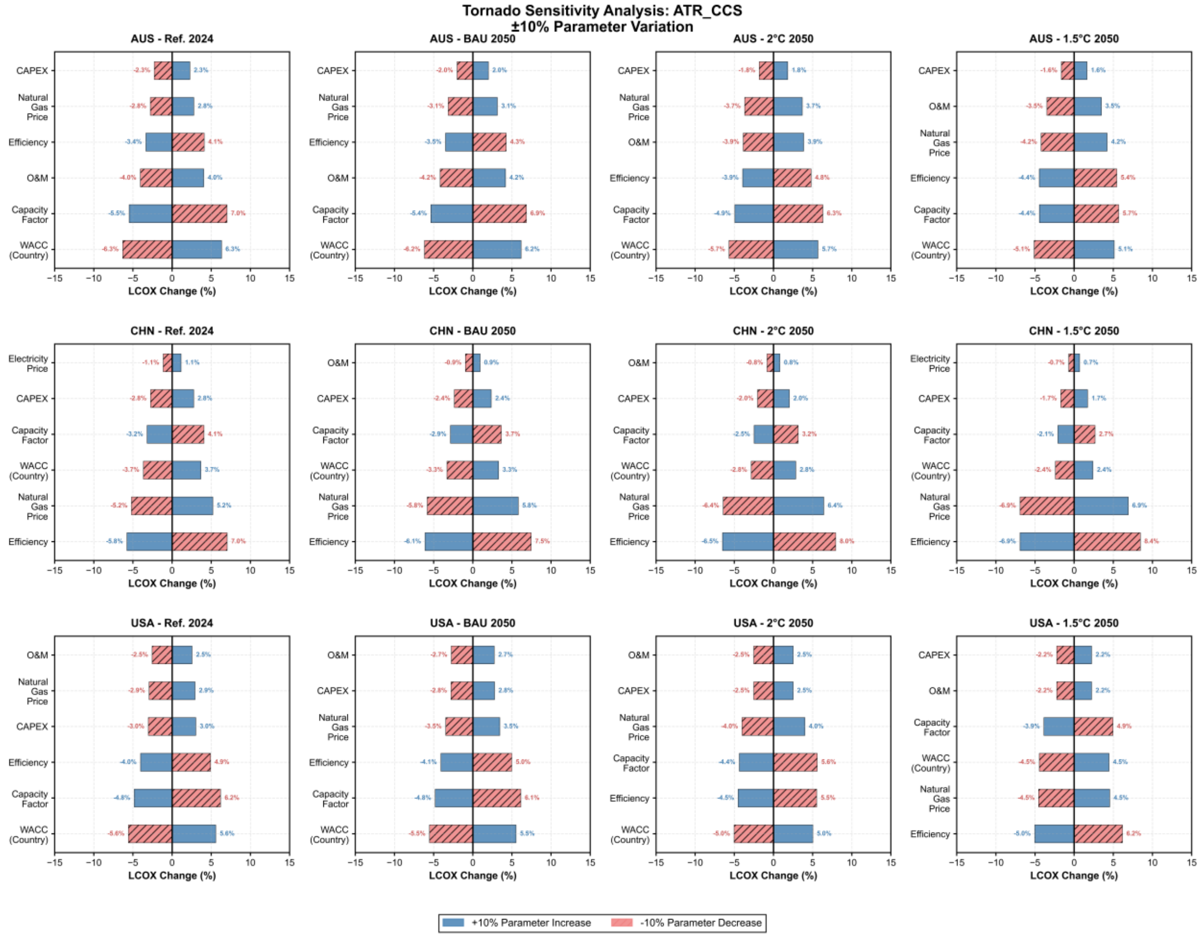

Fig. S40 Tornado sensitivity analysis of levelized hydrogen cost for autothermal reforming with CCS (ATR+CCS) across Australia, China, and USA under different scenarios (Ref. 2024, BAU 2050, 2°C 2050, and 1.5°C 2050). Each parameter was varied by ±20% from its baseline value. Blue bars represent the impact of +20% parameter increase; red hatched bars represent the impact of -20% parameter decrease.

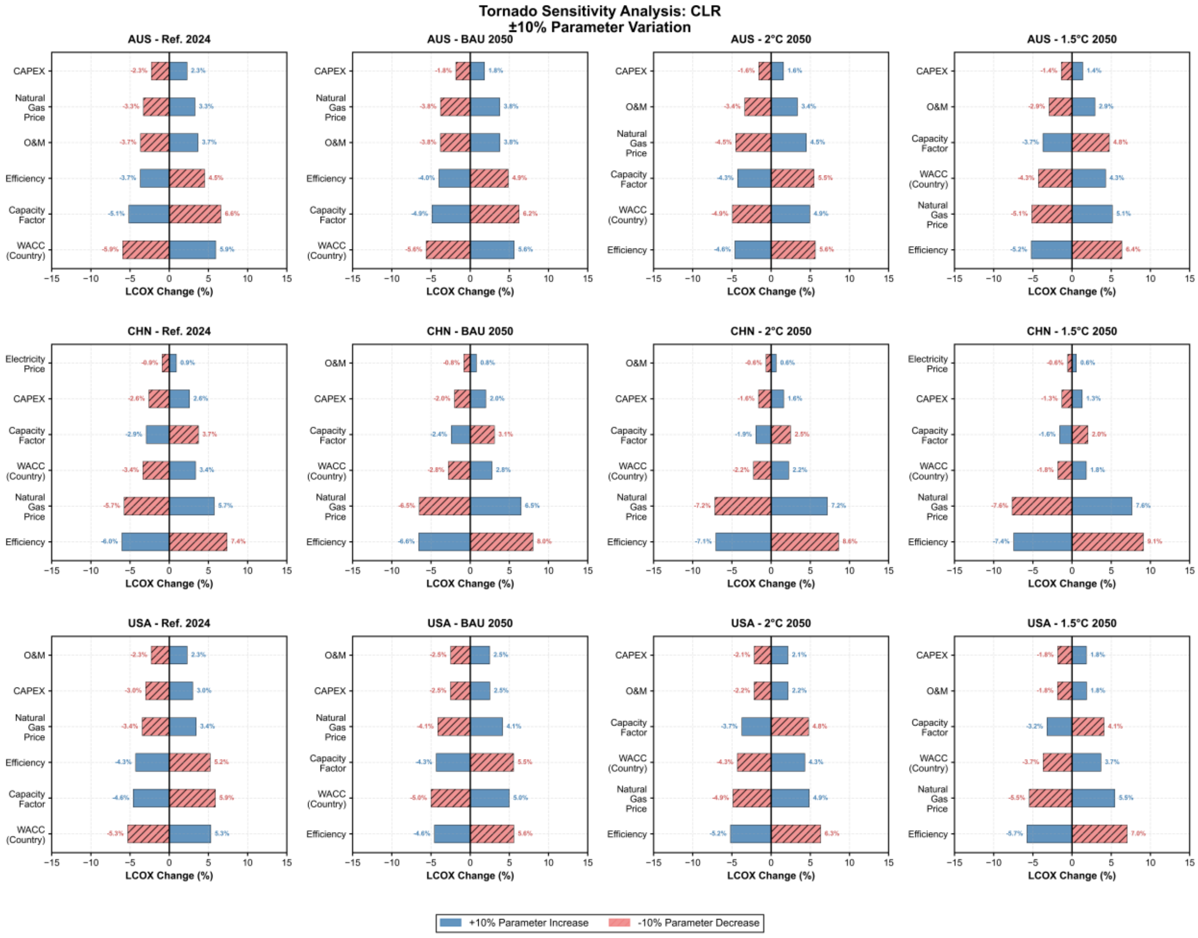

Fig. S41 Tornado sensitivity analysis of levelized hydrogen cost for chemical looping reforming (CLR) across Australia, China, and USA under different scenarios (Ref. 2024, BAU 2050, 2°C 2050, and 1.5°C 2050). Each parameter was varied by ±20% from its baseline value. Blue bars represent the impact of +20% parameter increase; red hatched bars represent the impact of -20% parameter decrease.

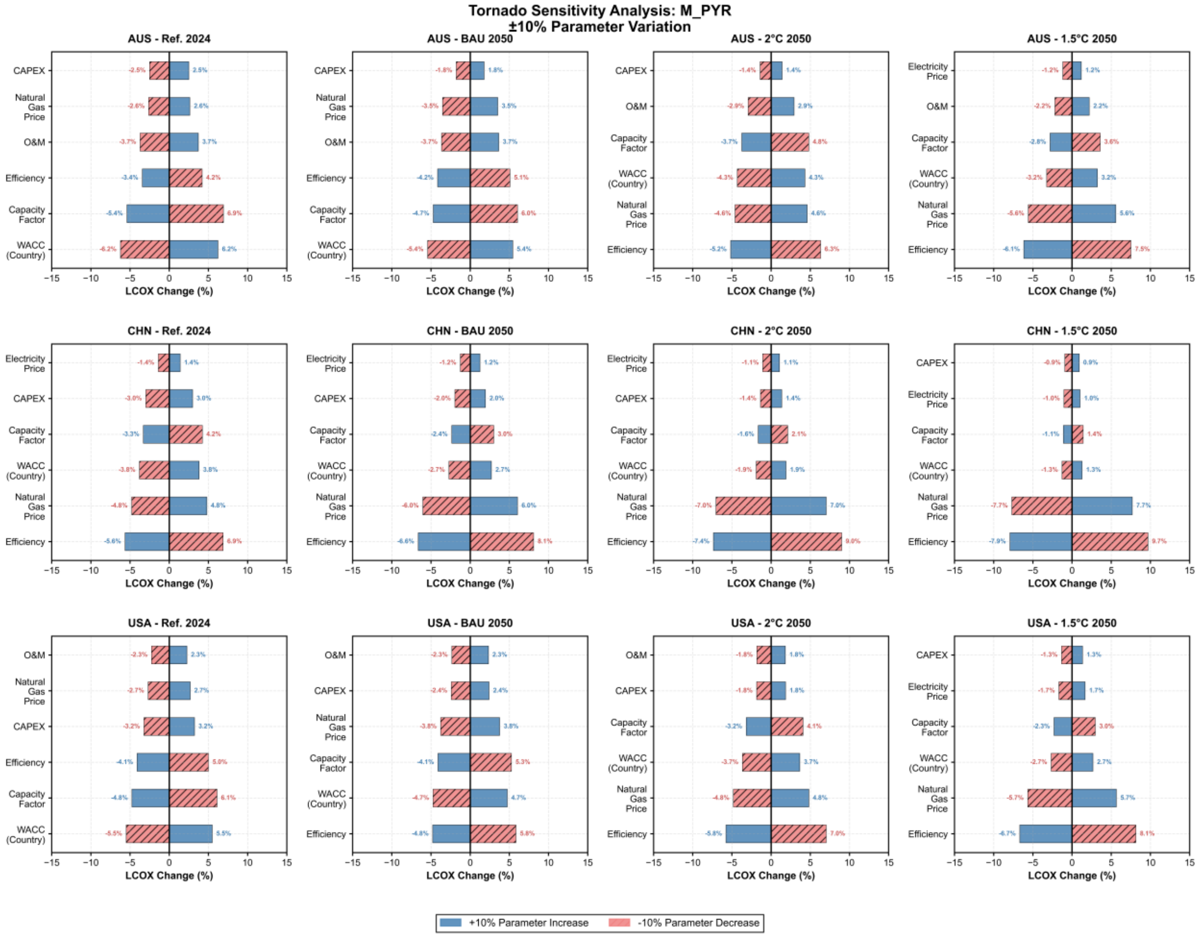

Fig. S42 Tornado sensitivity analysis of levelized hydrogen cost for methane pyrolysis (M_PYR) across Australia, China, and USA under different scenarios (Ref. 2024, BAU 2050, 2°C 2050, and 1.5°C 2050). Each parameter was varied by ±20% from its baseline value. Blue bars represent the impact of +20% parameter increase; red hatched bars represent the impact of -20% parameter decrease.

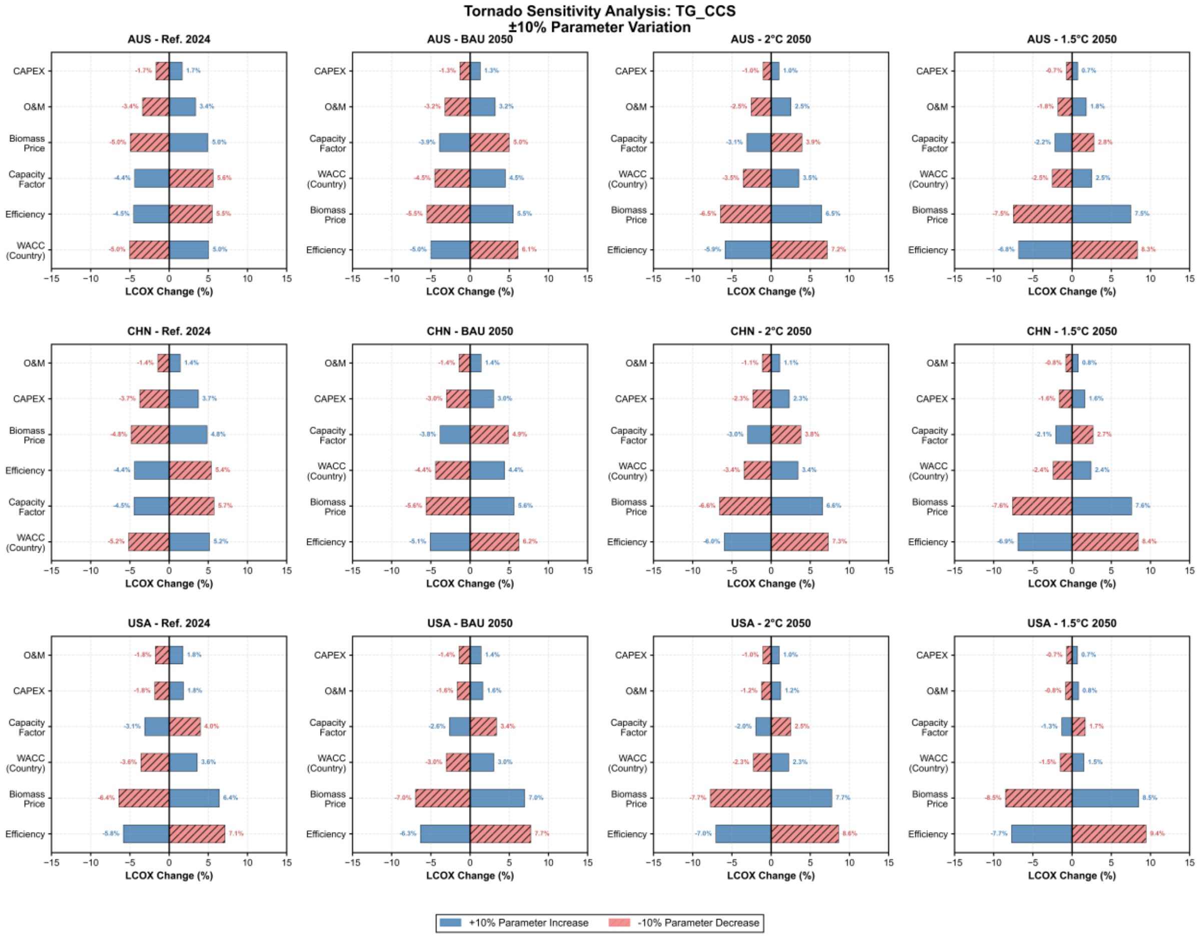

Fig. S43 Tornado sensitivity analysis of levelized hydrogen cost for biomass thermal gasification with CCS (TG_CCS) across Australia, China, and USA under different scenarios (Ref. 2024, BAU 2050, 2°C 2050, and 1.5°C 2050). Each parameter was varied by ±20% from its baseline value. Blue bars represent the impact of +20% parameter increase; red hatched bars represent the impact of -20% parameter decrease.

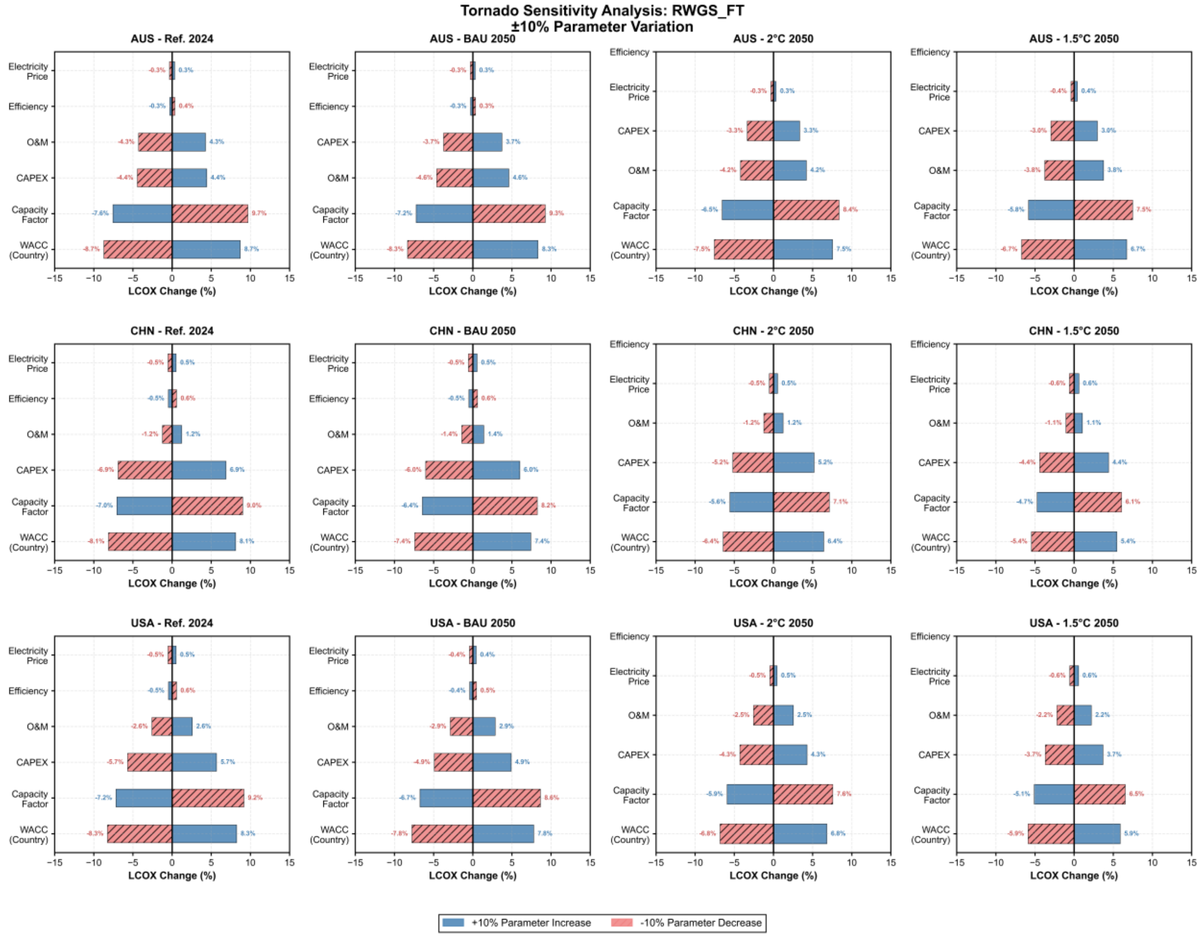

Fig. S44 Tornado sensitivity analysis of levelized hydrogen cost for reverse water gas shift FT (RWGS-FT) across Australia, China, and USA under different scenarios (Ref. 2024, BAU 2050, 2°C 2050, and 1.5°C 2050). Each parameter was varied by ±20% from its baseline value. Blue bars represent the impact of +20% parameter increase; red hatched bars represent the impact of -20% parameter decrease.

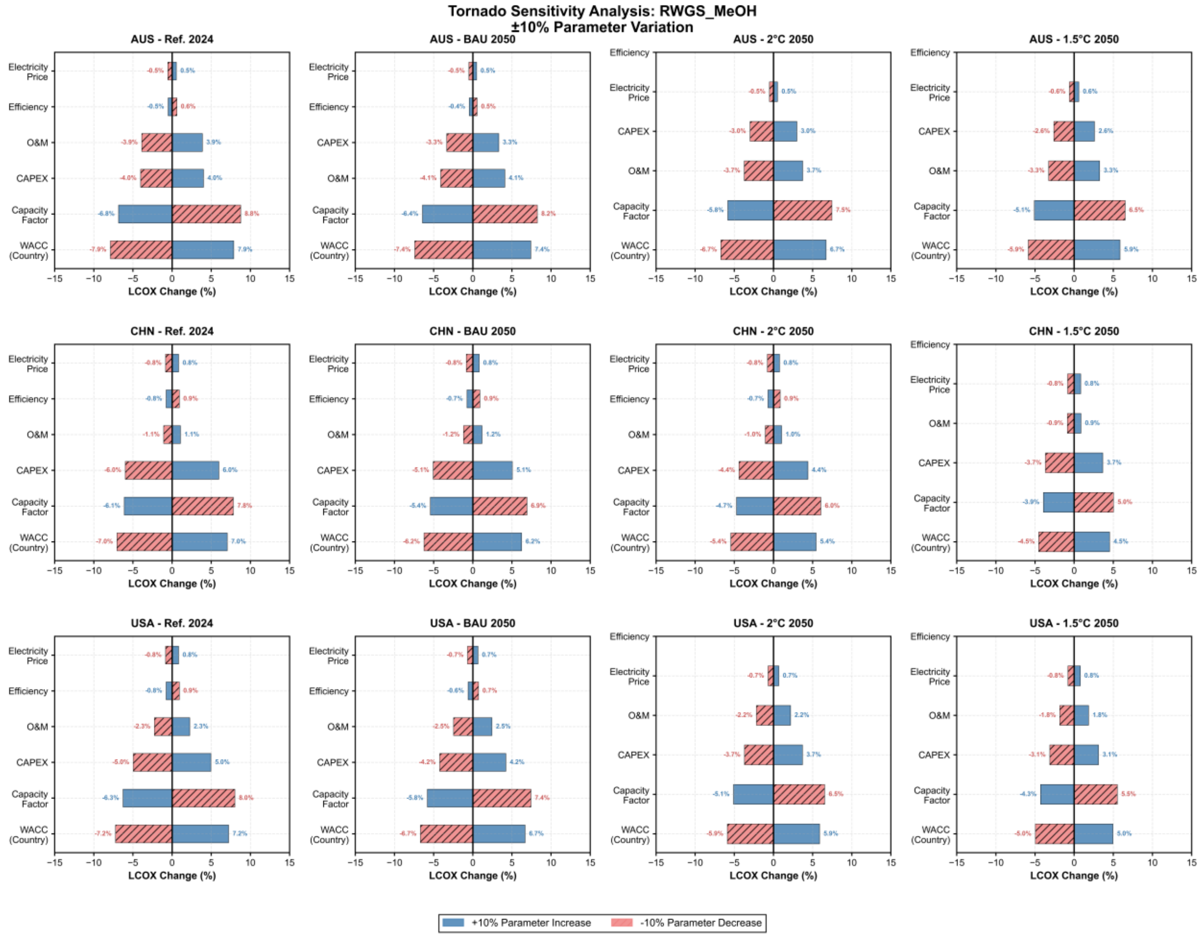

Fig. S45 Tornado sensitivity analysis of levelized hydrogen cost for reverse water gas shift MeOH Synthesis (RWGS-MeOH) across Australia, China, and USA under different scenarios (Ref. 2024, BAU 2050, 2°C 2050, and 1.5°C 2050). Each parameter was varied by ±20% from its baseline value. Blue bars represent the impact of +20% parameter increase; red hatched bars represent the impact of -20% parameter decrease.

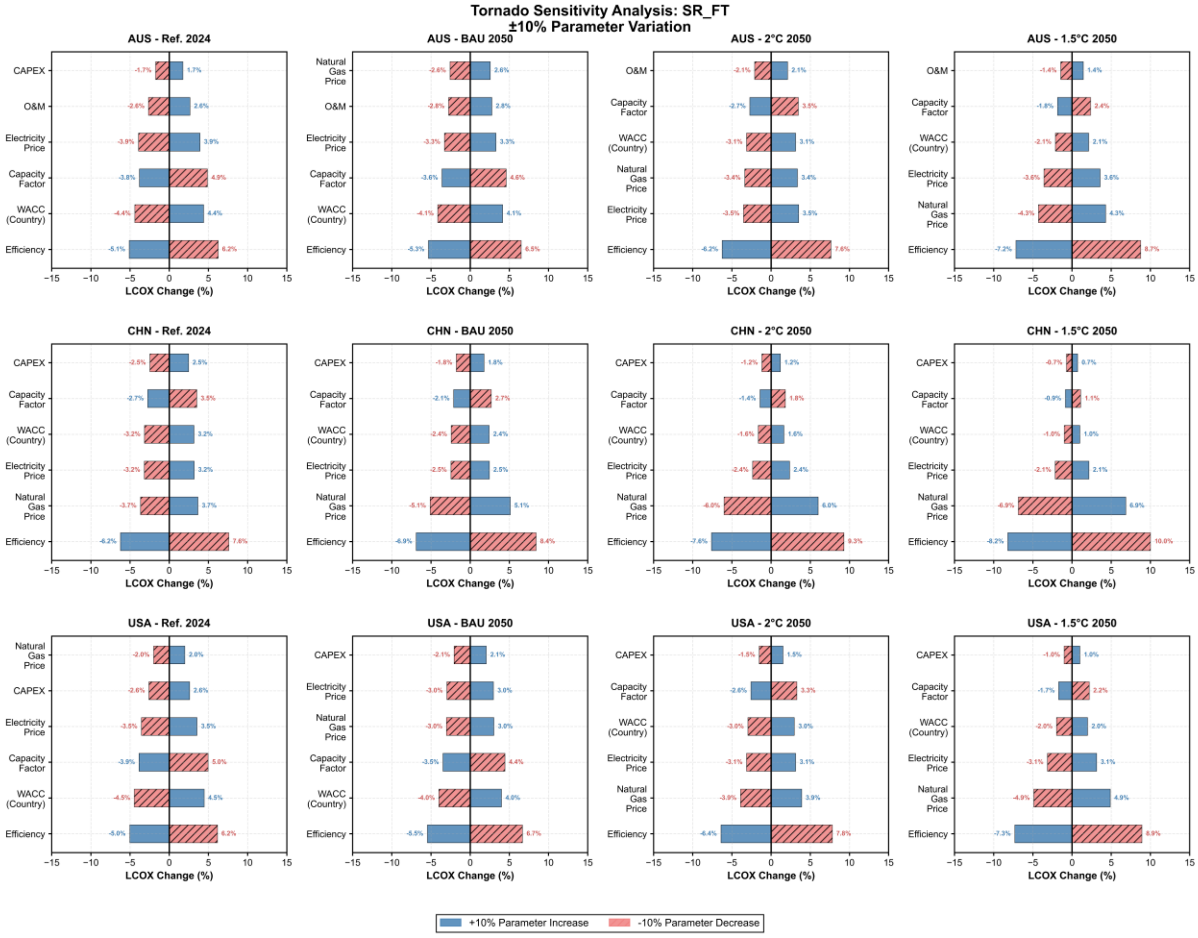

Fig. S46 Tornado sensitivity analysis of levelized hydrogen cost for solar reforming Fischer–Tropsch (SR-FT) across Australia, China, and USA under different scenarios (Ref. 2024, BAU 2050, 2°C 2050, and 1.5°C 2050). Each parameter was varied by ±20% from its baseline value. Blue bars represent the impact of +20% parameter increase; red hatched bars represent the impact of -20% parameter decrease.

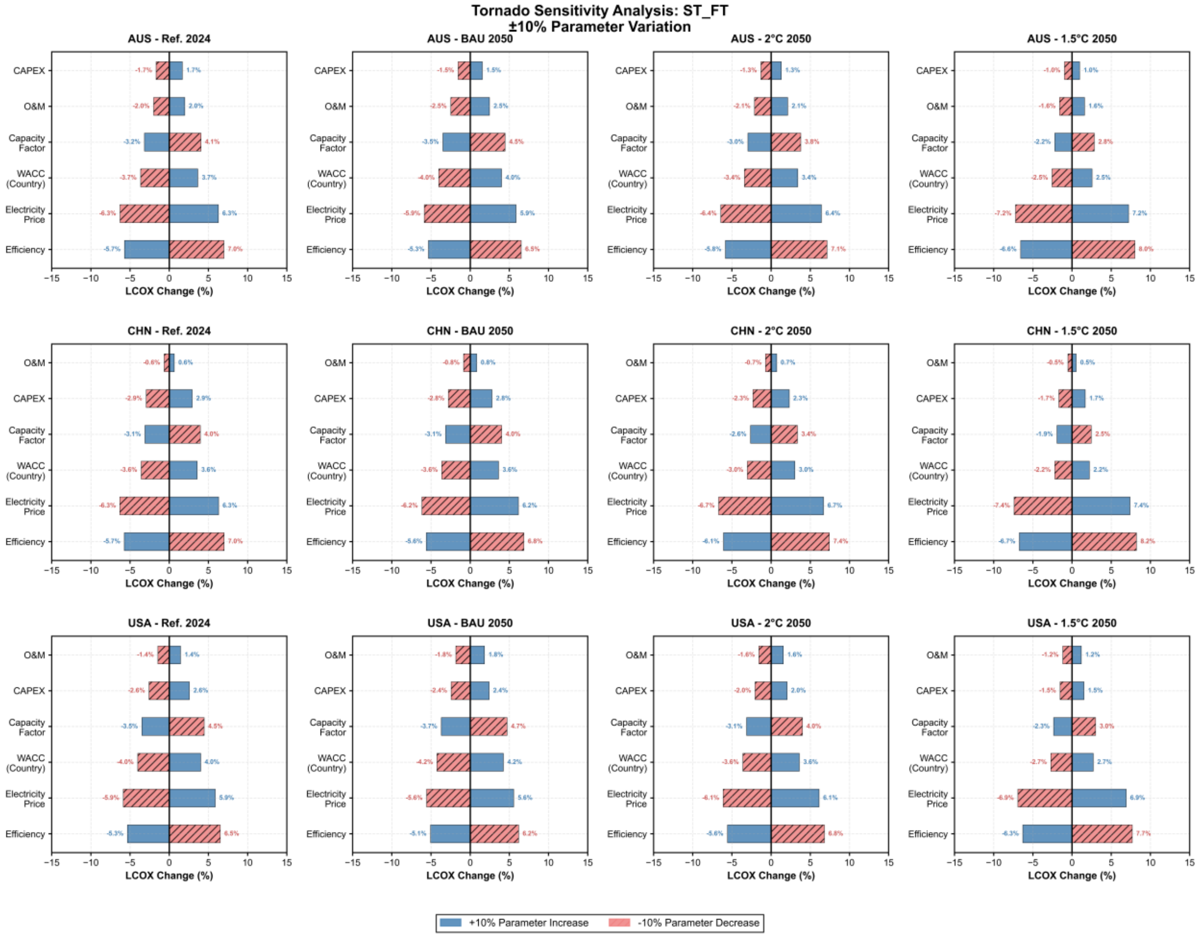

Fig. S47 Tornado sensitivity analysis of levelized hydrogen cost for solar thermochemical Fischer–Tropsch (ST-FT) across Australia, China, and USA under different scenarios (Ref. 2024, BAU 2050, 2°C 2050, and 1.5°C 2050). Each parameter was varied by ±20% from its baseline value. Blue bars represent the impact of +20% parameter increase; red hatched bars represent the impact of -20% parameter decrease.

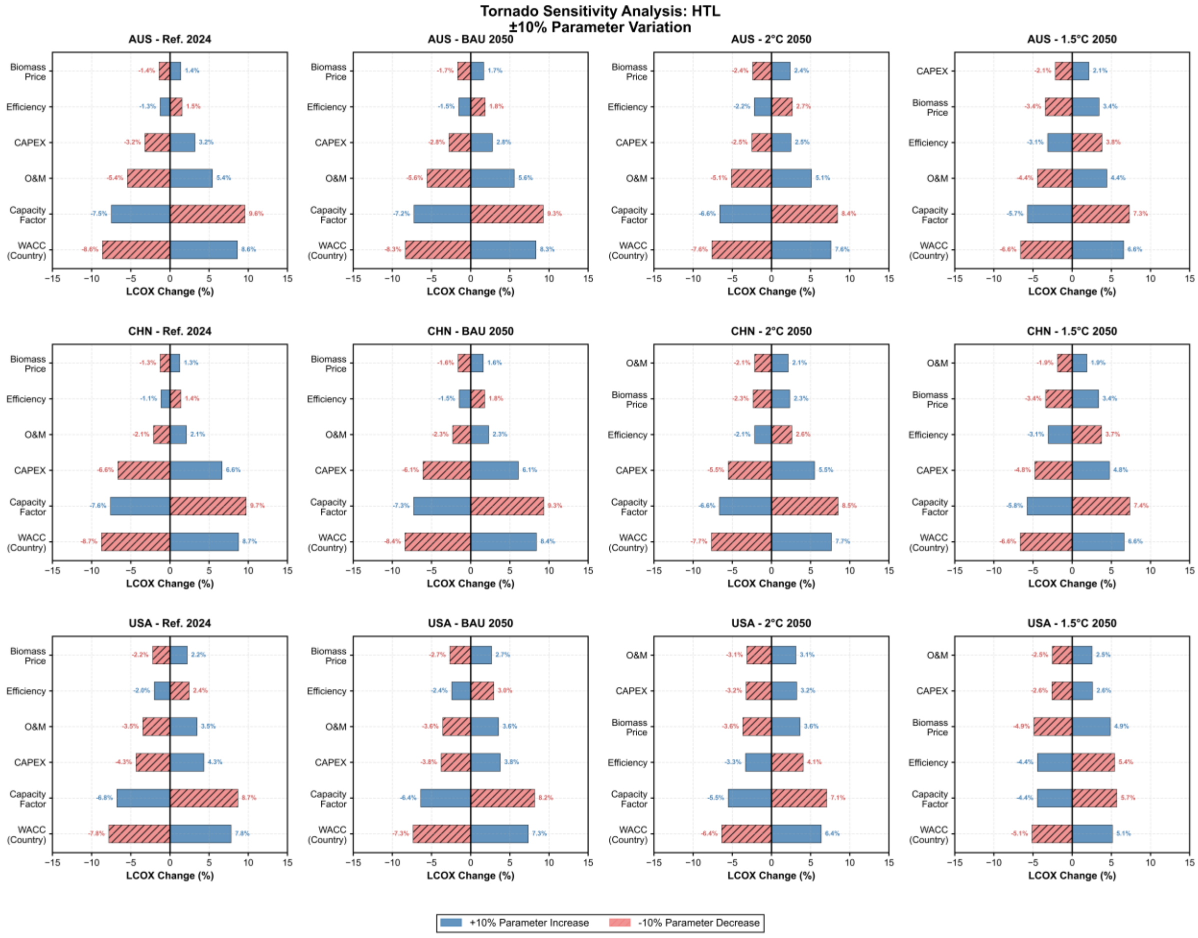

Fig. S48 Tornado sensitivity analysis of levelized hydrogen cost for hydrothermal liquefaction and upgrading (HTL) across Australia, China, and USA under different scenarios (Ref. 2024, BAU 2050, 2°C 2050, and 1.5°C 2050). Each parameter was varied by ±20% from its baseline value. Blue bars represent the impact of +20% parameter increase; red hatched bars represent the impact of -20% parameter decrease.

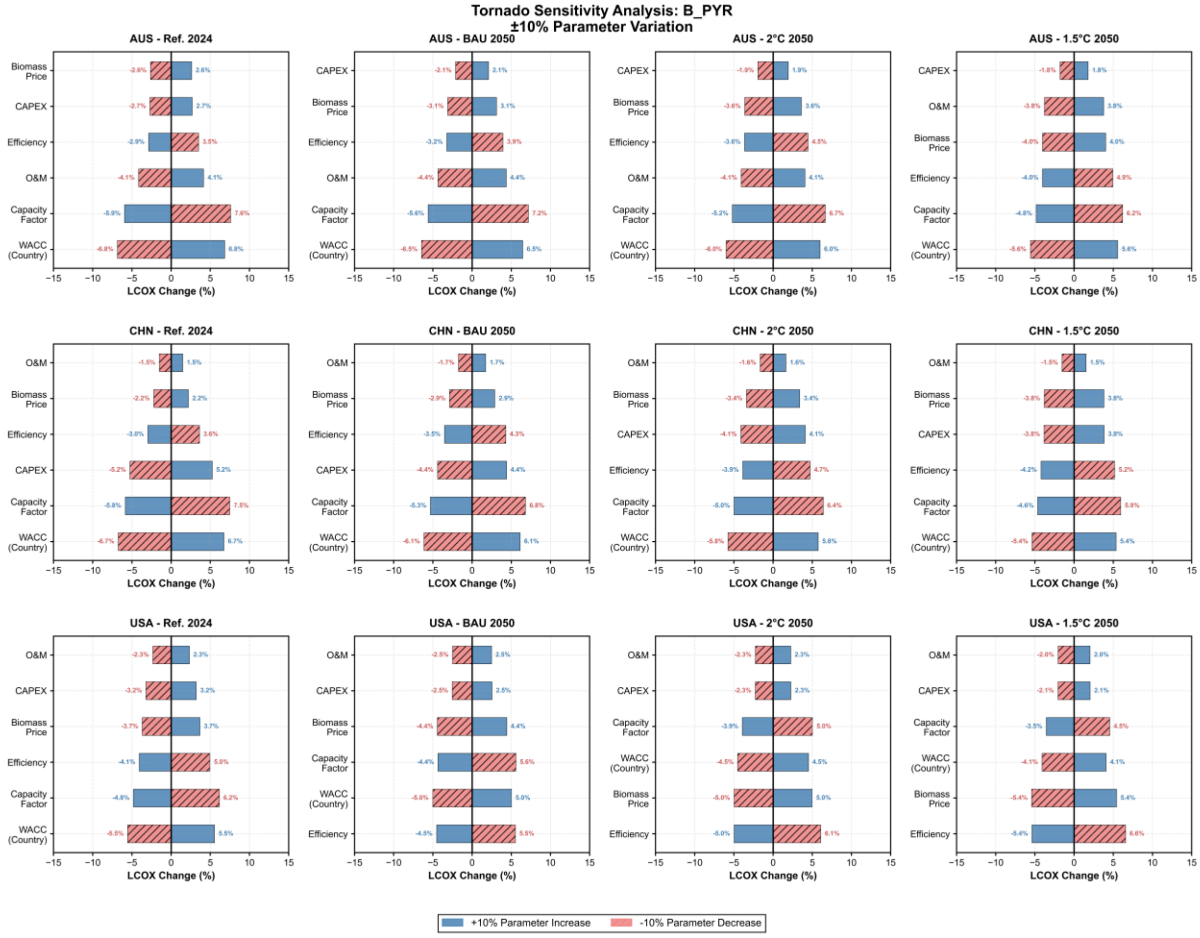

Fig. S49 Tornado sensitivity analysis of levelized hydrogen cost for biomass pyrolysis kerosene (B_PYR) across Australia, China, and USA under different scenarios (Ref. 2024, BAU 2050, 2°C 2050, and 1.5°C 2050). Each parameter was varied by ±20% from its baseline value. Blue bars represent the impact of +20% parameter increase; red hatched bars represent the impact of -20% parameter decrease.

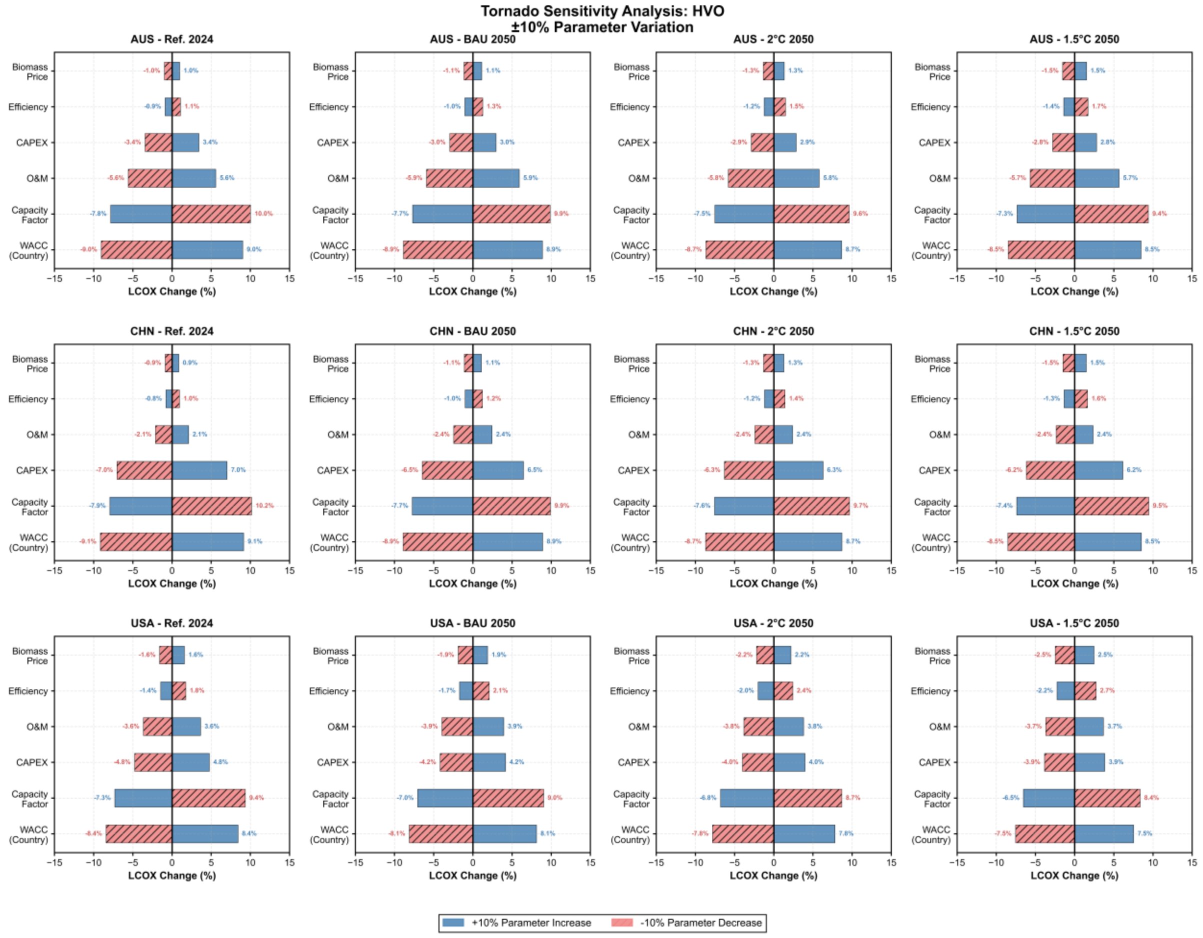

Fig. S50 Tornado sensitivity analysis of levelized hydrogen cost for hydrotreated vegetable oil/hydroprocessed esters and fatty acids (HEFA/HVO) across Australia, China, and USA under different scenarios (Ref. 2024, BAU 2050, 2°C 2050, and 1.5°C 2050). Each parameter was varied by ±20% from its baseline value. Blue bars represent the impact of +20% parameter increase; red hatched bars represent the impact of -20% parameter decrease.

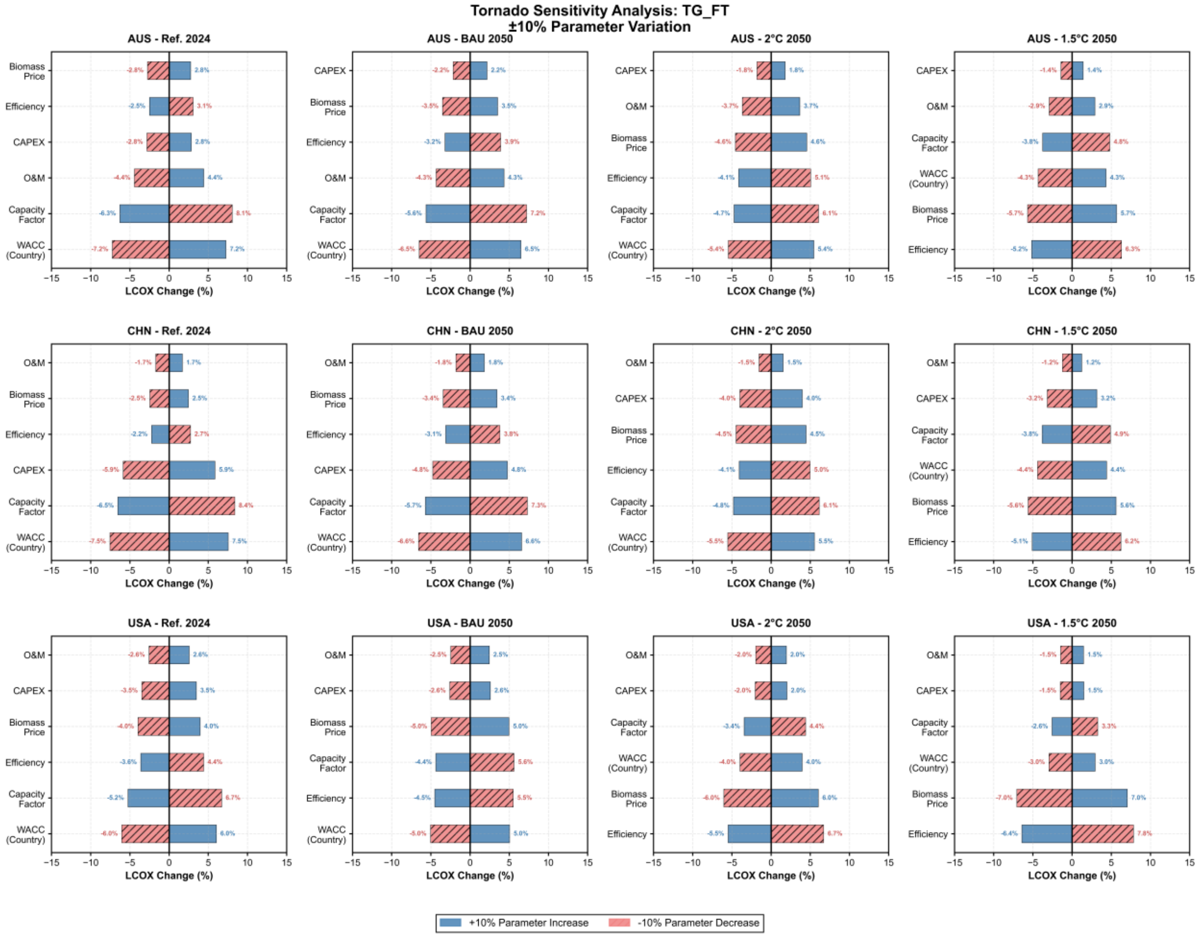

Fig. S51 Tornado sensitivity analysis of levelized hydrogen cost for biomass thermal gasification FT (TG-FT_ across Australia, China, and USA under different scenarios (Ref. 2024, BAU 2050, 2°C 2050, and 1.5°C 2050). Each parameter was varied by ±20% from its baseline value. Blue bars represent the impact of +20% parameter increase; red hatched bars represent the impact of -20% parameter decrease.

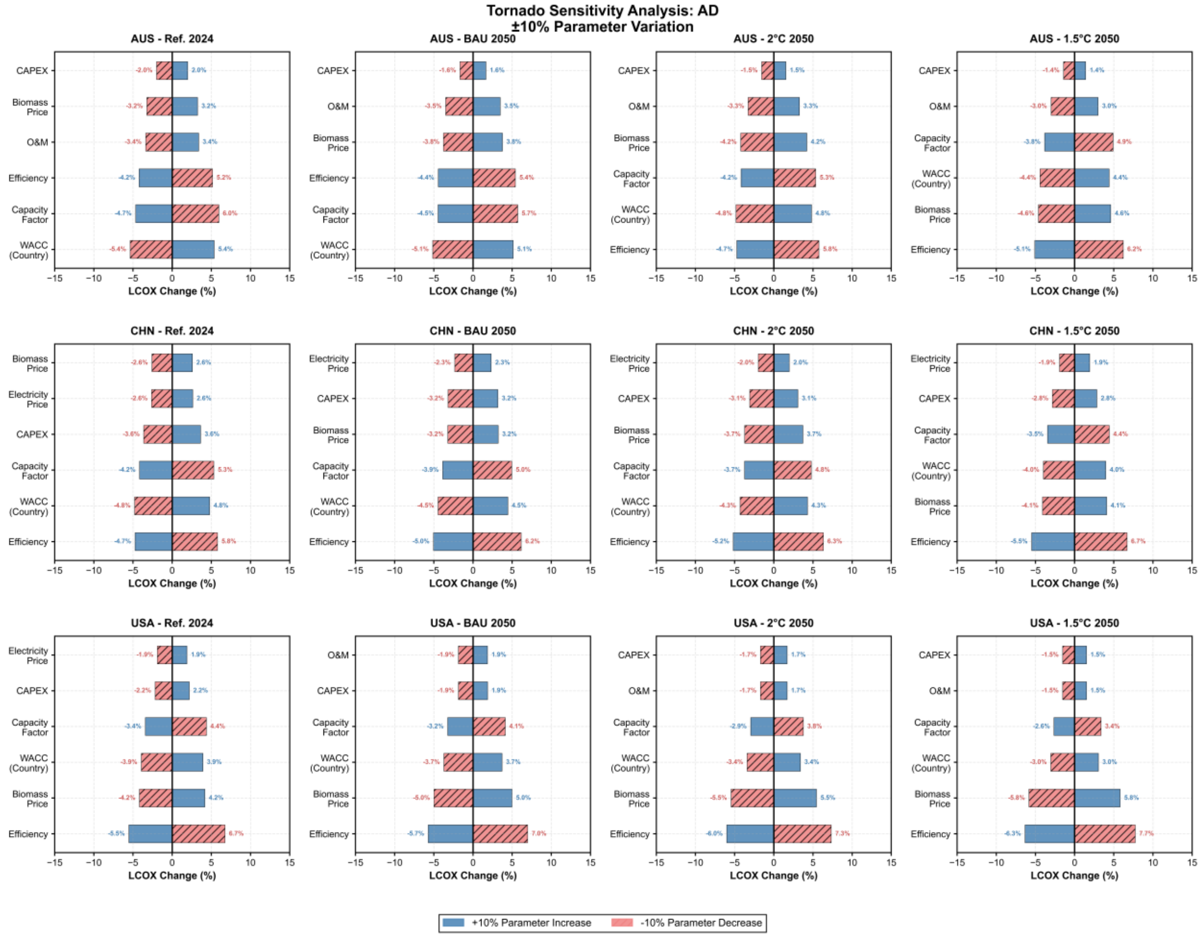

Fig. S52 Tornado sensitivity analysis of levelized hydrogen cost for anaerobic digestion (AD) methane across Australia, China, and USA under different scenarios (Ref. 2024, BAU 2050, 2°C 2050, and 1.5°C 2050). Each parameter was varied by ±20% from its baseline value. Blue bars represent the impact of +20% parameter increase; red hatched bars represent the impact of -20% parameter decrease.

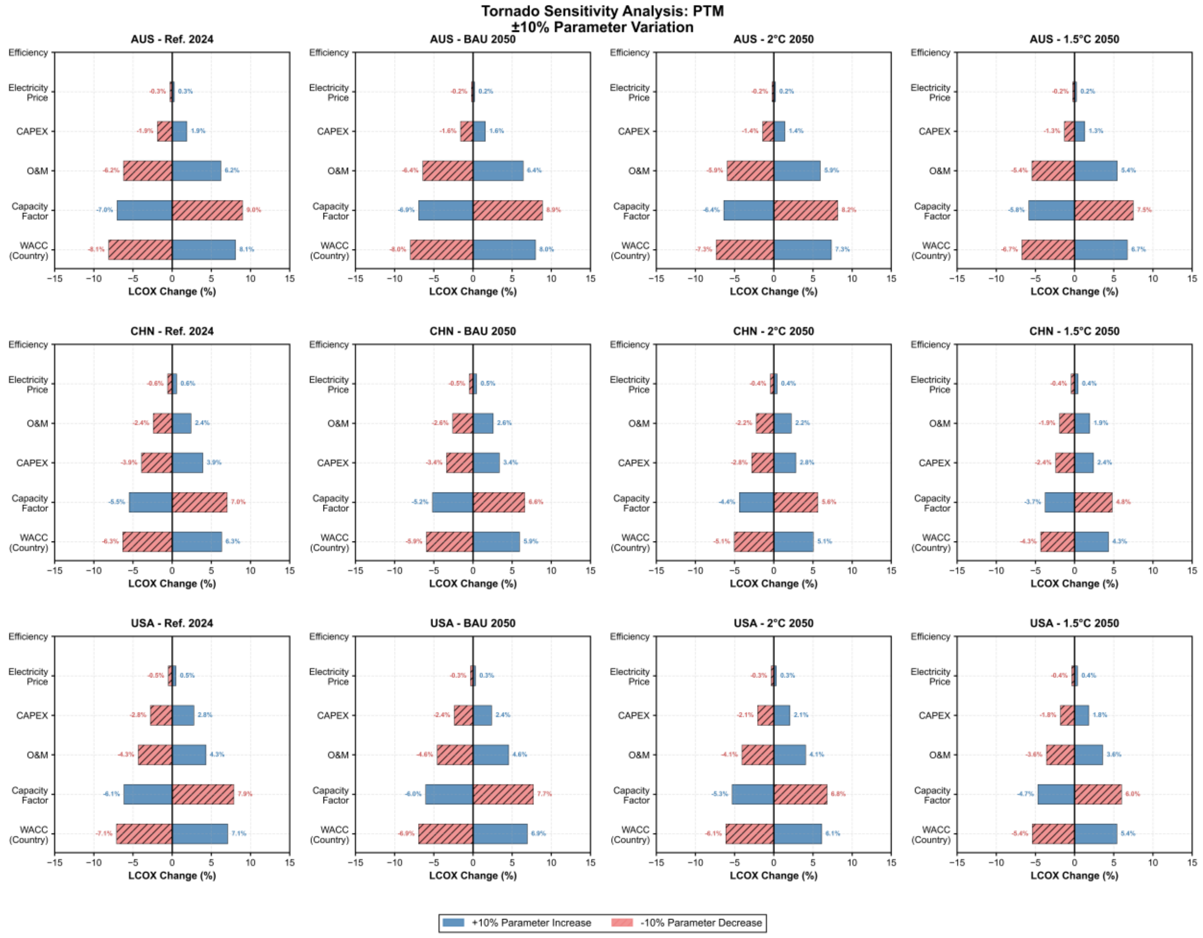

Fig. S53 Tornado sensitivity analysis of levelized hydrogen cost for power to methane (PTM) methane across Australia, China, and USA under different scenarios (Ref. 2024, BAU 2050, 2°C 2050, and 1.5°C 2050). Each parameter was varied by ±20% from its baseline value. Blue bars represent the impact of +20% parameter increase; red hatched bars represent the impact of -20% parameter decrease.

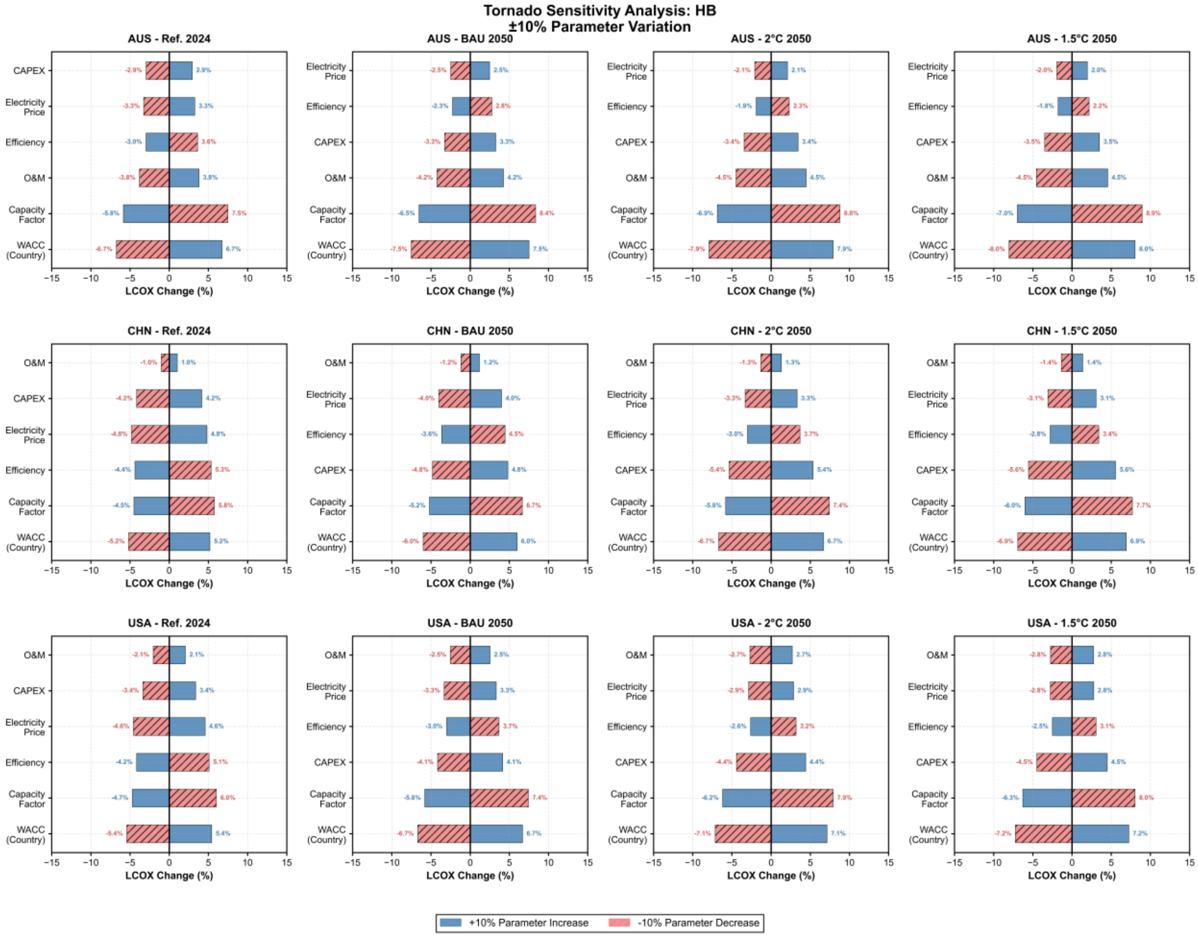

Fig. S54 Tornado sensitivity analysis of levelized hydrogen cost for Habor Bosch (with Green Hydrogen) (HB) across Australia, China, and USA under different scenarios (Ref. 2024, BAU 2050, 2°C 2050, and 1.5°C 2050). Each parameter was varied by ±20% from its baseline value. Blue bars represent the impact of +20% parameter increase; red hatched bars represent the impact of -20% parameter decrease.

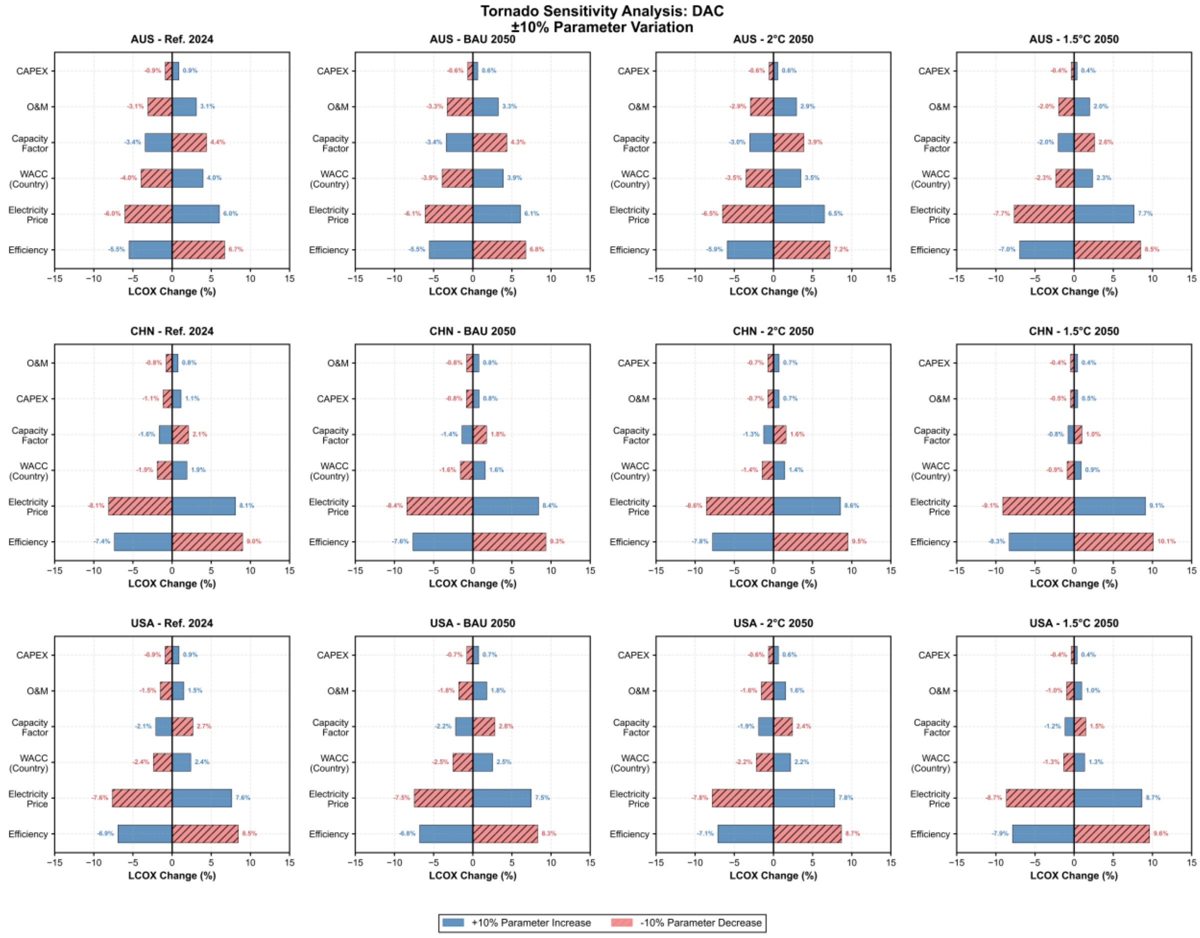

Fig. S55 Tornado sensitivity analysis of levelized hydrogen cost for direct air capture (DAC) CO_2 across Australia, China, and USA under different scenarios (Ref. 2024, BAU 2050, 2°C 2050, and 1.5°C 2050). Each parameter was varied by ±20% from its baseline value. Blue bars represent the impact of +20% parameter increase; red hatched bars represent the impact of -20% parameter decrease.

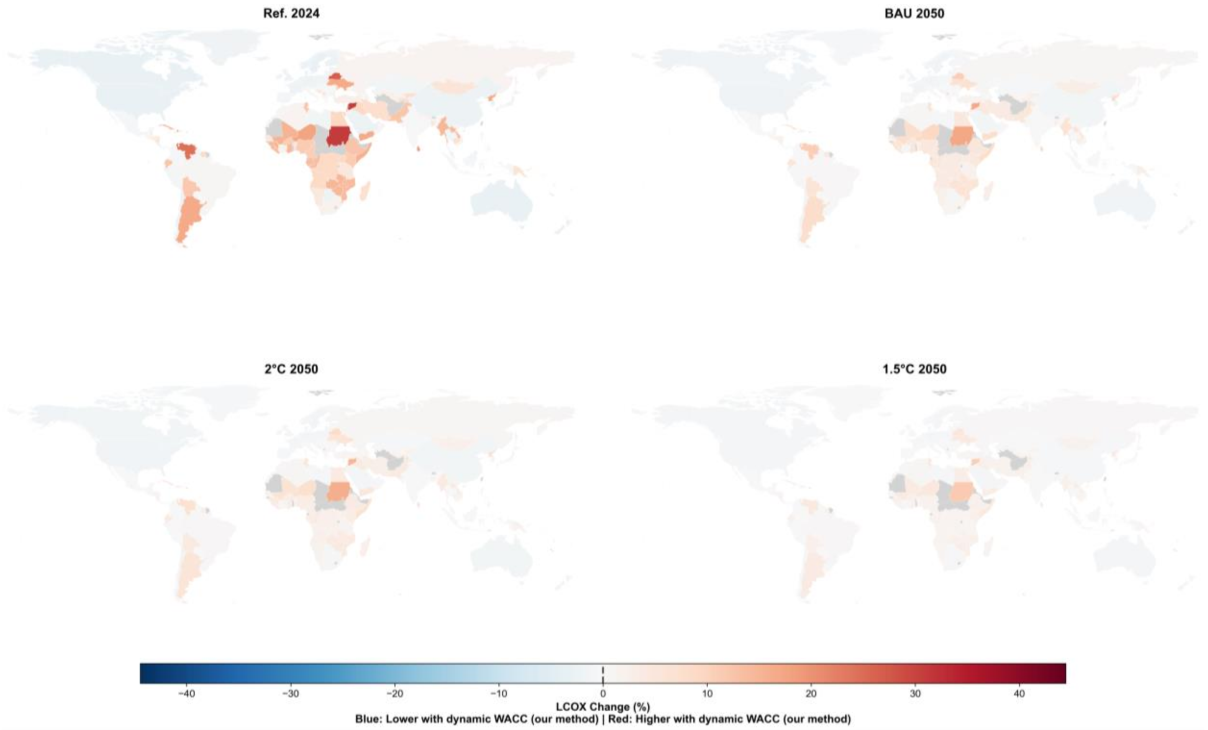

Fig. S56 Global distribution of cost differences between the dynamic country-specific WACC approach and a unified 8% WACC baseline for Direct Air Capture (DAC) across four scenarios. Values represent percentage change relative to the unified baseline scenario.

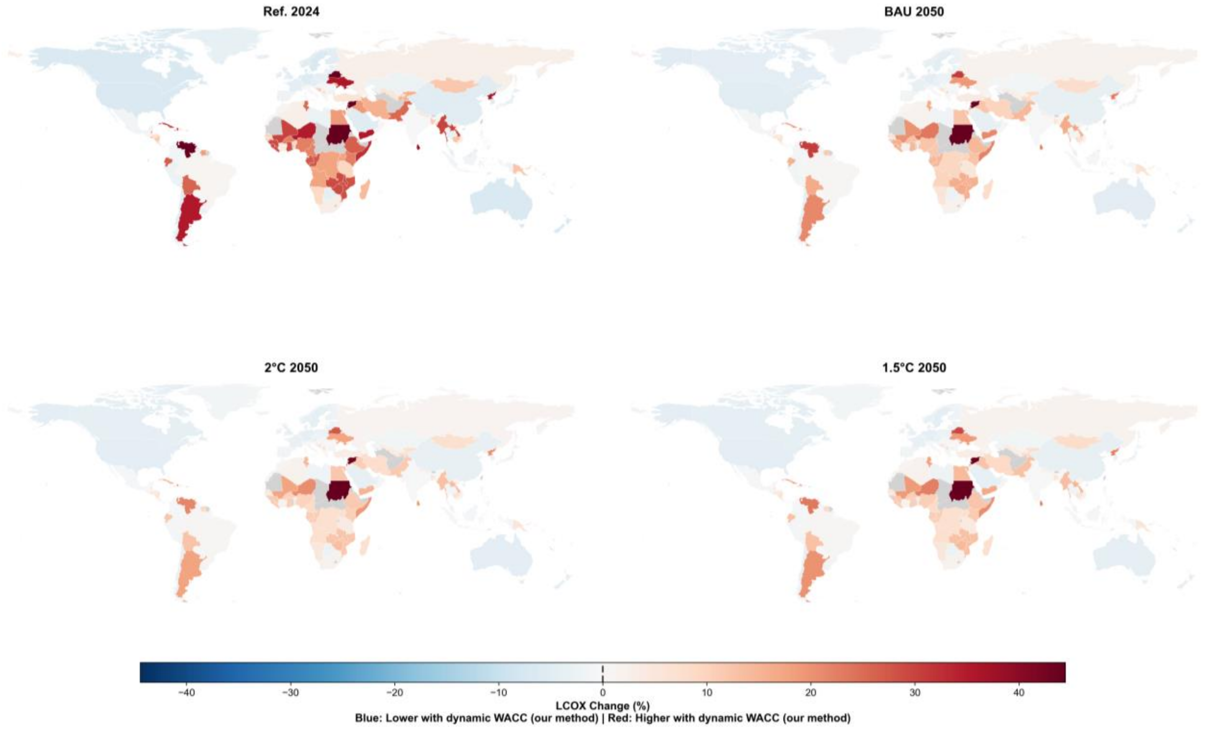

Fig. S57 Global distribution of cost differences between the dynamic country-specific WACC approach and a unified 8% WACC baseline for Proton Exchange Membrane (PEM) electrolysis across four scenarios. Values represent percentage change relative to the unified baseline scenario.

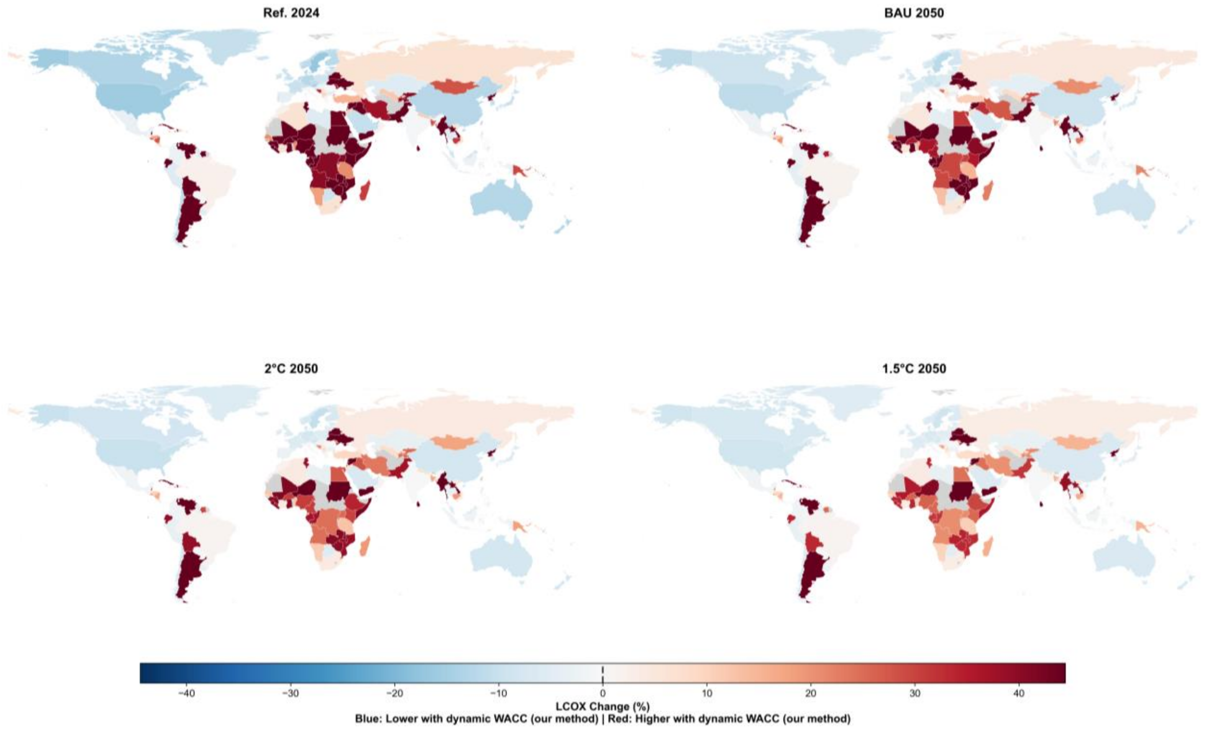

Fig. S58 Global distribution of cost differences between the dynamic country-specific WACC approach and a unified 8% WACC baseline for Reverse Water-Gas Shift Fischer-Tropsch (RWGS_FT) synthesis across four scenarios. Values represent percentage change relative to the unified baseline scenario.

References

1. Terlouw, T., Bauer, C., McKenna, R. & Mazzotti, M. Large-scale hydrogen production via water electrolysis: a techno-economic and environmental assessment. *ENERGY Environ. Sci.* **15**, 3583–3602 (2022).
2. Alabbadi, A. A., Obaid, O. A. & AlZahrani, A. A. A comparative economic study of nuclear hydrogen production, storage, and transportation. *Int. J. Hydrog. Energy* **54**, 849–863 (2024).
3. Frick, K., Wendt, D., Talbot, P., Rabiti, C. & Boardman, R. Technoeconomic assessment of hydrogen cogeneration via high temperature steam electrolysis with a light-water reactor. *Appl. Energy* **306**, 118044 (2022).
4. Razi, F., Dincer, I. & Gabriel, K. Exergoeconomic analysis of a new integrated copper-chlorine cycle for hydrogen production. *Int. J. Hydrog. Energy* **45**, 30042–30055 (2020).
5. Razi, F., Hewage, K. & Sadiq, R. Exergoeconomic performance evaluation of three, four, and five-step thermochemical copper-chlorine cycles for hydrogen production. *J. Clean. Prod.* **409**, 137219 (2023).
6. Karaca, A. E., Dincer, I. & Gu, J. Life cycle assessment study on nuclear based sustainable hydrogen production options. *Int. J. Hydrog. Energy* **45**, 22148–22159 (2020).
7. Oni, A. O., Anaya, K., Giwa, T., Di Lullo, G. & Kumar, A. Comparative assessment of blue hydrogen from steam methane reforming, autothermal reforming, and natural gas decomposition technologies for natural gas-producing regions. *Energy Convers. Manag.* **254**, 115245 (2022).
8. Argyris, P. A., Wong, J., Wright, A., Pereira, L. M. C. & Spallina, V. Reducing the cost of low-carbon hydrogen production via emerging chemical looping process. *Energy Convers. Manag.* **277**, 116581 (2023).
9. Patlolla, S. R. *et al.* A review of methane pyrolysis technologies for hydrogen production. *Renew. Sustain. Energy Rev.* **181**, 113323 (2023).
10. Cormos, C.-C. Green hydrogen production from decarbonized biomass gasification: An integrated techno-economic and environmental analysis. *Energy* **270**, 126926 (2023).
11. Wu, N., Lan, K. & Yao, Y. An integrated techno-economic and environmental assessment for carbon capture in hydrogen production by biomass gasification. *Resour. Conserv. Recycl.* **188**, (2023).
12. Falter, C., Valente, A., Habersetzer, A., Iribarren, D. & Dufour, J. An integrated techno-economic, environmental and social assessment of the solar thermochemical fuel pathway †. *Sustain. Energy Fuels* **4**, 3992 (2020).
13. Detz, R., Reek, J. & van der Zwaan, B. The future of solar fuels: when could they become competitive? *ENERGY Environ. Sci.* **11**, 1653–1669 (2018).
14. Eyberg, V. *et al.* Techno-economic assessment and comparison of Fischer–Tropsch and Methanol-to-Jet processes to produce sustainable aviation fuel via Power-to-Liquid. *Energy Convers. Manag.* **315**, 118728 (2024).
15. Gonzalez-Garay, A. *et al.* Unravelling the potential of sustainable aviation fuels to decarbonise the aviation sector. *Energy Environ. Sci.* **15**, 3291–3309 (2022).
16. Okoye-Chine, C. G. *et al.* Biomass to Liquid Fuel via Fischer–Tropsch (BTL-FT) Synthesis: Process Description and Economic Analysis. in *Chemicals and Fuels from Biomass via Fischer–Tropsch Synthesis: A Route to Sustainability* (eds Gorimbo, J., Liu, X., Yao, Y. & Hildebrandt, D.) 0 (The Royal Society of Chemistry, 2022). doi:10.1039/9781839167829-00412.
17. Lee, K., Sun, P., Elgowainy, A., Baek, K. H. & Bobba, P. Techno-economic and life cycle analysis of synthetic natural gas production from low-carbon H2 and point-source or atmospheric CO2 in the United States. *J. CO2 Util.* **83**, 102791 (2024).

18. Arnaiz del Pozo, C. & Cloete, S. Techno-economic assessment of blue and green ammonia as energy carriers in a low-carbon future. *Energy Convers. Manag.* **255**, 115312 (2022).
19. Sievert, K., Schmidt, T. S. & Steffen, B. Considering technology characteristics to project future costs of direct air capture. *Joule* **8**, 979–999 (2024).
20. Karras, T., Brosowski, A. & Thrän, D. A Review on Supply Costs and Prices of Residual Biomass in Techno-Economic Models for Europe. *Sustainability* **14**, 7473 (2022).
21. IPCC. *SYNTHESIS REPORT OF THE IPCC SIXTH ASSESSMENT REPORT (AR6) - Summary for Policymakers*. 26 https://report.ipcc.ch/ar6syr/pdf/IPCC_AR6_SYR_SPM.pdf (2023).
22. Nicholson, S. & Heath, G. Life Cycle Emissions Factors for Electricity Generation Technologies. 1 files National Renewable Energy Laboratory - Data (NREL-DATA), Golden, CO (United States); National Renewable Energy Laboratory (NREL), Golden, CO (United States) https://doi.org/10.7799/1819907 (2021).
23. Damodaran, A. Country Risk: Determinants, Measures and Implications - The 2022 Edition. SSRN Scholarly Paper at https://doi.org/10.2139/ssrn.4161010 (2022).
24. Egli, F. *et al.* Mapping the cost competitiveness of African green hydrogen imports to Europe. *Nat. Energy* 1–12 (2025) doi:10.1038/s41560-025-01768-y.
25. Calcaterra, M. *et al.* Reducing the cost of capital to finance the energy transition in developing countries. *Nat. Energy* 1–11 (2024) doi:10.1038/s41560-024-01606-7.
26. Lonergan, K. E. *et al.* Improving the representation of cost of capital in energy system models. *Joule* **7**, 469–483 (2023).
27. Egli, F., Steffen, B. & Schmidt, T. S. Bias in energy system models with uniform cost of capital assumption. *Nat. Commun.* **10**, 4588 (2019).
28. Yates, J. *et al.* Techno-economic Analysis of Hydrogen Electrolysis from Off-Grid Stand-Alone Photovoltaics Incorporating Uncertainty Analysis. *Cell Rep. Phys. Sci.* **1**, (2020).
29. Jang, D., Kim, K., Kim, K. & Kang, S. Techno-economic analysis and Monte Carlo simulation for green hydrogen production using offshore wind power plant. *ENERGY Convers. Manag.* **263**, (2022).
30. Jang, D., Kim, J., Kim, D., Han, W.-B. & Kang, S. Techno-economic analysis and Monte Carlo simulation of green hydrogen production technology through various water electrolysis technologies. *Energy Convers. Manag.* **258**, 115499 (2022).
31. Frey, P. Techno-Economic Assessment of Feedstock and Supply Chain Potential of Power-to-X Fuels for Switzerland. (University of Zurich, Zurich, 2023).
32. Bauer, C. *et al.* On the climate impacts of blue hydrogen production. *Sustain. Energy Fuels* **6**, 66–75 (2022).
33. Radner, F. *et al.* Off-grid hydrogen production: Analysing hydrogen production and supply costs considering country-specifics and transport to Europe. *Int. J. Hydrog. Energy* **80**, 1197–1209 (2024).
34. World Energy Outlook 2023 – Analysis. *IEA* https://www.iea.org/reports/world-energy-outlook-2023 (2023).
35. Zhen, Z. *et al.* Hydrogen production paths in China based on learning curve and discrete choice model. *J. Clean. Prod.* **415**, 137848 (2023).
36. IEA. *Towards Hydrogen Definitions Based on Their Emissions Intensity*. https://www.oecd-ilibrary.org/energy/towards-hydrogen-definitions-based-on-their-emissions-intensity_44618fd1-en (2023) doi:10.1787/44618fd1-en.
37. Baumstark, L. *et al.* REMIND2.1: transformation and innovation dynamics of the energy-economic system within climate and sustainability limits. *Geosci. Model Dev.* **14**, 6571–6603 (2021).

38. George, J. F., Müller, V. P., Winkler, J. & Ragwitz, M. Is blue hydrogen a bridging technology? - The limits of a CO2 price and the role of state-induced price components for green hydrogen production in Germany. *Energy Policy* **167**, 113072 (2022).
39. Dieterich, V., Buttler, A., Hanel, A., Spliethoff, H. & Fendt, S. Power-to-liquid via synthesis of methanol, DME or Fischer–Tropsch-fuels: a review. *Energy Environ. Sci.* **13**, 3207–3252 (2020).
40. Rahbari, A., Shirazi, A., Venkataraman, M. B. & Pye, J. A solar fuel plant via supercritical water gasification integrated with Fischer–Tropsch synthesis: Steady-state modelling and techno-economic assessment. *Energy Convers. Manag.* **184**, 636–648 (2019).
41. Voelker, S. *et al.* Towards carbon-neutral and clean propulsion in heavy-duty transportation with hydroformylated Fischer–Tropsch fuels. *Nat. Energy* **9**, 1220–1229 (2024).
42. Pasha, M. K., Dai, L., Liu, D., Guo, M. & Du, W. An overview to process design, simulation and sustainability evaluation of biodiesel production. *Biotechnol. Biofuels* **14**, 129 (2021).
43. Dougher, M., Soh, L. & Bala, A. M. Techno-Economic Analysis of Interesterification for Biodiesel Production. *Energy Fuels* **37**, 2912–2925 (2023).
44. Julio, A. A. V. *et al.* Techno-economic and environmental potential of Renewable Diesel as complementation for diesel and biodiesel in Brazil: A comprehensive review and perspectives. *J. Clean. Prod.* **371**, 133431 (2022).
45. Andrésternberg, A. & Andrébardow, A. Life Cycle Assessment of Power-to-Gas: Syngas vs Methane. *ACS Sustain. Chem Eng* **4**, 4156–4165 (2016).
46. Blanco, H., Nijs, W., Ruf, J. & Faaij, A. Potential of Power-to-Methane in the EU energy transition to a low carbon system using cost optimization. *Appl. Energy* **232**, 323–340 (2018).
47. IEA. *Direct Air Capture 2022*. https://www.iea.org/reports/direct-air-capture-2022/executive-summary (2022).
48. Khatiwada, D., Vasudevan, R. A. & Santos, B. H. Decarbonization of natural gas systems in the EU – Costs, barriers, and constraints of hydrogen production with a case study in Portugal. *Renew. Sustain. Energy Rev.* **168**, 112775 (2022).